3-3-2021

Study of Laser Based Additive Manufacturing for Titanium and Copper Alloys

Congyuan Zeng

STUDY OF LASER BASED ADDITIVE MANUFACTURING FOR TITANIUM AND COPPER ALLOYS

A Dissertation

Submitted to the Graduate Faculty of the
Louisiana State University and
Agricultural and Mechanical College
in partial fulfillment of the
requirements for the degree of
Doctor of Philosophy

in

The Department of Mechanical & Industrial Engineering

by
Congyuan Zeng
B.A., Southeast University, China, 2013
M.S., Southeast University, China, 2016
Ph.D., Louisiana State University
May 2021

Acknowledgements

All chapters of this dissertation were either supported by the National Science Foundation, namely Consortium for innovation in manufacturing and materials (CIMM) program (grant number # OIA-1541079), or Louisiana Materials Design Alliance (LAMDA, grant number NSF #OIA-1946231). Or the financial support from National Aeronautics and Space Administration (NASA) (Established Program to Stimulate Competitive Research (EPSCoR) Cooperative Agreement number 80NSSC19M0079 (CFDA number 43.008).

Contents

Acknowledgements ii

List of Tables v

List of Figures vi

Abstract ix

Chapter 1. Introduction 1
1.1 Background 1
1.2 Outline of the manuscript 10

Chapter 2. Titanium and Nitrogen Interactions under Laser Additive Manufacturing Conditions 11
2.1. Introduction 11
2.2. Experimental Section 14
2.3. Results and discussions 17
2.4. Conclusions 29

Chapter 3. Diffusion of Oxygen and Nitrogen into Titanium under Laser Irradiation in Air. 31
3.1. Introduction 31
3.2. Materials and methods 34
3.3. Results and discussions 36
3.4. Conclusions 51

Chapter 4. Laser Nitridation of Titanium Surfaces for Biomedical Applications 53
4.1. Introduction 53
4.2. Materials and methods 55
4.3. Results and discussions 59
4.4. Conclusions 72

Chapter 5. Mechanical, Thermal, and Corrosion Properties of Cu-10Sn Alloy Prepared by Laser-Powder-Bed-Fusion Additive Manufacturing 74
5.1. Introduction 74
5.2. Experimental procedures 75
5.3. Results and discussions 79
5.4. Conclusions 97

Chapter 6. Thermal and Mechanical Properties of Additively Manufactured Cu-1.5Cr-0.5Zr Alloy Samples 98
6.1. Introduction 98
6.2. Materials and methods 99
6.3. Results and discussions 103
6.4. Conclusions 120

Chapter 7. Conclusions 122

Appendix. Reprint Permissions 125

References 129

Vita 153

List of Tables

2.1. Melt pool sizes and the determined hatch spacing.....23

2.2. Laser parameters for samples made under controlled N_2 atmosphere.....26

3.1. Laser parameters.....38

3.2. The calculated diffusion coefficients.....40

3.3. The estimated diffusion coefficients of oxygen and nitrogen.....49

4.1. Laser processing parameters performed on sample surfaces.....56

4.2. Corrosion test results from this study and literature review.....70

5.2. Densities of the samples measured by Archimedes principle.....90

5.2. Slopes describing the weight loss rate of the samples.....94

5.3. Detailed corrosion test results obtained from potentiodynamic polarization tests.....95

List of Figures

2.1. The schematic of the *in-situ* synchrotron X-ray diffraction setup……..……..14

2.2. The *in-situ* diffraction angle and intensity as a function of time.....17

2.3. Titanium-nitrogen phase diagram……...……...……19

2.4. Single laser scanned tracks with differing scanning speeds……..……..……23

2.5. XRD results and phase compositions of the samples……..……..……23

2.6. XRD and phase composition test results on the sample surfaces……..….26

2.7. XPS survey scan spectra of the samples……..……..….27

3.1. Single tracks with varying laser scanning speeds under air environment……..……37

3.2. EDS mapping results of the cross section of Ti-A100 sample……..….39

3.3. SEM images of the cross sections of the samples……..……39

3.4. Image demonstrating *In-situ* X-ray diffraction information……..……..……42

3.5. The phase diagrams calculated using the Thermo-Calc software…….……..43

3.6. Microstructures and composition distribution of the sample surface……..……48

3.7. Diffusion coefficients of from literature and the present study……..…50

4.1. Image of the as-processed samples.....56

4.2. XRD test results of the laser irradiated sample surfaces……59

4.3. SEM images showing the microstructures of cross sections……..…61

4.4. SEM images showing the top view of the laser irradiated surfaces……..…….63

4.5. Surface roughness test results of the processed sample surfaces……...…….63

4.6. Surface hardness of the different samples by nanoindentation technique…….….65

4.7. SEM images illustrating the cell adhesion on the laser processed sample……..…..66

4.8. Representative composite cell viability image of Ti-N400……...…….67

4.9. Images illustrating cell densities……..……..68

4.10. Images showing the potentiodynamic polarization curves of samples…….68

4.11. EDS mapping results of oxygen distribution on the sample surfaces……..…..70

5.1. The powders, laser scanning strategy and the as-fabricated samples…….……76

5.2. XRD analysis results and XRD Rietveld refinement analysis result…….……...…80

5.3. SEM images illustrating the microstructures of the AF samples…….…...…81

5.4. EBSD inverse pole figure (IPF) maps of microstructures of the samples…….……82

5.5. Images showing the pore structures……...84

5.6. Mechanical response of as-fabricated and vacuum-annealed Cu-10Sn samples……86

5.7. Thermal conductivity of both as-fabricated and vacuum-annealed samples…….….89

5.8. Literature data showing thermal conductivty of Cu-Sn alloy…….……....90

5.9. Weight loss and surface phases of the samples…….……..93

5.10. Corrosion test results of the samples in 3.5 wt.% NaCl water solution……..….95

5.11. SEM images showing surface morphologies after weight loss test……96

6.1. Schematic image showing the orientations of the L-PBF samples……..…100

6.2. Temperature profiles of the aging processes……..……..100

6.3. Images indicating the high-temperature tensile test setup……..….101

6.4. Images showing the shapes and sizes of samples…….…101

6.5. Images showing the CALPHAD study results of Cu-1.5Cr-0.5Zr alloy……..…...103

6.6. DSC testing results of samples with differing orientations……..……104

6.7. Three consecutive DSC heating and cooling thermal cycles……..…….105

6.8. Images showing XRD test results of the samples……..……..106

6.9. Microstructures of the samples……...…….107

6.10. Microstrures of as-fabricated Vertical sample after aging treatments……..…..108

6.11. Images showing the composition distribution results……...……..108

6.12. Images showing the thermal properties…….....….109

6.13. Images indicating the thermal properties of the as-fabricated samples…….....113

6.14. Thermal diffusivity of the samples both before and after aging treatments……114

6.15. Specific heat of the samples before and after aging treatments (Vertical)……..115

6.16. Thermal conductivity of the samples both before and after aging treatments……...115

6.17. Tensile test results for as-fabricated samples with differing orientations……..…116

6.18. Microstructures of the samples after tensile testing……...…….117

6.19. Tensile test results of Vertical samples at room temperature, 204 and 427 ℃……..118

6.20. Hardness test results of the samples both before and after aging treatments……..120

Abstract

Material processing by laser is increasingly applied in industrial applications for its outstanding characteristics, such as localized heating, high efficiency, and high manufacturing precision. In this study, two kinds of laser material processing strategies were investigated, namely laser surface engineering and laser-powder-bed fusion additive manufacturing, with pure titanium and copper alloys as target materials, respectively.

For laser surface engineering related studies, the work includes the investigation of the dynamic interactions between titanium and pure nitrogen or ambient air under transient laser processing conditions. Thanks to the *in-situ* synchrotron X-ray diffraction tests, the high-temperature reaction steps between titanium and pure nitrogen/ambient air were successfully revealed. For the titanium-nitrogen interaction case, under a set of gas environments containing different concentrations of nitrogen, the titanium-nitrogen reaction products were examined for compositions, phases, and microstructures. Besides, considering the biomedical application of titanium, the above laser processed surfaces (titanium-nitrogen cases) were also studied for its biocompatibility and corrosion property. For the improved properties, a dense and thick titanium-nitride dendritic layer was found to be desirable. For the titanium-air interaction situation, the microstructures and composition distributions of the reaction products (under transient laser processing conditions) on and within the titanium samples were also reported, which led to the estimation of high-temperature diffusion coefficients for nitrogen and oxygen into the titanium substrate. Moreover, the formation mechanisms of both titanium nitrides and titanium oxides were also discussed.

For laser-powder-bed fusion additive manufacturing research, Cu-10Sn alloy and Cu-1.5Cr-0.5Zr alloy (wt.%, C-18150) parts were examined. After additive manufacturing preparations, the compositions, microstructures, together with mechanical, thermal, and corrosion properties were investigated under both as fabricated and heat-treated conditions. For

the Cu-10Sn alloy, the as-fabricated samples exhibited smaller grain sizes and higher compression strength than those of vacuum annealed samples, which is consistent with the Hall-Petch equation. Thermal conductivity of the as fabricated samples was higher than that of the vacuum annealed samples ascribed to the two-phase constituents of the former. The corrosion rate of the as fabricated samples was almost two times higher than that of the vacuum annealed samples due to the differences in passive layers, intergranular corrosion, and internal galvanic corrosion. For the Cu-1.5Cr-0.5Zr alloy, aging treatments were performed on the samples with three differing fabrication orientations (vertical, angled (45˚), and horizontal to the building direction). Thermal conductivity of the as fabricated samples was significantly reduced due to the extremely fast cooling rate of the laser powder bed fusion process, which made the samples remain as supersaturated state. However, aging above 500 ℃ for 2 hours could dramatically recover the thermal property of the as fabricated samples. Building direction exhibited little influence on the tensile strengths but had obvious effect on ductility of the as fabricated samples. After aging treatments, tensile strengths were improved while ductility of the samples were declined. The highest tensile strength was obtained after aging treatment at 500 ℃ for 2 hours.

Chapter 1. Introduction

1.1 Background

Laser is one of the greatest innovations in the 20th century, which is essentially a beam of electromagnetic radiation with a specific wavelength ranging from ultra-violet to infrared. Laser has many unique characteristics, i.e. high intensity, convergence, coherence, spectral purity and straight-line propagation, which is a clean heat source [1, 2]. With such extraordinary features, laser has improved the developments of several sectors, such as machining, surveying, communications and entertainment [3]. As technology improves, extremely high-power laser (1-100 kW) has been created, which can be delivered to a controlled and precise spot area, making laser beam qualified for more diverse applications, especially for laser material processing [1], such as laser-assisted surface engineering (near-surface region), i.e. laser surface remelting, laser surface nitridation or carbonization [4-6], laser forming, laser powder-bed-fusion additive manufacturing [7-9], laser joining (i.e. welding, brazing) [10, 11], and laser machining (drilling, cutting, etc.) [12, 13]. In the present contribution, the main research topics are laser surface engineering and laser powder-bed-fusion additive manufacturing.

Laser surface engineering. In real applications, surfaces of materials are prone to the influence of external environments. For example, copper alloys are widely used as electronic packaging materials due to their high thermal conductivities, however, copper alloys are quite susceptible to the thermal oxidation when exposed to the high temperature of the electronic package working condictions under air atmosphere [14]. Owing to the low surface hardness, titanium or titanium alloys show inferior tribological peformance, which limit this material for non-tribological applications only [15]. Magnesium and its alloys are light metals with many excellent properties, such as high specific rigidity, biocompatibility, easy recycling, and high thermal conductivity, which are applied in the aerospace and automotive industries. However,

the poor corrosion resistance limited their applications [16]. In the meantime, machenical faliures are, in most cases, initiated from the exterior layers of the working components, especially for the components used under fatigue and bending loading conditions [1, 17]. Therefore, surface modification to enhance surface hardness and corrosion/oxidation resistance would be effective to significantly improve the properties of components and expand their applications.

A number of surface modification methods have been applied for improving surface performance. First, plasma surface modification, during which the substrate is exposed to the partially ionized gas enviroments comprising high contents of excited ionic, molecular, atomic and excited species, leading to both chemical and physical modifications of the substrate surfaces [18-20]. Second, diffusion coating [21-23], in which process, an alloying element enriched layer was generated on the surface of the substrate, acting as an alloying element diffusion source typically at elevated temepratures. If the alloying element is reactive with the base material, reaction products would generate on the component surface. Third, gas nitridation [24-26], this process involves the atomic nitrogen (typically dissociating ammonia gas) diffusing into the substrate at elevated temperatures, and form the so-called "diffusion zone" with both diffused nitrogen and reacted nitrides. Fourth, carburizing [27-29] is typically applied for iron or steels, which would absorb carbon while heated to high temperatures with the presence of carbon-bearing materials, i.e. carbon monoxide or charcoal, with the motivation to achieve harder surfaces. Fifth, induction hardening [30-32] is a non-contact heating process using electromagnetic induction to produce heat inside the surface layer of components, followed by immediately quenching, enhancing the surface hardness. With the surface modification strategies above, the surface properties can be significantly improved, which greatly broadens the applications of the materials.

Recently, laser surface engineering has been widely used for tailoring the composion or microstructures/phases to improve surface properties of workpieces. Due to the characteristics of high coherence, outstanding directionality, high energy density, and the excellent spatial resolution, laser is the ideal tool to deposit coatings on small sized components [33-35]. Superior to conventional surface engineering strategies, laser surface engineering process is less time/energy/material consuming, more precise and flexible, and has simplified processing procedures (without complex heat treatment steps). In addition, laser surface engineering is not restricted by the slow solid-state diffusivity limitations. Unlike the near-equilibrium processes in conventional cases, due to the extremely fast cooling rate of the laser processing, non-equilibrium characteristics of can be expected, with typical hierarchical microstructures, non-equilibrium phases, supersaturated solution state, etc. [36, 37]. Owing to the obvious advantages, laser surface engineering has been successfully applied in various materials, i.e. titanium alloys [38, 39], aluminum alloys [40, 41], stainless steel [42, 43], magnesium alloys [44], and copper alloys [45].

Titanium and its alloys have many excellent properties, such as superior bio-compatibility, high strength-to-weight ratio, and high corrosion resistance, and have been widely applied in automobile, aerospace, medical and chemical industries [46]. However, due to the low surface hardness, titanium and titanium alloys show poor tribological property and wear resistance. Meanwhile, recent studies pointed out that when planted within the host, titanium and its alloys (i.e. Ti-6Al-4V) showed the potential of ion leakage, leading to elevated serum metal ion levels [47]. Therefore, the surfaces of titanium and titanium alloys need to be modified for better performance. Laser surface enginnering has been widely applied in titanium surface modification, including laser surface remelting [48], laser surface nitridation [49], and laser surface oxidation [50]. Laser surface remelting process is performed in inert atmospheres (i.e. pure argon) to melt titanium (or its alloys) surface to achieve a defect-free and composition

homogeneous surface layer, which is beneficial for improving corrosion resistance [51]. In the meantime, surface roughness was also tailored, for example microgrooves were reported achieved after laser irradiation, which improved osseoinegration when planted in the host [52, 53]. Due to the extremely fast cooling rate of the process, non-equilibrium characteristics was achieved, i.e. the fine microstructures, acicular matensitic phases [54, 55], increasing the surface hardness and improving the wear resistance [51, 56-58]. Laser surface oxidation is commonly performed under pure oxygen or air atmosphere, during which titanium oxides, such as TiO_2, will form on the surfaces of the components, which improves the corrosion resistance and biocompatibility of the parts [59, 60]. Laser surface nitridation are the most widely applied strategy for improving the surface properties of titanium and its alloys due to the excellent properties of titanium nitrides, i.e. superior hardness/stability, high corrosion resistance, and good biocompatibility, which can be used for triboligical and biomedical applications [38, 61-75]. The laser surface nitridation process is mainly performed under pure N_2 or dilute N_2 atmosphere (air atmosphere or mixture of N_2 and inert gas). After laser nitridation, three regions generate on the titanium surface, namely laser melted region (typically contains high volume fraction of titanium nitrides), heat affected region, and the base metal/alloy region [62, 63, 66]. Till now, many types of titanium alloys have been modified with laser nitridation, for example, pure Ti [59, 76, 77], Ti-6Al-4V alloy [63, 64, 66, 67, 78, 79], Ti–45%Nb alloy [61, 80], Ti-6.5Al-3.5Mo-1.5Zr-0.3Si alloy [62], Ti-35Nb-7Zr-6Ta alloy [65], Ti–1Al–1Mn [81], and TiNi alloy [82].

According to the literature review above, large quantities of research work has been performed on laser nitridation/oxidation of titanium alloys, which, however, mainly focused on the reaction products after laser nitridation/oxidation. Little research work has been conducted to investigate the *in-situ* reaction information of laser nitridation/oxidation process of titanium. Such knowledge should provide significant guidance for designing laser surface

nitridation or oxidation of titanium and its alloys. In view of this, one of the main goals of the author's research work was to reveal the dynamic reaction steps between tiatnium and nitrogen/oxygen under laser irradition conditions with the help of *in-situ* synchrotron X-ray testing.

Laser powder bed fusion additive manufacturing. Achieving near net-shape components with one-step manufactring is one of the major goals of material processing. Fortunately, additive manufacturing provides a feasible strategy to fulfill this, which paves the way to the next industrial revolution [83]. Laser powder bed fusion is one of the most prevalent additive manufacturing strategies, which is typically applied for metallic materials [84]. Contrast with traditional substractive and formative manufacturing processes, laser powder bed fusion additive manufacturing is designed to enable the layer-by-layer production of net-shaped parts with complex shapes (based on three-dimentional CAD models) directly from metal powders [85-87]. And with the small laser spot sizes (several tens of microns) and high laser power, both the improved manufacturing resolution, surface finish and incrreased building rate could be achieved [88]. With the brilliant characteristics of laser powder bed fusion, more and more materials are being prepared and investigated, such as titanium alloys [16, 89-92], aluminum alloys [93-95], nickel-based alloys [96-98], copper alloys [99-101], and stainless steels [102-104].

Copper and its alloys show excellent electrical and thermal properties, and are widely used as functional materials in electroic industry, such as heat sink materials [100, 101, 105, 106]. However, due to the high thermal conductivity, as well as the low absorption coefficient of laser irradiation (around 25% with laser wavelength 1030-1080 nm), fabricating copper or its alloys with laser powder bed fusion process is of great challenge [106]. Due to the low coupling of laser-energy on the metal-powder surfaces, defects such as incomplete melting or pores would exsit inside the as-fabricated material. Therefore, high-power laser powder bed

fusion facilities are need to prepare high-density components. Meanwhile, adding some alloying elements are also beneficial for improving the laser-energy absoption coefficient of copper alloys. For example, CuCrZr alloy was reported showing a laser absorption coefficient of around 37% [101, 107-109], which has become an attractive copper alloy for laser powder bed fusion investigation. However, even a tiny addition of alloying elements in the copper matrix would lead to a significant reduce of thermal and elctrical properties due to the interaction between free electrons and solute atoms [110-112]. To tackle this problem, heat treatments are usually performed to precipitate the solute atoms to improve the electrical/thermal conductivity and mechanical strength simultaneously. Hatakeyama et al. [113] performed aging and reaging heat treatments on the Cu-0.78%Cr0.13%Zr alloy, and it was reported that after the primary aging at 460 ℃ for 3 hours, Cr clusters are observed together with Zr element, and after the reaging treatment at 600 ℃ for 1 hour spherical precipitates generated. And the precipitates are mainly pure Cr, while the Zr, Si and Fe element enriched around the pure Cr precipitates, forming a sandwich structure. Zhang et al. [114] conducted a two-stage cryorolling and an intermediate aging treatment on the Cu-1Cr-0.1Zr (wt%) alloy, specifically primary 30% thickness reduction, intermediate aging treatment at 450 ℃ for 2 hours, and finally with a secondary 60% thickness reduction at cryogenic temperature. And a improved combination of electrical conductivity (67% IACS) and tensile strength (690.13 MPa) were obtained. Cu-0.26Cr-0.15Zr, Cu-0.13Cr-0.41Zr, and Cu-0.34Cr-0.41Zr (wt.%) were also investigated, and the solution treatment + cold working + aging is the superior post treatment process, for the precipitates preferentially generate at the dislocations and subcells. And a best combination of tensile strength (599 MPa) and electrical conductivity (82% IACS) were achieved [115]. Sağlam et al. [116] performed solution treatment (900 ℃ for 1 hour) and aging treatment on Cu-0.65Cr-0.07Zr (wt.%) alloy, and it was reported that when aging at 500 ℃ for 2 hours, the best wear resistance was observed. Tu et al. [117] studied Cu-0.4Cr-0.2Zr alloy

with aging treatment, and it was found that the heat treatment showed significant influence on the microstructure, hardness, and wear resistance. When aging at 500 ℃ for 2 hours, the highest wear resistance was observed in their research. Lin et al. [118] carried out two-step aging treatments on Cu-0.22Cr-0.24Zr alloy, after the treatment of 440 ℃ × 15 h + 470 ℃ × 5 h, an excellent combination of tensile strength (~380 MPa), yield strength (~275 MPa) and electrical conductivity (~86.2 IACS%) were obtained. Recently, CuCrZr alloy was also fabricated by laser powder bed fusion method [101]. In their study, due to the characteristic fast cooling rate of Laser Powder Bed Fusion (L-PBF) process, supersaturated solution state is in the as fabricated samples. Therefore, direct aging treatment was performed on the as-fabricated CuCrZr alloy. After the heat treatment at 450 ℃ for 2 hours, a high hardness of ~185 HV and a high thermal conductivity of ~239 W/(mK) were obtained.

Another representative copper alloy that has been widely investigated is Cu-Sn alloy, which is one of the oldest materials used by human beings. Due to the excellent mehanical property and electrical/thermal conductivity, Cu-Sn alloys have been utilized for bearings, electrical chips and heat sink applications [119]. Paul and Sellamuthu [120] conducted surface modification of Cu-10Sn alloy with gas tungsten arc. After modification, uniformly distributed fine grains were observed in the treated surface layer, and the surface hardness and wear resistance were significantly enhanced compared with the as cast counterpart. Paul and Sellamuthu [121] also evaluated the effect of Sn content on the microstructure, hardness and wear properties of surface refined Cu-Sn alloy treated with gas tungsten arc. With differing Sn content (4, 6, 8, 10, 12 wt.%), no significant microstructure differnece (though refined) was observed for the treated samples, however, the surface hardness increased with the increase of Sn content. High temperature torsion was performed on both Cu-7.8Sn an Cu-23Sn alloy (at.%). It was reported that after the mechanical treatment, significant grain refinement of α phase and partial dissolution of ε phase into the Cu matrix were observed for the Cu-7.8Sn alloy, while

no clear change of microstructure was seen for the Cu-23Sn alloy, which indicates the effect of Sn content on the microstructrues [122]. Šatović et al. [123] investigated the corrosion property of Cu-6Sn alloy by exposing the sample to the 15 mM Na_2SO_4 aqueous solution for 12 days, and they pointed out that Cu-6Sn alloy exhibited superior corrosion resistance to the pure Cu sample, which is most likely ascribed to the presence of tin compounds in the surface layer.

A lot of work was also carried out on studying Cu-Sn alloy prepared with laser powder bed fusion additive manufacturing. Mao et al. [124] successfully prepared Cu-4Sn alloy with selective laser melting technology, and investigated the effects of laser processing parameters (i.e., scanning speed, laser power, and hatch space) on the relative density and Vickers hardness, and figured out that Vickers hardness is mainly determined by laser power. Cu-4.3Sn alloy was also fabricated [125], and the samples were heat treated at 600 ℃ and 900 ℃ for 1 hour. With optimized sample preparation parameters, a density of 97%, a yield strength of 274 MPa, an electrical conductivity of 24.1% IACS, and an elongation of 5.6% were achieved. After heat treatment, yield strength was significantly lowered, while the ductility was remarkably improved due to the recrystallization and the decrease of dislocation density. Scudino et al. [126] preapred highly-dense bulk Cu-10Sn alloy samples with selective laser melting method, and it was found that, compared with casted samples, the samples fabricated with selective laser melting method showed much refined grain sizes (from 5.3 μm to 2.3 μm), clearly enhanced yield strength (from 120 MPa to 180 MPa), ultimate strength (from 220 MPa to 420 MPa), and improved ductility (from 7% to 17%). Cu-10Sn alloy prepared with selective laser melting was also studied by Deng et al. [127], and with a laser energy density of 220 J/mm^2, the best properties were achieved, with the density, hardness, yield strength, tensile strength, and elongation to be 8.82 g/cm^3, 78.2 HRB, 399 MPa, 490 MPa, and 19%, respectively. With the goal of improving the mechanical and thermal performance of Cu-10Sn alloy, carbon

nanotube was added to prepare the Cu-10Sn/carbon nanotube composites using high power lasers. It was reported that the strain hardening, mechanical and thermal properties were imporved after the addition of carbon nanotubes. Cu-10Sn samples with 12 vol.% of carbon nanotubes showed much improved performance, specifically, 80% enhancement of Young's modulus and 40% improvement of thermal conductivity [128]. Cu-Sn alloy with much higher Sn content was also successfully fabricated. For example, Mao et al. [119] prepared Cu-15Sn alloy with selective laser melting, and estabilished a statistical relationship between the laser fabrication parameters (i.e., laser scanning speed, laser power, and hatch space) and the density of the fabricated samples. Due to the extremely fast cooling feature of selective laser melting, fine grains (both cellular and dendrite shapes) generated. Heat treatments were also performed on the as-fabricated Cu-15Sn alloys, and it showed that the as-fabeicated Cu-15Sn alloy possessed higher tensile strength but lower ductility. By comparison, the samples after heat treatments showed much improved ductility, which is proportional to the heat treatment temperature, while no clear tensile strength difference was observed after heat treatments.

Clearly, a lot of research work has been done on copper alloys both fabricated with conventional strategies (i.e., cast) and laser powder bed fusion additive manufacturing. Heat treatments are typically applied for improving the overall performance of copper alloys, for example the mechancal property and conductivity (electrical and thermal). However, based on the literature review above, previous study was mainly foucused on the mechanical property and electrical conductivity of copper alloys both before and after heat treatments, quite limited research work has been done on thermal property. Considering the increasing high-temperature applications of copper alloys prepared with laser powder bed fusion method [129, 130], gaining a knowledge of the high-temperature thermal perfromance is of great significance. Therefore, another research focus of the author was the high-temperature thermal property of copper alloys (Cu-10Sn alloy and Cu-1.5Cr-0.5Zr alloy) prepared with laser powder bed fusion

additive manufacturing. In the meantime, heat treatments (anealing, and aging) were also conducted on the as-fabricated alloys, and the effect of the treatments on thermal property, mechanical performance and corrosion resistance were investigated.

1.2 Outline of the manuscript

This manuscript has seven chapters that are sequentially organized. Chapter 1 shows the introduction and the outline of this manuscript. Chapter 2 to Chapter 4 present the study of laser surface engineering of pure titanium under controlled atmosphere. Chapter 2: the study of laser-surface-processed titanium under pure nitrogen atmosphere; Chapter 3: the study of laser-surface-processed titanium under ambient air environment; Chapter 4: the biocompatibility and corrosion property study of laser-surface-processed titanium under pure nitrogen. In chapter 2 and chapter 3, *in-situ* synchrotron X-ray diffraction study was carried out to reveal the reaction steps between titanium and controlled gas environments. Besides, the laser-processed surfaces were also evaluated in terms of their composition, phase distribution, and microstructures to determine the relation with laser parameters/atmospheric compositions. In chapter 4, the surface composition, microstructures, roughness, hardness, biocompatibility and corrosion property were characterized to determine the critical processing parameters for improved performances of titanium. Chapter 5 includes the design, fabrication, heat treatment and property characterization (compression test, thermal conductivity, and corrosion property) of Cu-10Sn alloy made with laser powder bed fusion additive manufacturing method. Chapter 6 depicts the aging heat treatment and property examination (thermal conductivity and tensile property) of Cu-1.5Cr-0.5Zr alloy with differing fabrication orientations made by laser powder bed fusion method. Chapter 7 indicates the conclusions of the manuscript. In the end, an acknowledgement part is presented.

Chapter 2. Titanium and Nitrogen Interactions under Laser Additive Manufacturing Conditions

2.1. Introduction

Compared with conventional manufacturing strategies, laser-based additive manufacturing has the merits of simplicity, fast production rate, reduced manufacturing cost, and the capability of producing parts with complex shapes. Due to the outstanding features of laser-based additive manufacturing, many types of metal laser additive manufacturing methods have been developed. Two types of direct metal laser additive manufacturing processes have received the most attentions, namely 1) Laser Powder Stream, or LENS®-Laser Engineered Net Shaping™ [131-134], which was developed by Sandia National Laboratories; and 2) Laser Beam Powder Bed processes, including selective laser melting (SLM) of powder thin layers [135-138]. SLM shows the advantage of high precision while LENS possesses the merit of outstanding capability of producing parts with significantly larger sizes. The laser scanning speed of the SLM process is much larger than that of the LENS process, consequently, based on previous study, the melt pool size of the LENS was reported one order of magnitude larger than that of the SLM process [139].

Titanium (Ti) is one of the most popular materials. Due to the excellent corrosion resistance, biocompatibility, and strength-weight ratio, Ti has been extensively accepted for aerospace and biomedical applications [46, 140]. However, Ti is active, which reacts with nitrogen (N_2) especially at elevated temperatures. The laser-based additive manufacturing is a high-temperature process, and it was pointed out that the maximum temperature under laser

This chapter was previously published as Congyuan Zeng, Hao Wen, Henry Bellamy, P.T. Sprunger, Paul J. Schilling, S.M. Guo. "Titanium and nitrogen interactions under laser additive manufacturing conditions", Surface and Coatings Technology, 2019. Reprinted by permission of Elsevier.

irradiation can reach 2400 ℃ [141]. Therefore, titanium nitride is expected to generate when N_2 exists during the laser-based additive manufacturing process. To alleviate the nitridation tendency of Ti (or its alloys) produced by laser additive manufacturing processes, pure argon (Ar) is typically utilized to act as shielding gas. Within a typical SLM system, the residual content of oxygen (O_2) lower than 0.3% or even 0.1% is considered safe to start the manufacturing process. However, surfaces of some Ti alloys are also deliberately processed to form a nitride coating for certain applications, and laser nitridation is one of the popular processes [142, 143]. Laser nitridation on Ti-4V-6Al sample surface in pure N_2 gas-flow was investigated by Mridha and Baker [144], and it was pointed out that the content of titanium nitrides went up with the increased laser energy density and N_2 gas flow. Laser surface nitridation modifies and improves the surface properties through tailoring the surface microstructures and/or compositions. For example, it was reported that when the Ti-6Al-4V sample surface was irradiated by laser under pure N_2 environment, the corrosion resistance of Ti-6Al-4V in HCl solution was improved due to the titanium nitride layer generated on the sample surface [145]. Man et al. [146] studied laser diffusion nitridation on Ti-6Al-4V sample surface with varying laser scanning speeds and laser powers in pure N_2 flow. And it was found that the hardness, friction and wear performance of the samples were significantly improved with the optimized laser parameters. A thick titanium nitride layer (tens of microns), produced with a slow laser scanning speed (a few to tens of millimeters per second, commonly found in the LENS process) can be utilized for tribological applications [147]. Besides, it was reported that the microstructure of such a titanium nitride layer was a pure TiN layer on top of a mixed layer where hard TiN dendrites are embedded in a Ti matrix [148]. However, with a fast scanning speed, the nitridation process is expected to be incomplete; in other words, the sample surface may not be covered by thick and dense TiN layer. Recently, Ti surfaces partially covered with TiN coatings were investigated by Dahotre et al. [149], and it was reported that

TiN volume fraction was less than 10% on the surface. With a partially grown TiN layer, the corrosion resistance, osseo-integration, and tribological performances of Ti-6Al-4V alloy samples were improved. Meanwhile, a small amount of addition of oxygen (0.2-0.4 vol.%) in the commercially pure (CP) Ti prepared by SLM method was discovered beneficial for enhancing mechanical strength [150]. Attar et al. [151] pointed out that pure Ti samples prepared by SLM method showed improved wear resistance than the casted counterparts, owing to the finer grain size, martensitic microstructure and enhanced microhardness of the sample. Further studies was performed by Attar et al. [152] to investigate the microhardness of Ti and Ti-TiB composite materials with nanoindentation method, and it was discovered that Ti-TiB showed higher hardness and elastic modulus than Ti due to the reinforcement of TiB. Correspondingly, it is reasonable that the enhanced mechanical properties may also be obtained by producing Ti-TiN composite with SLM. For the purpose of bone in-growth, Mullen et al. [153] reported the research of a novel porous Ti structure made by SLM. It was announced that optimized SLM structures could enhance bone in-growth and would be promising for orthopedic applications.

However, the formation of thick titanium nitride layers was the main focus of previous laser nitridation studies [144-148], very limited work has been performed on the early stage of nitride formation on laser AM parts under laser additive manufacturing conditions. To fill this knowledge gap and to better understand the nitridation process design under typical laser additive manufacturing processing conditions, the motivation of this chapter is to investigate the dynamic reactions between Ti and N_2 under differing laser additive manufacturing processing conditions.

2.2. Experimental Section

2.2.1 Nitridation process with a slow laser scanning speed and In-situ synchrotron X-ray diffraction study

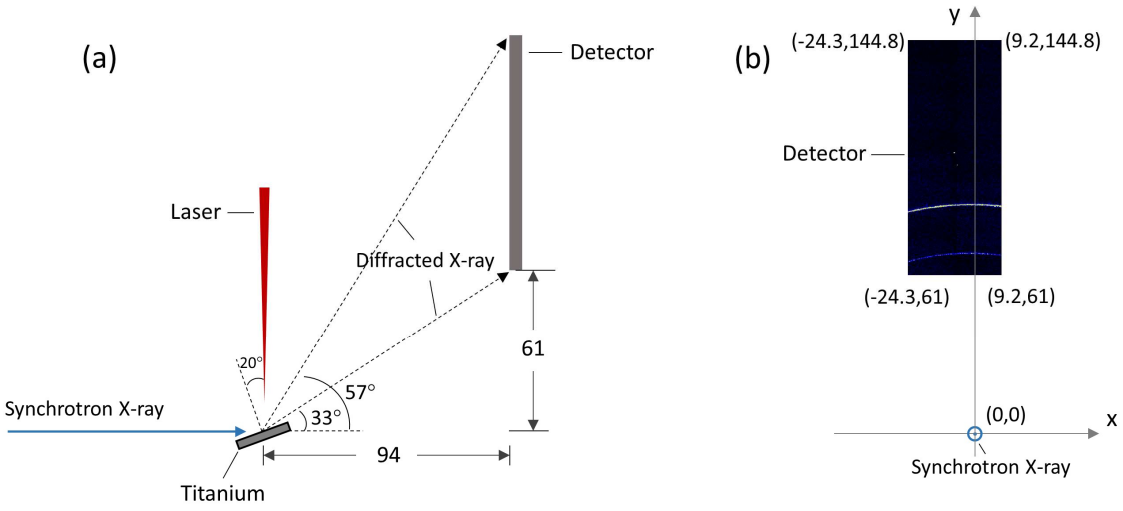

Figure 2.1. Images describing the configuration of the *in-situ* synchrotron X-ray diffraction setup, with the unit of millimeter (mm).

Pure Ti powders were utilized as the raw material (99.5 wt.% purity, ~325 mesh, Alfa Aesar), and were first cold pressed with a stainless steel die into a disk (Φ25.4 × 2.5 mm^3) using a pressing machine (type 16T, MTI), with a pressure of 100 MPa and a holding time 60 secs. A custom rig, comprising three main parts, namely the laser heating source, synchrotron X-ray beam, and a 2D detector, was designed for the in-situ synchrotron X-ray diffraction (SXRD) test. The synchrotron beam line utilized in this study is located at the Center for Advanced Microstructures and Devices (CAMD), Baton Rouge, Louisiana, USA, which is the synchrotron X-ray diffraction research center for Louisiana State University. The synchrotron beam (energy about 8.9 keV) provides X-ray with a wavelength of 1.3808 Å, which is generated from a 1.3 GeV electron storage ring. The synchrotron X-ray beam size irradiated on the sample surface can be adjusted with slits, with the minimum size of 0.3 mm × 0.3 mm. An IPG fiber laser (type YLS-2000, maximum power 2000 W, Gaussian energy distribution, and continuous wave mode) was used as the heating source. To ensure the laser beam spot covering the X-ray beam spot, laser beam was defocused to achieve a spot size of 0.8 mm on

the sample surface (diameter). A PILATUS 100 K detector system (Dectris AG, Switzerland, maximum framing rate 100 HZ) was used for the SXRD data recording.

The *in-situ* SXRD follows Bragg's equation, $2d \cdot sin\theta = n\lambda$, where d, θ, n and λ indicate interplanar spacing of the tested sample, half diffraction angle, positive integer and incident X-ray wavelength, respectively. Before the characterization, to avoid slippage, the cold-pressed Ti powder disk was attached with an adhesive bond to an aluminum sample holder. The laser beam direction was set vertical to the synchrotron X-ray beam. To ensure an effective interaction between the synchrotron X-ray beam and laser beam spots on the sample surface, the sample holder was tilted (with the surface normal) 20° to the laser beam direction (indicated by Fig. 2.1 (a)). The detector window was rectangle shaped (83.8 × 33.5 mm^2), with the long side oriented parallel to, while the short side vertical to the laser beam direction (y axis in Fig. 2.1 (b)). The sample to detector distance (horizontally) was 94 mm, and the distance from the X-ray beam to the bottom of the detector was 61 mm (vertically). The X-ray beam was not strictly (also not necessarily) on the vertical center axis of the detector, which is shown in Fig. 2.1 (b). When taking the position of the X-ray beam as (0, 0), the position of the bottom left corner was determined (-24.3, 61). Approximately 1 sec before the initiation of laser, the X-ray beam and the detector (with framing rate of 10 Hz) were simultaneously switched on to begin recording the diffraction information (diffraction angle and intensity). Afterwards, the laser beam was turned on to heat the sample up with the programmed profile. The laser power was first increased to 200 W with a constant rate of 40 W/s in 5 seconds, with a holding time at 200 W for 1 second, finally declined to 0 W with a fixed rate of -200 W/s in 1 second. After the laser was switched off, the X-ray beam and the detector were kept on working for about 4 more seconds. The whole testing process lasted for 12 seconds (corresponding to 120 frames recorded) and was under pure N_2 gas flow.

2.2.2 Nitridation process under SLM representative conditions

A custom SLM device was used to subject Ti samples under differing gas environments and laser processing parameters, which had a 200W fiber laser (IPG ytterbium, continuous mode, Gaussian energy distribution) with the wavelength 1064nm. A ProSeries II scan head was used to control the scan patterns. A JENar F-Theta lens was used to reduce the laser spot size to 46 μm at the focal plane. With the fixation of laser powder (175 W) and spot size (0.207 mm), melt pool sizes as well as cooling rates are determined by laser scanning speed. Four laser canning speeds, namely 25, 100, 400 and 1600mm/s, were selected. To examine the effect of N_2 contents on the nitridation process, six different N_2 contents, i.e. 0%, 5%, 20%, 50%, 75% and 100% (balance of Ar) were studied. The total pressure of the gas environment was kept at one atm.

2.2.3 Sample characterizations

The compositions, phases, and microstructures of the laser processed samples were characterized. Cross sections of molten tracks (vertical to the laser scanning direction) were cut using a BUEHLER low speed saw. Afterwards, the cross sections were ground using SiC papers with the differing sizes (i.e. 320, 600, 800, 1000 grit sequentially), then polished with diamond suspension (MetaDi™ Supereme polycrystalline, 1 μm), followed by ultrasonically rinsed successively in acetone, ethanol and deionized water for 20 min each. Finally, the polished sample surfaces were etched with the etching solution (Kroll's Reagent, PACE Technologies) for 20 secs. Scanning electron microscope (SEM, Quanta™ 3D DualBeam™ FEG FIB-SEM) was utilized to observe the microstructures of the laser processed areas, and the determination of the molten track geometries. X-ray diffraction (XRD, PANalytical) was used to analyze phases of laser processed surfaces. According to the intensities of the strongest diffraction peaks of the phases and the Reference Intensity Ratio (RIR) values acquired from

the standard powder diffraction file (PDF) cards, the relative amounts of all phases were calculated with Equation (2-1).

$$w_x = I_x/(K_x(I_1/K_1 + I_2/K_2 + \cdots + I_x/K_x)) \quad (2\text{-}1)$$

where w, I and K are mass fraction, diffraction intensity of the strongest peak and RIR value of each phase, respectively, the subscripts indicate different phases. X-ray photoelectron spectroscopy (XPS, Kratos AXIS 165) was utilized to examine the surface compositions. To reduce contaminants from the sample surfaces, Ar^+ sputtering was applied in the XPS tests.

2.3. Results and discussions

Differing laser nitridation conditions (through varying laser scanning speeds), to mimic both LENS and SLM laser AM conditions, were applied onto Ti samples under different N_2 environments. The characterization results of phases, compositions, and microstructures of laser-scanned surfaces are described below.

2.3.1 Dynamic interaction process of Ti and N2 using in-situ SXRD

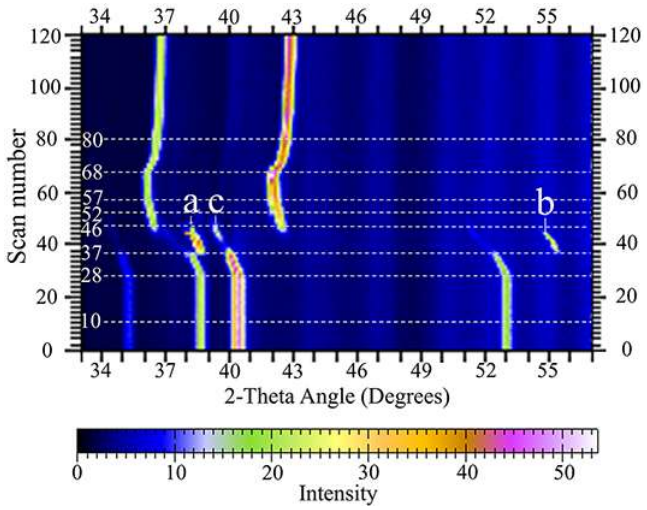

Figure 2.2. Image depicting the *in-situ* diffraction angle and intensity as a function of time frames, a, b represent the diffraction peaks of β-Ti, c is the diffraction peak of α-Ti.

Figure 2.2 shows the SXRD results (analyzed by software FIT2D), indicating the variation of diffraction angles and intensities as a function of frame number (time). Considering

a 10 Hz sampling rate was applied, a total of 120 frames representing 12 secs. The initial time zero was set arbitrarily around one sec before the start of laser heating. With a close observation of Fig. 2.2, the Ti and N_2 interactions can be treated into four stages.

Stage 1 (y = 0-10 and 10-28) shows the diffraction information (angles and intensities) at about room temperature, revealing the diffraction patterns of pure Ti. Based on the initiation point of laser irradiation, stage 1 can be divided into two periods, namely time frames from 0 to 10 (period 1) and time frames from 10 to 28 (period 2). In period 1, the sample stayed at room temperature before laser initiation. At frame 10, laser heating was initiated. Within period 2, the laser power went up from 0 to 72 W linearly. However, the programmed increase of laser energy did not cause a noticeable variation of XRD peaks, indicating negligible temperature variance on the sample surface.

Stage 2 (y = 28-37 and 37-46) depicts the temperature rising period under laser irradiation on Ti sample surface. Obviously, diffraction peaks continuously move to the lower 2θ value side (frames 28 to 37). Based on Bragg's equation, $d = \lambda/(2dsin\theta)$, decrease of θ reveals an increase of the interplanar spacing value, *d*. At low temperature, the crystal structure of Ti is close-packed hexagonal (HCP), the relationship between interplanar spacing, and lattice parameters is described by the following expression.

$$d = 1/\sqrt{4(h^2 + hk + k^2)/3a^2 + 1/c^2} \quad (2\text{-}2)$$

where *h*, *k* and *l* are miller indices, and a, c are lattice parameters for HCP crystals. At high temperatures, β-Ti and the generated TiN phase belong to cubic space groups. In this case, the interplanar spacing is proportional to lattice parameter, and the relation is shown below,

$$a = d\sqrt{h^2 + k^2 + l^2} \quad (2\text{-}3)$$

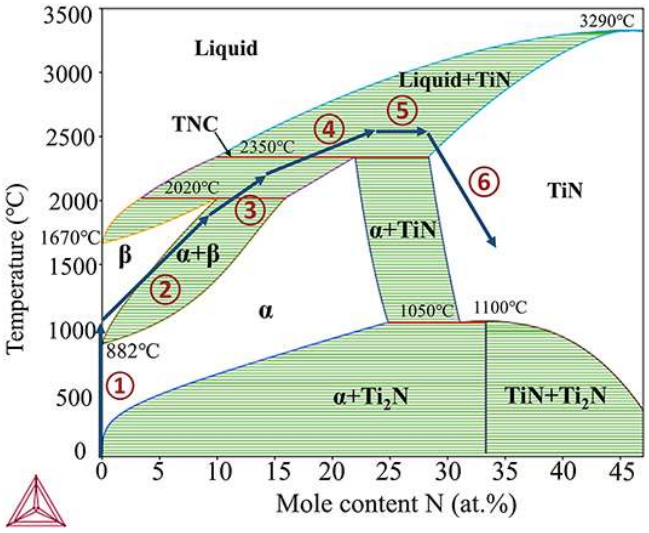

Figure 2.3. Titanium-nitrogen phase diagram. Phase transformation steps ① αTi→βTi. ② βTi→αTi+βTi. ③ αTi+βTi→liquid+αTi. ④ Liquid+αTi→liquid+TiN. ⑤ Liquid+TiN. ⑥ Liquid+TiN→solid+TiN.

According to equations 2-2 and 2-3, the increase of lattice parameters results in an increase of interplanar spacing, and vise versa. As laser irradiation continued, temperature on the sample surface increased, leading to thermal expansion of the sample. If both diffraction angles and the corresponding temperatures can be precisely measured, *in-situ* thermal expansion can then be determined. At around frame 37, a critical temperature was reached, where abrupt changes of diffraction angles and intensities were captured, which result from the fact that pure Ti transforms from HCP structure, αTi, to body-centered cubic (BCC) structure, βTi when the temperature reaches about 882°C [154]. In Fig. 2.2, points a and b correspond to diffraction peaks of βTi, while point c indicates αTi's diffraction pattern, which lies on the extrapolating line of the diffraction patterns of αTi phase at lower temperatures. Despite the abrupt change in diffraction intensity described above, weak diffraction patterns of αTi are still observed. The signal of αTi became even stronger from time frames 40 to 46, indicated by point c, which demonstrated an increase of αTi. This observation is quite interesting, because for pure Ti, a change from αTi to βTi is expected when reaching the phase transformation

temperature (~882 ℃). The coexistence of α and β phases is ascribed to the presence of nitrogen in the structure. Based on Ti-N phase diagram in Fig. 2.3 (calculated by ThermoCalc^{TM} software), as temperature increases, the solubility of nitrogen in Ti increases remarkably. Besides, it was also reported that nitrogen plasma can be induced by the laser during the laser nitridation process [155], accelerating the diffusion of nitrogen into Ti, and increasing nitrogen content in the Ti surface area.

Therefore, different from the constant nitrogen content situation, in which case the Ti transits from α to α+ β, and then to β phase, the pure Ti first underwent the α to β phase transformation at time frame 37. With the rapid absorption of nitrogen at high temperatures, the system was brought into the α+β two-phase area. When temperature kept increasing, nitrogen intake into the Ti sample was accelerated, and more αTi generated from βTi. That explains the reason why the intensity of αTi was enhanced around point c (Fig. 2.2) from time frames 40 to 46. With the further increase of nitrogen content and temperature, βTi melted or transformed to αTi phase, and TiN started to form rapidly. The majority of Ti entered Liquid+αTi two-phase region, while small amount of Ti started entering Liquid+TiN two-phase area. At time frame 46, the coexistence of αTi and TiN phases was detected by the *in-situ* SXRD test, which can be explained by the transient nitridation curve (TNC) indicated on Fig. 2.3 (~ 2350℃). Besides, the non-uniform temperature distribution on the X-rays illuminated area could be another reason. Due to the Gaussian energy distribution of the laser, the center of the laser beam showed a higher power density, which led to higher temperature appeared at the Ti surface area that interacted with the laser spot center, at which the Liquid+TiN two-phase appeared first. With the further increase of temperature and more progress of nitridation, the TiN layer was thick enough to dominate the synchrotron X-ray diffraction pattern.

Stage 3 (y = 46-52, 52-57, and 57-68) indicates a TiN layer floating on a molten Ti. During this stage, temperature went even higher as the diffraction peaks of TiN further shifted toward smaller angle side. Meanwhile, more nitrogen was absorbed and reacted with liquid Ti, leading to the further enhancement of diffraction intensity of TiN. Within time frames 52-57, a further increase of temperature was observed from the shift of the TiN diffraction patterns. The TiN diffraction intensity, however, remained nearly constant, which could be ascribed to the reduced nitrogen diffusion rate through the already thickened TiN layer. Over the time frames 57-68, little variance was observed on diffraction angle, indicating that with the used laser processing profile, temperature of the molten spot kept nearly constant as the laser irradiation power was balanced with heat losses from the sample surface due to radiation and conduction.

Stage 4 (y = 68-80) describes the solidification process. Clearly, only TiN diffraction peaks were detected, no new phases generated, which is similar with stage 3. Diffraction peak shifts towards the large angle side due to contraction during the cooling down stage.

In summary, according to the *in-situ* SXRD results, diffraction peak shifts were observed during the laser heating and cooling processes. With an accurate measurement of the shift of the diffraction angles, an *in-situ* thermal expansion coefficient could be calculated when the corresponding temperature could be measured. A slow laser scanning speed leads to a long laser dwelling time, which is beneficial for the formation of a complete TiN layer. The nitridation process occurred quickly once the temperature approached the melting point of Ti. A thick TiN layer was rapidly generated to the penetration thickness of synchrotron X-ray within 0.6 second (time frames 46 and 52). And the thickness of the TiN layer was reported around 5.5 μm based on the study of Valvoda and Musil [156]. The X-ray beam energy in the present study was 8980 eV, therefore, the attenuation length in solid TiN was about 16 μm. Considering the diffraction setup, when the TiN layer formed on Ti surface is over 5.5 μm,

only TiN signal can be detected. During the Ti-N_2 interactions, the Ti sample surface underwent the following phase transformation steps, αTi→ βTi→ αTi+βTi→ liquid+αTi→ liquid+TiN→ solid+TiN.

2.3.2 Effect of laser scanning speed on phases, compositions, and microstructures of Ti

2.3.2.1 The laser processing parameters and the resulting molten tracks

Laser power selected in this study was 175W, together with spot size of 0.8 mm. The hatch spacing was determined by single track study (quantifying the molten track geometries) with different laser scanning speeds.

The SLM system processing chamber was first evacuated down to 145 Pa, then refilled with pure Ar to atmospheric pressure. Fig. 2.4 illustrates a group of single laser scanning tracks with differing scanning speeds, together with the representative melt pool morphology processed with a laser scanning speed of 25 mm/s. Based on Figs. 2.4 (a)-(d), the width of the laser track decreased as the scanning speed increased, with the detailed results listed in Table 2.1. Interestingly, with the increase of scanning speed, the ripple line on the molten track was elongated towards the laser scanning direction. The ripple line was even elongated to be two parallel lines when the scanning speed reached 1600 mm/s. Cross sections of the scanning tracks (perpendicular to the laser scanning direction) were sectioned, ground, and polished, then etched in the etching solution (Kroll's Reagent, PACE Technologies) for 15 secs. And the revealed cross section of the melt pool is shown in Fig. 2.4 (e), with a semi-elliptical shape, indicating the conduction mode of laser irradiation [157]. The shallow penetration depth of laser melting was due to the large laser spot size on Ti surfaces, which dramatically lowered the laser power density. Based on the molten pool sizes, hatch spacing was determined and summarized in Table 2.1. To achieve full molten track coverages on the sample surfaces, the overlapping rate was slightly above 50%.

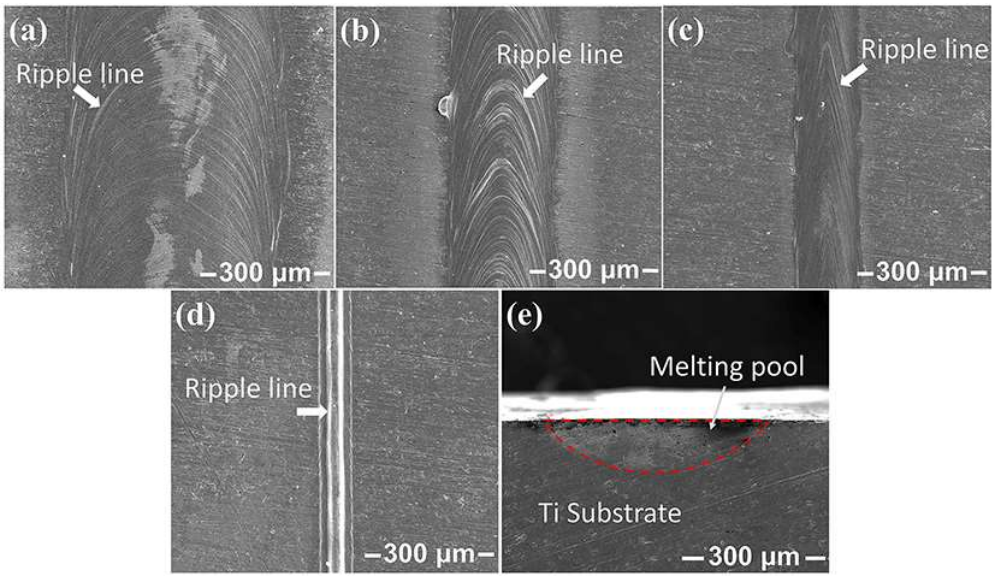

Figure 2.4. Images showing the single laser scanned tracks with differing scanning speeds, (a) 25 mm/s (b) 100 mm/s (c) 400 mm/s (d) 1600 mm/s, and the melt pool cross section morphology of the sample irradiated with the speed of 25 mm/s (e).

Table 2.1. Melt pool sizes and the determined hatch spacing under varying laser scanning speeds

Parameter	Value			
Scanning speed (mm/s)	25	100	400	1600
Melting pool width (μm)	473 ± 15	252 ± 5	151 ± 2	75 ± 2
Melting pool depth (μm)	93 ± 3.5	55 ± 1.0	34 ± 0.4	16 ± 0.5
Hatch spacing (μm)	230	120	64	35

2.3.2.2 Effect of laser scanning speeds on composition and phases of Ti

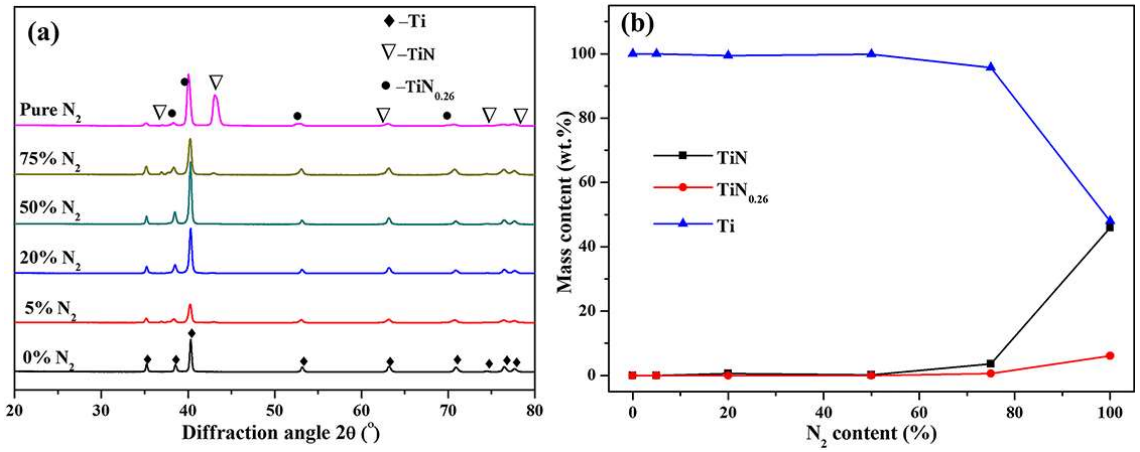

Figure 2.5. Images displaying XRD results and phase compositions of the samples. (a) depicts the XRD results with differing scanning speeds under pure N_2 atmosphere. (b) indicates the phase compositions on the sample surfaces.

With the laser parameters shown in section 2.3.2.1, Ti samples were processed under pure N_2 atmosphere using four differing scanning speeds, namely 25, 100, 400 and 1600 mm/s. The XRD results are presented in Fig. 2.5. According to Fig. 2.5 (a), titanium nitrides, i.e. TiN and $TiN_{0.26}$, in addition to α-Ti phase were found on the surfaces of all the samples. Obviously, diffraction peak intensities of titanium nitrides decreased with the increase of scanning speed, in other words, the ratio of the strongest diffraction peak intensity of TiN, i.e. diffraction angle ~43°, to that of α-Ti, diffraction angle ~40°, declined monotonously, indicating the declining content of titanium nitride. Fig. 2.5 (b) depicts the calculated mass amount of all phases, Ti, TiN and $TiN_{0.26}$, under differing scanning speeds. With the increase of scanning speed, the mass content of titanium nitride decreased, while α-Ti increased. Specifically, when the scanning speed went up from 25 mm/s to 1600 mm/s, the content of TiN decreased from 82.2% to 13.7%, while that of $TiN_{0.26}$ declined from 15.5% to 1.6%. Correspondingly, mass concentration of α-Ti increased from 2.3% to 84.8%. The above observation can be explained below. Firstly, a slower laser scanning speed leads to longer laser-sample interaction time. As a result, Ti remained in the molten state longer to react with N_2. Second, a longer laser-sample interaction time makes more energy absorbed by the sample, resulting in a higher temperature, which enhanced the reaction between Ti and N_2, consequently increasing the mass amounts of titanium nitrides on the surface.

The scanning speeds of 25 mm/s and 100 mm/s represent the LENS process, while the scanning speeds of 400 mm/s and 1600 mm/s match the SLM process better. Clearly, nitridation to a certain degree can still be observed with fast scanning speed, for example 1600mm/s in this study, if a SLM system uses pure N_2 in the processing chamber. For SLM conditions, laser-sample interaction time was two orders of magnitude less than that of the LENS process. Within the limited laser-sample interaction time, the temperature of the laser-sample interaction spot was not as high as that of LENS condition. Shorter interaction time and

lower temperature resulted in a thin or discontinuous titanium nitride layer. For the LENS method, taking the laser scanning speed of 25 mm/s and a molten pool size of 0.5 mm, the dwelling time was 20 ms. Within 20 ms, a layer with more than 80% TiN could be formed.

2.3.3 Effect of controlled N2 environments on phases and composition

The influence of controlled N_2 environments on the phases and compositions of Ti samples processed under representative SLM conditions was investigated. Table 2.2 lists parameters that were used to process the samples. According to XRD results (Fig. 2.6 (a)), diffraction peaks of TiN was obvious when N_2 content was 100%. However, diffraction peaks of TiN were negligible when N_2 content was below 75%, indicating significantly reduced titanium nitride on the sample surfaces. Quantitative analysis was conducted with the XRD results. The relationship between the calculated titanium nitride mass concentration and the N_2 content is displayed in Fig. 2.6 (b). Apparently, less TiN generated on the sample surfaces as N_2 concentration decreased. When N_2 content was low (i.e. from 0% to 50%), TiN and $TiN_{0.26}$ content was neglectable. When N_2 content went up to 75%, the amount of TiN increased from 0.2% to 3.64% and the amount of $TiN_{0.26}$ went up from 0% to 0.65%. When N_2 content reached 100%, an abrupt content increase of titanium nitrides was observed, and the amounts of TiN and $TiN_{0.26}$ were climbing to 45.9% and 6.1%, respectively. Transforming the mass amount of the phases to atomic percentage of single elements, when N_2 content went up from 50% to 100%, nitrogen absorption on sample surface increased from 0.17% to 29.33% (atomic content). This demonstrates the profound effect of N_2 content in the environment on the formation of titanium nitrides.

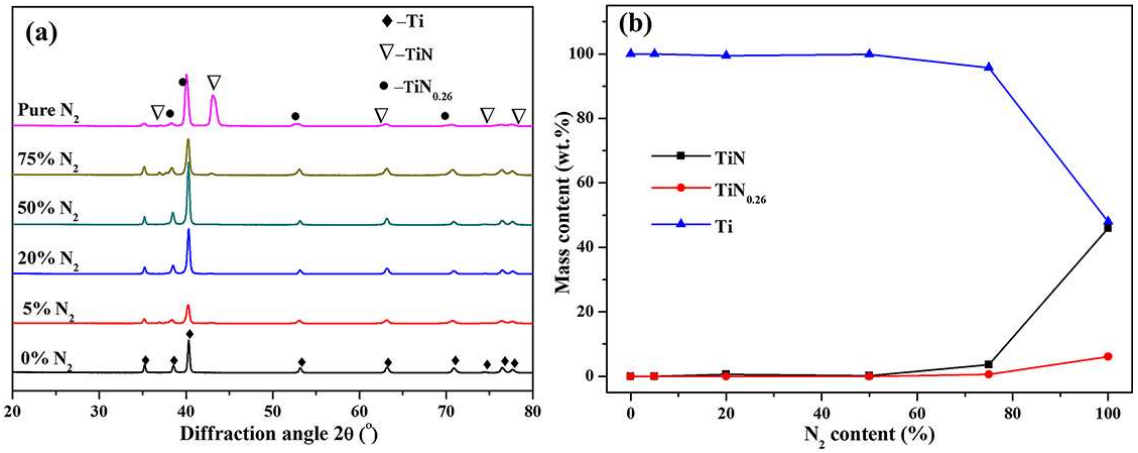

Figure 2.6. Images illustrating XRD and phase composition test results on the sample surfaces. (a) shows the XRD results of the samples treated with controlled N_2 environments, (b) indicates the phase compositions on the surfaces of the samples based on XRD test results.

Table 2.2. Laser parameters for samples made under controlled N_2 atmosphere

Parameter	Laser power (W)	Spot size (um)	Scanning speed (mm/s)	Hatch spacing (mm)
Values	175	207	400	64

2.3.4 Surface compositions of samples tested by XPS.

To find out the more accurate composition of laser scanned surface, X-ray photoelectron spectroscopy (XPS) method was used. The detecting depth of XPS is within 10nm, while detection depth of XRD is in the order of several micrometers. Clearly, XPS reveals the outermost surface compositions, while XRD tells the average composition information with a depth of several micrometers. When exposed to air, Ti reacts with O_2 even at RT due to its active characteristics. To remove surface contaminants (especially titanium oxides), Ar^+ sputtering was applied prior to the XPS testing.

Fig. 2.7(a) shows the relation between the element content on sample surface and the Ar^+ sputtering time, the sample examined here was prepared under 100% N_2 atmosphere. With the increase of Ar^+ sputtering time, Ti content (TC) went up continuously. Correspondingly, it indicated the declining of the total amount of oxygen (O) and nitrogen (N). Specifically, O

content (OC) went down quickly from 63.59% to 15.42% as the sputtering time went up from 0 min to 20 min. However, as the sputtering time further increased to 60 min, OC declined from 15.42% to 8.00% with a clearly slower rate. N content shows clear differing variation behavior. N content (NC) increased from 8.03% to 32.45% as the sputtering time increased from 0 min to 20 min. The above observation indicated that the O element existed mainly on the outermost surface. As the research focus of this study was NC, the sputtering time was set as 20 min.

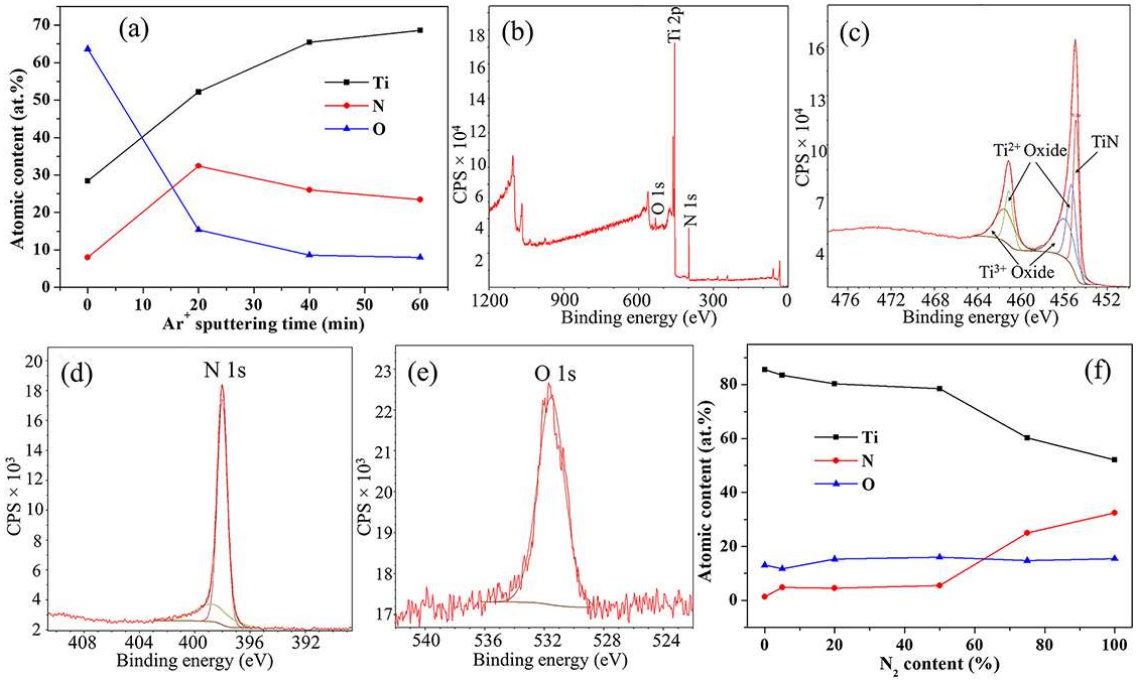

Figure 2.7. (a) displays the relation between Ar^+ sputtering time and surface composition of the sample processed with 100% N_2. (b), (c), (d) and (e) show the XPS survey scan spectra after 20 min Ar^+ sputtering (100% N_2 atmosphere), with (b) full range scan spectra, and narrow scan spectra of (c) Ti, (d) N, and (e) O. (f) indicates the relation between the controlled N_2 atmosphere and sample surface composition. The sample characterized here was processed with laser power, spot size and scanning speed of 175 W, 207μm, and 400 mm/s, respectively.

Figs. 2.7 (b)-(e) depict XPS survey scan spectra of the sample. Fig. 2.7 (b) describes a full range XPS scan spectra, revealing the coexistence of Ti, N and O. Figs. 2.7(c)-(e) are narrow scan results of Ti, N and O, respectively. Based on previous work [158], it was reported that Ti mainly existed as TiN, Ti^{3+} (e.g Ti_3O_2) and Ti^{2+} (e.g TiO). However, little TiO_2 peak

was seen, which might be ascribed to the fact that the outermost surface had been removed by the Ar^+ sputtering. As it went deeper into the sample surface, OC was too little for the formation of TiO_2, instead Ti_3O_2 and TiO generated. N existed in two states, and this observation was in line with the XRD results, where two titanium nitrides, TiN and $TiN_{0.26}$, were observed.

After Ar^+ sputtering for 20 min, the sample surface was tested with XPS. Fig. 2.7(f) shows the relations between the N_2 contents and the element contents on the sample surfaces. Obviously, NC and TC showed opposite variations. Generally, TC declined while NC increased with the increase of N_2 content. Meanwhile, OC stayed nearly constant over the entire N_2 content range (range from 12% to 16%). Most reasonably, oxygen stemmed from the trace amount of O_2 in both N_2 and Ar gas utilized in the study. When there was no N_2 in the chamber, maximum TC and minimum NC on sample surface were observed, (83.45% and 1.38% respectively). When N_2 content increased to 5%, TC declined from 83.45% to 78.49%, while NC went up from 1.38% to 4.77%.

When N_2 content varied from 5% to 50%, NC remained almost the same (around 5%). However, TC decreased slightly (83.45% to 78.49%) due to the tiny increase of oxygen. When N_2 content continuously increased to 75%, a clear jump of NC was observed (from 5.54% to 25%), while TC dropped from 78.49% to 60.28%. When N_2 content reached 100%, maximum value of NC was obtained (32.45%), while the minimum value of TC was achieved (52.13%). Therefore, NC on sample surface increased from 5.54% to 32.45% when N_2 content increased from 50% to 100%. The variation behavior of NC detected by XPS agreed with the results achieved by XRD characterization. However, differences were observed for the 75% N_2 case, where NC detected by XPS was clearly higher than that obtained by XRD. This observation originated from the detection depth difference between the two characterization methods. XPS reflected the outermost surface composition while XRD revealed the average composition with a depth of several microns. To sum up, NC on sample surface can be controlled to a low level

when N_2 content was below 50% (around 5% according to XPS tests). And sample surface was most likely covered by titanium nitrides partially. Therefore, via adjusting N_2 content, controlled phases and composition on titanium surfaces were achieved with SLM conditions.

2.4. Conclusions

This present investigation revealed the dynamic interactions between Ti and N_2 under laser-based AM conditions. The dynamic reaction steps between Ti and N_2 with a slow laser scanning speed, mimicking the LENS condition, was characterized with *in-situ* SXRD method. The nitridation products on the sample surfaces, processed with varying laser scan speeds (indicating LENS/SLM conditions) and controlled N_2 atmospheres, were evaluated for composition, microstructures and phase compositions. The conclusions were achieved below.

(1) Thanks to the SXRD test results, diffraction peak shifts ascribed to thermal expansion or contraction were observed and the high-temperature reactions between Ti and N_2 were revealed. Based on the Ti-N phase diagram, phase changes during the laser processing were depicted as αTi→ βTi→ αTi+βTi→ liquid+αTi→ liquid+TiN→ solid+TiN.

(2) Under pure N_2 atmosphere, the time to form a thick TiN layer, able to block the penetration of synchrotron X-ray, on molten titanium was around 0.6 sec.

(3) Two titanium nitrides (TiN and $TiN_{0.26}$) were observed under laser processing conditions associated with the laser AM conditions and N_2 gas environment. And the content of titanium nitride decreased with the increase of scanning speed.

(4) Nitrogen content on sample surfaces increased with the increase of N_2 content with the same laser parameters. Nitrogen content on sample surfaces was at a low level when N_2 content was less than 50% (under 5% based on XPS results). However, nitrogen absorption on the sample surfaces went up rapidly (from 5.54% to 32.45% according to XPS results) when N_2 content went up from 50% to 100%. Further investigations

concerning mechanical properties prepared under differing N_2 content are worthy to be pursued.

Chapter 3. Diffusion of Oxygen and Nitrogen into Titanium under Laser Irradiation in Air

3.1. Introduction

Due to the outstanding properties, i.e. high strength-to-weight ratio, high corrosion resistance, and excellent biocompatibility, titanium (Ti) and its alloys are widely applied as aerospace and biomaterial materials [159-162]. For many situations, the surfaces of Ti parts are intentionally processed to generate a coating layer, and laser gas alloying is one of the most popular treating strategies. As is shown in Chapter 2, plenty of investigations have been performed on laser surface nitridation, and the TiN layers generated on the surfaces of Ti parts are discovered to enhance tribological performance, surface hardness, biocompatibility, and corrosion resistance [39, 147, 149, 163-165]. Meanwhile, the formation and characteristics of titanium oxide layers have also been considerably studied. Based on a previous study [166], a titanium oxide layer not only can enhance the surface hardness for improved wear resistance, but also can improve the corrosion resistance. Furthermore, it was also reported that titanium oxides (i.e. rutile and anatase titania) can improve bioactivity and biocompatibility of Ti based medical parts [53, 166-168]. With controlled laser energy levels and the gas atmosphere, various surface reaction products with differing colors have been observed after laser surface modification [169-175].

The effect of gas atmosphere, namely air and pure oxygen, on Ti surface modification was investigated [80], it was reported that oxygen absorption on Ti surface was ~36 wt.% and ~38 wt.% when processed in air and pure oxygen, respectively, which showed no significant

This chapter was previously published as Congyuan Zeng, Hao Wen, Boliang Zhang, P.T. Sprunger, S.M. Guo. "Diffusion of oxygen and nitrogen into titanium under laser irradiation in air", Applied Surface Science, 2020. Reprinted by permission of Elsevier.

difference on oxygen insertion despite oxygen concentration difference in the atmosphere. Interestingly, with a low laser energy density (around 2.5 J/cm^2), only TiN phase was detected on the Ti surfaces under air atmosphere [176]. Surface modifications on Ti dental implants were also performed by Braga et al. [69] with a set of laser irradiation parameters under ambient air, intending to produce tailored surface oxides. Several phases on the laser processed surfaces were discovered, including αTi, βTi, Ti_6O, Ti_3O and TiO but no TiO_2 phase was found. However, Pérez del Pino et al. [177] reported the formation of both rutile and anatase TiO_2 on laser processed surfaces in air. To explore the titanium oxide formation mechanism (composition and phase distribution) on Ti surface after laser irradiation, chemical thermodynamic method was investigated [178]. And it was discovered that on Ti surface multilayered composite generated, a thin layer consisting of Ti dioxide appear on the outermost surface, while layers comprising Ti_2O_3 and TiO oxides together with Ti nitride formed in inner layers. The effect of laser wavelength (i.e. 532, 1064 nm) on the incorporation of nitrogen was also evaluated [173], and the wavelength 1064 nm showed a higher efficiency for nitrogen insertion. By comparison, the experimental study results and the theoretical prediction in study [178] (in air atmosphere) were discovered not necessarily in line with each other. With a pulsed laser heating source, with the increase of laser fluence the insertion amount of light elements (oxygen and nitrogen) increased. Besides, Ti oxynitride layers were also generated [179]. Similar results were also reported by Antończak et al. [169], where the top transparent layer was not only pure TiO_2, but also nitrogen and nonstoichiometric compounds.

In many cases, composition distribution and phase constituents of a reaction system can be predicted either by phase diagrams or chemical thermodynamics and kinetics. However, laser processing is unique due to the extremely fast cooling rate, making the laser processed parts in a non-equilibrium state. Therefore, equilibrium prediction is no longer validate in the present, i.e. titanium-nitrogen and titanium-oxygen systems. Moreover, it has also been proved

that the experimental results do not perfectly agree with the theoretical calculations [169, 178, 179], which can be explained by the reasons below. Firstly, contrast with the stationary non-laser heating conditions (equilibrium state due to the uniform temperature distribution and slow heating/cooling rate), laser heating (typically with continuous-wave mode (CW)), due to its extremely fast heating/cooling rates and non-isothermal feature, is a non-equilibrium process [180, 181]. And a complex temperature distribution (or large thermal gradient) results from the dynamic laser scanning and the non-uniform energy distribution of laser spot. Consequently, non-equilibrium/non-stoichiometric generates, which shows significant variance with theoretical calculation. Secondly, the complex air composition makes the reaction products complicated. The oxide and nitride layers generated on the sample surfaces may also have significant effects on the absorption of laser energy [182, 183], make it more difficult to determine the heat absorbed. Finally, considerable residual stress exists in the surface due to the extremely rapid cooling rate, causing structural defects (e.g. dislocations and microcracks), serving as diffusion paths for element (oxygen or nitrogen) intake, consequently modifying the reaction kinetics [169].

The laser-nitridation and -oxidation of Ti (or its alloys) were discovered to be diffusion dominated processes [46, 69, 146, 184, 185]. Considerable amount of studies have been performed to evaluate the reactions between Ti and air, however, nearly all of them were concentrated on the influence of laser parameters on the reaction products. For example, Dahotre [46] pointed out that nitridation was achieved with a laser energy density of 2×10^6 J/m^2 and Man [146] fulfilled nitridation on Ti-6Al-4V surfaces with optimized laser parameters. In order to better understand the laser-Ti interaction process in air, understanding the diffusion of elements (i.e. oxygen and nitrogen) in Ti during laser irradiation (especially at high temperatures) is of great significance. In addition, due to the non-equilibrium feature (unpredictable) of the laser reaction process in air, discovering the dynamic reaction steps

experimentally also becomes urgent. However, to the best knowledge of the author, detailed reaction steps between Ti and air under laser processing have not been fully examined. And the diffusion coefficients of nitrogen and oxygen in Ti (or its alloys) substrate at elevated temperatures (i.e. molten state) are quite limited because previous studies were mainly focused on the diffusion conditions below the melting points of Ti (or its alloy) [186-196]. Therefore, the research motivation of the present chapter is to examine oxygen/nitrogen diffusion into Ti substrate at elevated temperatures over melting point and to find out Ti-air dynamic reactions with typical laser processing conditions.

3.2. Materials and methods

3.2.1 Transient laser processing

The oxidation and nitridation processes between Ti and air were investigated under representative additive manufacturing process conditions, with a wide range of laser scanning speeds (from tens of millimeters per second to several meters per second). Melt pool size with a slow laser scanning speed can be one order of magnitude larger than that of a fast scanning case, which in turn causes a remarkably differing melt-pool dwelling time. To achieve different laser processing parameters on Ti sample surfaces, a custom laser processing system was applied, which comprised a 200 W fiber laser (IPG ytterbium, CW mode, Gaussian distribution, wavelength 1064 nm). With a fixed laser spot size of 58 μm and a fixed laser power of 100 W, four different scanning speeds (25, 100, 400 and 1600 mm/s) were evaluated. Laser scanning patterns were controlled by a ProSeries II scan head, and single laser scanning for each scanning speed was carried out to determine the laser hatch spacing, with which the whole surface coverage was achieved. Commercially pure (CP) Ti pieces (99.2 wt% purity, 10×10×3 mm^3) are used as the target material. Prior to laser irradiation, the sample surfaces were ground with SiC grinding papers (320 and 600 grit, successively). Then the samples were rinsed ultrasonically in acetone, ethanol, and deionized water sequentially for 20 min each.

3.2.2 *In-situ* Synchrotron X-ray diffraction setup

The dynamic high-temperature reaction steps between Ti and ambient air were investigated with *in-situ* synchrotron X-ray diffraction (SXRD) with spatially fixed laser irradiation over time span of several seconds, in which the laser power was programmed to increase to a maximum of 200 W and then decreased. Detailed description of the *in-situ* synchrotron X-ray testing setup can be found in Chapter 2. Ti powders (99.5 wt% purity, ~325 mesh, Alfa Aesar) were applied, which were cold pressed into a disk-shaped sample (Φ25.4×2.5 mm^3) with a stainless steel die.

The X-ray beam was adjusted using slits to a size of 0.3 mm×0.3 mm. Full laser irradiation was applied using an IPG fiber laser (YLS-2000, CW mode, Gaussian distribution) over the X-ray beam/sample interaction zone. To log the diffraction data, a detector system (PILATUS 100K, Dectris AG, Switzerland) with an active area of 83.8×33.5 mm^2 was applied with a framing rate of 10 Hz. SXRD follows Bragg's formula, described as $2dsin\theta = \lambda$, where d, 2θ and λ are interplanar spacing, diffraction angle, and wavelength of the synchrotron X-rays, respectively. The sequential SXRD data obtained during the laser processing were processed with a program named FIT2D, which gave the diffraction information, including diffraction angles and intensities, of the whole process. The synchrotron X-ray and the detector were initiated before the laser heating. About 1 sec later, the laser was turned on with a preset profile with heat-up, soaking, and cool-down periods. For the heat-up period, laser power went up to 200 W in 5 secs; for the soaking period, the power was held at 200 W for one sec; and finally for the cool-down period, the power was declined to 0 W with a nearly fixed rate in 1 sec. The detector and the X-rays were kept on working for around four more secs after the laser's shutdown.

3.2.3 Sample characterization

After laser irradiation studies, the samples were processed for the following characterization. Cross sections of the laser processed samples were cut with a low-speed saw (BUEHLER). Then the sample was mounted using the mixture of SamplKwick powder and liquid with the volume ratio of 2:1, leaving the target cross section uncovered. Afterwards, the sample cross sections were ground with SiC papers (320, 600, 800 and 1000 grit, successively), polished with diamond suspension (MetaDi^{TM} Supereme polycrystalline, 1 μm), and rinsed in acetone, ethanol, and deionized water sequentially for 20 min each ultrasonically. After that, the polished sample cross sections were etched (Kroll's Reagent, PACE Technologies) for 15 s, and finally cleaned with deionized water and dried in air. Microstructure information of the cross-sections were characterized using a scanning electron microscope (SEM, Quanta™ 3D Dual Beam™ FEG FIB-SEM) with an accelerating voltage of 20 KV.

3.3. Results and discussions

3.3.1 Diffusion of oxygen and nitrogen into Ti under laser irradiation

To evaluate the laser-activated diffusion of oxygen and nitrogen into Ti substrates, four laser scanning speeds, namely 25, 100, 400 and 1600 mm/s, were investigated under ambient air environments. In the remainder of this chapter, the samples were denoted as Ti-A25, Ti-A100, Ti-A400 and Ti-A1600, respectively, where "A" indicates air. Laser energy density was determine with the following equation,

$$E = 4 \cdot P \cdot t/(\pi d^2) \tag{3-1}$$

where E, P, t and d represent laser energy density, laser power, laser-sample interaction time and laser spot size, respectively. Laser-sample interaction time is determined with $t = d/v$, where v is laser scanning speed [46]. Therefore, laser energy densities can be determined, which are 87.81×10^6, 21.95×10^6, 5.49×10^6 and 1.37×10^6 J/m^2 on Ti-A25, Ti-A100, Ti-A400 and Ti-A1600, respectively. It was reported that, when the laser energy densities were 1.7×10^6

and 2.12 $\times 10^6$ J/m^2, peak temperatures of around 4400 and 4900 ℃, respectively, would be achieved on Ti-6Al-4V surface [46, 149, 197]. Based on the research results above, it is reasonable to deduce that with the laser energy density 1.37 $\times 10^6$ J/m^2, titanium surface could also be melted.

3.3.1.1 Determination of hatch spacing for laser scanning

Hatch spacing must be determined before laser irradiation. CP Ti pieces were selected as the research material, and a custom laser processing system was utilized to perform laser irradiation. To quantify the molten track geometries, single laser scanning tracks were performed on Ti samples with each selected laser scanning speed. During the laser processing, ambient air environment with a pressure of one bar was applied.

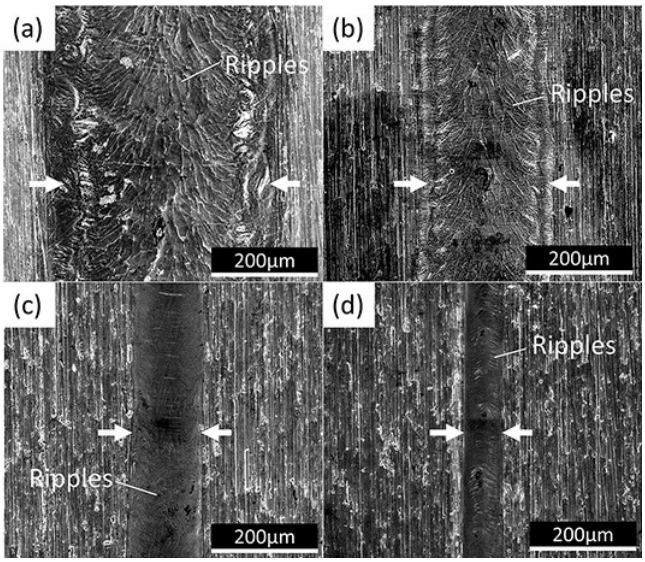

Figure 3.1. Images showing single tracks with varying laser scanning speeds under air environment (100 W) (a) 25 mm/s (b) 100 mm/s (c) 400 mm/s (d) 1600 mm/s. Arrows show the approximate boundaries of the laser single tracks, ripple structures are also indicated.

Figure 3.1 shows a set of SEM images of single-track morphology processed with differing laser scanning speeds, and Table 3.1 displays the detailed measured results. Based on the measured results, hatch spacing (laser overlapping 50 %) can be determined. Ripple structures are observed on all the single tracks, which are indicated in Fig. 3.1. Based on

previous study, this structure was found originated from the fluctuation of melt pool volume [198], indicating the formation of molten state on titanium surfaces during laser processing.

Table 3.1. Laser parameters

Parameter	Value			
Laser power (W)	100	100	100	100
Spot size (μm)	58	58	58	58
Scanning speed (mm/s)	25	100	400	1600
Width of single track (μm)	362 ± 9.1	225 ± 10.9	114 ± 3.7	75 ± 2.9
Hatch spacing (μm)	181	112.5	57	37.5

3.3.1.2 Effect of laser scanning speed on the diffusion of oxygen and nitrogen into Ti

Figure 3.2 demonstrates the microstructures and the composition (energy-dispersive X-ray spectroscopy (EDS) mapping) results of the cross section of the representative Ti-A100 sample (irradiated with full molten track coverage). Figures 3.2(b) and 3.2(c) illustrate that oxygen enriches in the outermost surface region (< 500 nm) preferentially. Meanwhile, nitrogen penetrates much deeper into the substrate and mainly enriches below the outermost surface region (> 500 nm), which agrees with previous study results [169]. With a careful observation, it is figured out that the TiN region comprises a TiN layer and TiN dendrites embedded in the Ti substrate [199] (clearly revealed in Figs. 3.2(a) and 3.2(c)). Thanks to the EDS mapping results of the cross section, diffusion depths of oxygen and nitrogen were measured. In the present study, it was assumed that the average thickness of the top layer and the average penetration depth of TiN dendrites were taken as the effective diffusion depths of oxygen and nitrogen, respectively. As demonstrated in Figs. 3.2(b) and 3.2(c), the diffusion depths of oxygen and nitrogen for the sample Ti-A100 were determined. Similarly, diffusion results of all the other three samples were also measured.

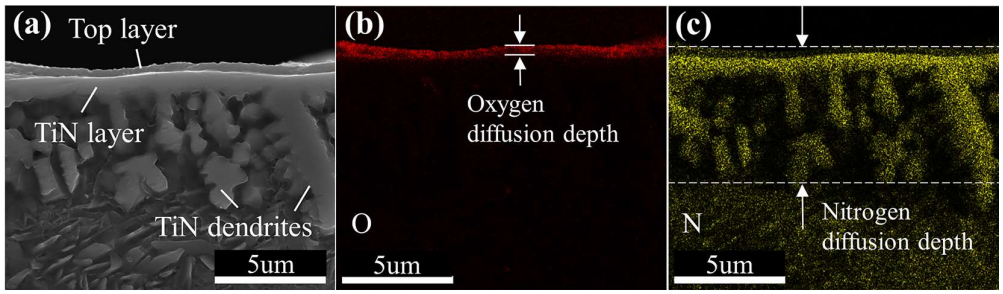

Figure 3.2. Images showing EDS mapping results of the cross section of Ti-A100. (a) shows the cross-section region where the EDS tests was performed, (b) and (c) show the oxygen and nitrogen distribution on the cross section.

Figure 3.3 reveals the microstructures of the cross sections of the Ti-A25, Ti-A100, Ti-A400 and Ti-A1600 samples. Obviously, the cross sections are composed of an outermost surface layer (an oxygen enrichment layer) and a TiN region (TiN layer and TiN dendrites). With the increase of laser scanning speed, the diffusion depths of oxygen and nitrogen declines. Specifically, as the laser scanning speed increases from 25 mm/s to 1600 mm/s, the measured diffusion depth (x) of oxygen declines from 0.79 μm to 0.10 μm. This observation can be explained as follows, a slower scanning speed leads to a longer laser-sample interaction time (longer soaking time at elevated temperature) for oxygen and nitrogen to diffuse into the substrate and react with Ti, resulting in a thicker diffusion depth.

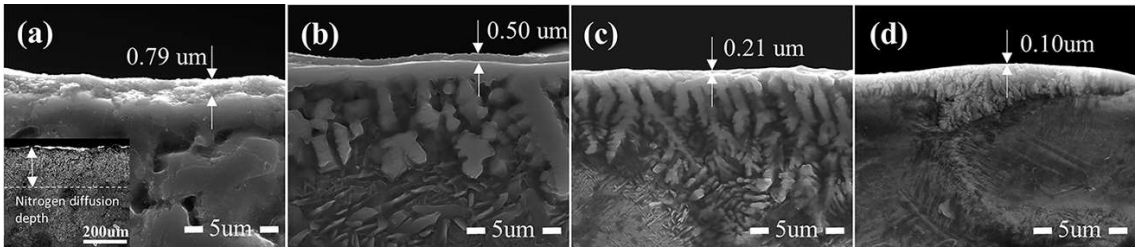

Figure 3.3. (a), (b), (c) and (d) show the SEM images of the cross sections of Ti-A25, Ti-A100, Ti-A400 and Ti-A1600, respectively. The insert image in (a) demonstrates the cross section of Ti-A25 with small magnification.

Table 3.2. The calculated diffusion coefficients of oxygen and nitrogen into Ti under laser irradiation

Element	Sample	Diffusion depth x (μm)	Spot size d (μm)	Scanning speed v (mm/s)	Interaction time t (s)	D (cm^2/s)	Average D (cm^2/s)
O	Ti-A25	0.79 ± 0.09	58	25	2.32×10^{-3}	$(6.73 \pm 1.62) \times 10^{-7}$	$8.00\pm 1.89\times10^{-7}$
	Ti-A100	0.50 ± 0.06		100	5.80×10^{-4}	$(10.78 \pm 2.74)\times10^{-7}$	
	Ti-A400	0.21 ± 0.03		400	1.45×10^{-4}	$(7.60 \pm 2.32)\times10^{-7}$	
	Ti-A1600	0.10 ± 0.01		1600	3.63×10^{-5}	$(6.89 \pm 1.45)\times10^{-7}$	
N	Ti-A25	198.4 ± 4.30	58	25	2.32×10^{-3}	$(4.24 \pm 0.19)\times10^{-2}$	/
	Ti-A100	9.00 ± 0.66		100	5.80×10^{-4}	$(3.49 \pm 0.53)\times10^{-4}$	
	Ti-A400	2.87 ± 0.56		400	1.45×10^{-4}	$(1.42 \pm 0.61)\times10^{-4}$	
	Ti-A1600	1.06 ± 0.30		1600	3.63×10^{-5}	$(7.73 \pm 4.99)\times10^{-5}$	

Based on the results above, diffusion coefficients of oxygen and nitrogen into Ti substrate, named as $D^{O}_{Ti(O,N)}$ and $D^{N}_{Ti(O,N)}$, were calculated, where Ti(O,N) indicates the Ti substrate with already diffused oxygen and nitrogen elements. Laser-sample interaction time (diffusion time) t was determined by $t = d/v$, where d, v are laser spot size and laser scanning speed, respectively. According to the equation [200],

$$D = x^2/(4t) \tag{3-2}$$

where D, t are the average diffusion coefficient and the diffusion time, $D^{N}_{Ti(O,N)}$ and $D^{O}_{Ti(O,N)}$ values were determined from the measured diffusion depths x shown in Table 3.2. With this simple model, $D^{O}_{Ti(O,N)}$ values were found similar for all the tested laser speeds. However, with the decrease of laser scanning speed, $D^{N}_{Ti(O,N)}$ increases significantly. Specifically, when laser scanning speed decreases from 100 mm/s to 25 mm/s, a dramatically increase of $D^{N}_{Ti(O,N)}$ (from 3.49×10^{-4} to 4.24×10^{-2} cm^2/s) is seen. This phenomenon indicates the absorption of nitrogen is more dependent on the laser parameters than that of oxygen, which agrees with the previous discovery [201]. Due to the much increased diffusion depth of nitrogen, $D^{N}_{Ti(O,N)}$ is approximately three orders of magnitude larger than $D^{O}_{Ti(O,N)}$. Clearly, the diffusion mechanism of oxygen and nitrogen in molten Ti is distinguished from each other. Previous studies also reported similar observations [169, 173, 201, 202], where TiO_2 appeared in the outermost

surface over TiN. Nitrogen was also found to have a large solubility in liquid iron while oxygen showed limited solubility, the insertion of oxygen into iron was inhibited at elevated temperatures over melting point [201]. This observation can be applied to explain the case in liquid Ti. Besides, TiN and TiO_2 show remarkably varied formation enthalpies (-338 and -944 kJ/mol, respectively) [202]. The much reduced enthalpy of formation of TiO_2 inhibits the diffusion of oxygen into Ti to a deep region, instead, oxygen tends to react with Ti and form TiO_2 near the outermost surface [201, 202].

3.3.2 Synchrotron X-ray diffraction test to understand the diffusion processes

To better understand the diffusion processes of oxygen and nitrogen into the Ti substrate, *in-situ* SXRD characterization was performed to discover the high-temperature reaction steps between Ti and air.

The location of laser irradiation was fixed and the whole process endured for several secs, and the detailed setup is shown in Fig. 2.1. After obtaining the XRD patterns, the results were radially integrated crystallographic peaks by the software FIT2D. Figure 3.4 shows the analyzed results, which exhibit the detailed information of XRD diffraction angles and intensities as a function of time frame numbers. Considering the sampling rate as 10 Hz, 120 frames indicate 12 secs for the entire data logging process. Laser irradiation was started around 0.7 sec after the initiation of data collecting, and the laser irradiation process endured from time-frames 7 to 77, seven secs in total. Based on the time and the phases generated during the SXRD process, the interactions between Ti and air can be divided into four stages.

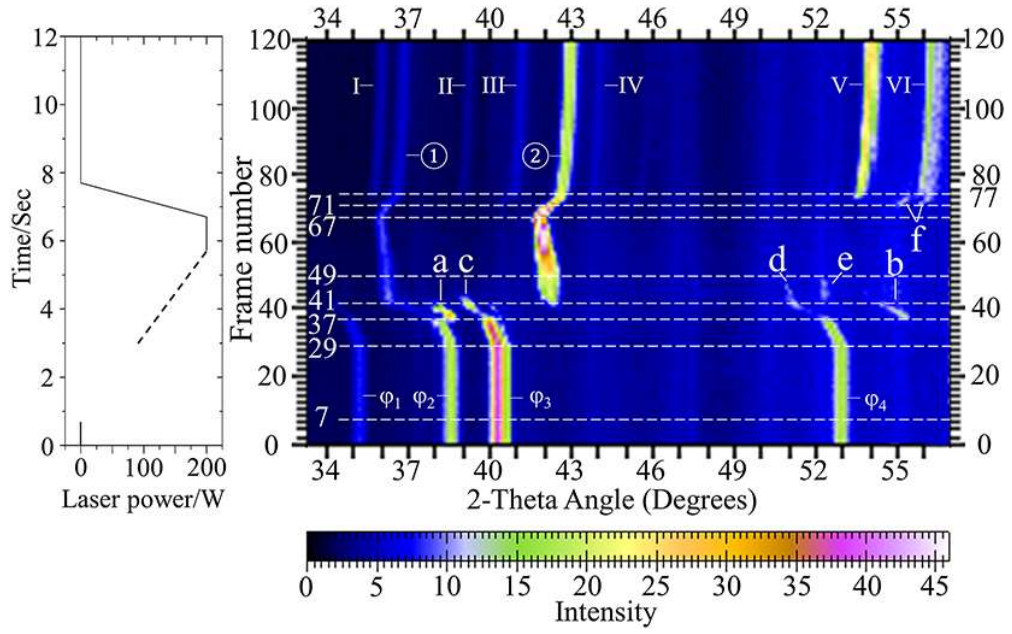

Figure 3.4. Image demonstrating *In-situ* X-ray diffraction information (angles and intensities) as a function of time frames, the image on the left indicates the programmed laser profile. φ_1, φ_2, φ_3, φ_4 indicate the diffraction patterns of αTi(100), αTi(002), αTi(101) and αTi(102), respectively. a, b describe the peaks of βTi. c, d depict the peaks of αTi. e displays the peak of TiN_x. f shows the peaks of the phase TiO_xN_y. ① and ② are diffraction patterns of TiN(111) and TiN(200), respectively. I, II, III, IV, V and VI repreesnt the diffraction peaks of rutile TiO_2 (101), TiO_2(200), TiO_2(111), TiO_2(210), TiO_2(211) and TiO_2(220), respectively.

Stage 1 (y = 0-29) shows diffraction patterns, intensity and angle, at around room temperature, which indicates αTi phase on the tested sample surface. This stage can be further divided into two periods, from time frame 0 to 7 (period 1, before the initiation of laser) and from time frame 7 to 29 (period 2, after the initiation of laser). Obviously, the diffraction patterns remain the same during stage 1. The observation is due to the features of the YLS-2000 IPG fiber laser applied in the present study, which cannot be accurately controlled at a low power level (200 W, below 10% of the maximum power). With a closer observation of the SXRD results shown in Fig. 3.4, it was revealed that the laser irradiation was actually effectively initiated at time-frame 29, and then increased to 200 W at time-frame 57. The dotted line (left image in Fig. 3.4) depicts the programed power increasing rate. According to the observed SXRD results, the Ti sample remained at/near room-temperature before time-frame

29 because of the non-linear irradiation power; moreover, the only phase can be detected is αTi.

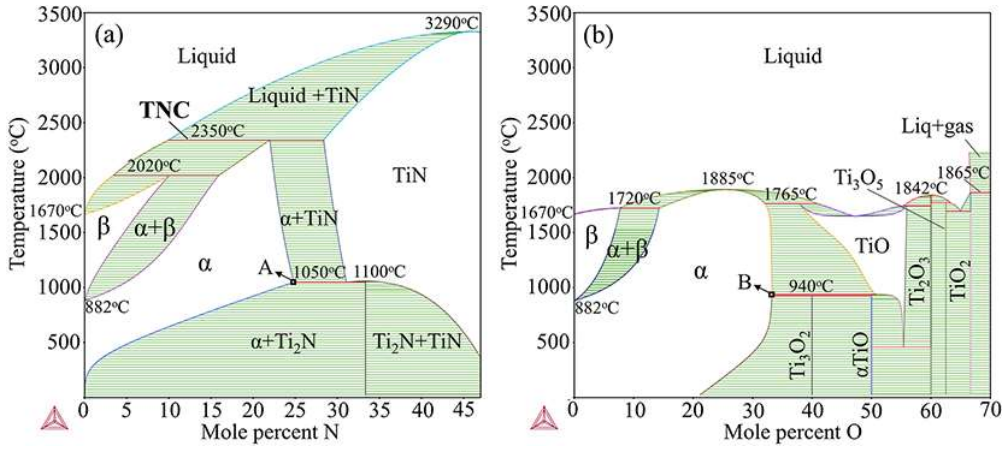

Figure 3.5. Image depicting the phase diagrams calculated using the Thermo-Calc software (a) Ti-N binary phase diagram (b) Ti-O binary phase diagram.

Stage 2 (y = 29-37, 37-41 and 41-49) shows the surface temperature rising of the Ti sample. Diffraction angle of αTi phase keeps decreasing from time frame 29 to 37, ascribed to the expansion of sample originated from the increasing temperature. Clear change of diffraction angles and intensities are observed at time frame 37, which is due to the phase transformation from αTi (HCP) to βTi (BCC). Ti-O and Ti-N binary phase diagrams were calculated using Thermo-Calc software (TCBIN database) to assist the understanding to the oxidation and nitridation processes, which are shown in Fig. 3.5. According to the phase diagrams, at atmospheric pressure, the HCP to BCC allotropic phase transformation temperature for pure Ti is 822 ℃. Four distinct diffraction peaks (namely *a*, *b*, *c* and *d*) are observed within time frames 37 to 41. Peaks *a* and *b* reflect the appearance of a βTi structural phase, while peaks *c* and *d* reveal the αTi phase with expanded lattice. Note that the diffraction intensity of βTi is gradually attenuated over the time-frames 37-41, while the diffraction intensity of αTi is gradually enhanced. When the pure Ti is heated up, it undergoes the following phase change αTi → βTi → Liquid. Thanks to the Ti-N and Ti-O binary phase diagrams in Fig. 3.5, the observed unique coexistence of αTi and βTi can be explained.

Antończak [169] discovered that both αTi and βTi would absorb large quantities of interstitial oxygen and nitrogen atoms above 600 °C. Specifically, αTi has the capability of dissolving 33 at% (14 wt%) of oxygen and 23 at% (8 wt%) of nitrogen, which is also indicated on the Ti-N and Ti-O phase diagrams (marked by A and B). Nitrogen and oxygen plasma was also reported induced during laser heating [155], which would accelerate the intake of nitrogen and oxygen into the Ti sample surface. Based on our *in-situ* SXRD results, Ti first transformed from αTi to βTi, then changed from βTi to αTi+βTi two-phase state due to the rapid concurrent intake of nitrogen or oxygen. When reaching time frame 41, βTi vanishes, which is caused by the conversion to αTi ascribed to the further intake of nitrogen or oxygen. Meanwhile, TiN signal starts to appear while the diffraction patterns of αTi can still be seen. The coexistence of αTi and TiN phases can be interpreted as follows. Firstly, the transient nitridation curve (TNC) marked in Fig. 3.5(a) is reached (with a temperature of 2350 °C), which indicates the coexistence of TiN, αTi and Liquid phase. Secondly, due to the Gaussian distribution, energy distribution of the laser spot is not uniform, causing the uneven temperature distribution of the area illuminated by the X-ray. Therefore, due to the higher energy density, the center of the laser irradiated area shows a higher temperature, wherein exist the Liquid+TiN two phases. Thirdly, due to the complex composition and temperature distribution on the laser illuminated area, some regions may go directly into the αTi+TiN two-phase region. Within the time-frames 41-49, diffraction peak (e) of TiN_x appears (a sub-stoichiometric phase), which, however, becomes almost invisible at around time-frame 49 as it further reacts to completion of TiN. TiN becomes the dominate phase by time frame 49. It is worth noting that no diffraction pattern of titanium oxides can be detected before time-frame 49, strongly indicating that this component exists in liquid state.

Stage 3 (y = 49-67) demonstrates the diffraction peaks of TiN. During this stage, temperature of the laser illuminated area keeps increasing due to the further shift of the

diffraction patterns of TiN to the smaller angles. Besides, more TiN is generated over this stage, which is reflected by the further enhancement of diffraction intensities of TiN. The maximum temperature is reached at time-frame 67, for the minimum value of diffraction angle of TiN phase is obtained. Obviously, with the laser profile in the present study, the maximum temperature on the sample surface does not exceed the melting point of TiN, which would be indicated by the intensity drop off and a strongly increased peak width.

Stage 4 (y = 67-71, 71-77 and 77-80) depicts the cooling process. Evidently, the diffraction peaks of TiN continuously shift to larger angle side over the time-frames 67-71, indicating the thermal contraction of TiN phase due to the declining temperature. Only distinct diffraction peaks that correspond to TiN are identified during this period. At time-frame 71, two new diffraction peaks appear with difraction angles around 55° and 56° (indicated with "f"). According to previous study [203], these diffraction peaks correspond to TiO_xN_y structure, originated from the early reaction between oxygen and TiN. This structure is generated when oxygen atoms diffuse into the TiN lattice and replace nitrogen. The intensity of TiN is gradually weakened from time frames 71 to 77, while the diffraction peaks of TiO_xN_y disappear and rutile TiO_2 peaks appear at time-frame 77. This observation indicates that TiO_xN_y is a transitional, metastable phase.TiN is a thermodynamically stable phase, however, when it is exposed to air or O_2, reaction occurs: $TiN + O_2 \rightarrow TiO_2 + ½N_2$ [204-207]. And the standard Gibbs energy difference ($\Delta G°$) of this process is -581.6 KJ/mol, indicating that the process is thermodynamically favorable.

According to the diffraction patterns from time-frames 67 to 77, the phase transformations presumably follow $TiN \rightarrow TiO_xN_y \rightarrow TiO_2$, and this is a diffusion-limited process by the atomic oxygen into the TiN/Ti substrate. Therefore, for obtaining a thick TiO_2 layer, sufficient diffusion time for atomic oxygen is essential. It is worth noting that TiO_2 may indeed exist in liquid state since its melting point (1843 °C), is significantly lower than that of

TiN (2930 °C). No diffraction pattern would be observed from the liquid state TiO_2 (LTO) in the SXRD test. Therefore, the TiO_2 phase observed at time-frame 77 may stem from two parts, (i) the reaction between TiN and O_2, (ii) the solidification from LTO. From time-frame 77 to 120, the diffraction intensity of TiN keeps attenuates slightly while the diffraction intensity of TiO_2, to some extent, increases. Diffraction peaks continue to shift to larger angles, however, with clearly smaller angle varying rate relative to the period from time-frame 67 to 77, revealing a significantly smaller cooling rate.

According to the SXRD results, the phase change steps between Ti and air during laser irradiation are as follows, $\alpha Ti \rightarrow \beta Ti \rightarrow \alpha Ti+\beta Ti \rightarrow \alpha Ti+TiN+TiN_x$ (+LTO)$\rightarrow$ liquid+TiN (+LTO)$\rightarrow$ $TiN+TiO_xN_y$ (+LTO)$\rightarrow$ TiO_2+TiN.

3.3.3 Compositions and microstructures of the sample after the SXRD test and diffusion coefficient calculation

Figure 3.6 demonstrates the microstructure and composition testing results of the laser processed surface after the SXRD test. With a closer observation, the cross section is composed of two regions, the solid layer (around 240 μm thick) and the heat affected layer. The obvious separation of the two layers must be resulted from the induced stress of the cold pressed ~40 μm Ti powder during the laser processing. Interestingly, the top half of the re-solidified layer contains clearly more pores than the bottom half (Fig. 3.6(e)). Large amounts of gaps between powders exist in the Ti disk for it is originally loosely packed. Moreover, as explained above, oxygen might react with the generated TiN on the surface and consequently N_2 is released. During the SXRD test process, the cooling process lasts approximately 1 sec (time frame 67-77). Therefore, the average cooling rate would be over 2.0×10^3 K/s considering a peak temperature on the sample surface is over 2000 ℃. Owing to the fast cooling rate, the generated N_2 gas would be trapped in the sample surface region. The solid layer can then be correspondingly divided into two regions, the porous solid layer closer to the surface and the

underlying solid layer, which show almost identical thickness (120 μm). Figures 3.6 (f)-(h) illustrate the EDS mapping analysis results of the area indicated in Fig. 3.6 (e), which reveal that oxygen mainly enriches in the porous solid layer, especially on the outermost surface layer, while nitrogen has higher content on the bottom of the porous solid layer. Oxygen can hardly be seen in the bottom solid layer, while nitrogen signal can still be identified, though with a relatively weaker intensity. EDS testing results show that Ti element exists everywhere in the cross section, with the signal intensity in the bottom solid layer stronger than that in the porous solid layer. The distinct enrichment of oxygen in the outermost surface may be attributed to the following two reasons, first the enrichment of LTO at the solidification front and second the reaction between TiN and O_2. Due to the limited diffusion time, only limited amount of nitrogen and oxygen is absorbed by the sample, causing limited diffusion depth of the two elements. As discussed in section 3.1.2, nitrogen diffuses faster than oxygen into Ti substrate. The above discussions explain the reasons why the bottom solid layer contains limited oxygen, reduced nitrogen content, and clearly fewer pores.

According to the SXRD testing results, the outermost surface layer should be composed of a mixture of TiO_2 and TiN, or TiN beneath TiO_2. Based on Figs. 3.6 (i)-(l), with larger magnification, it is obvious that the outermost surface layer mainly comprises titanium-oxides species with negligible nitrogen signal. Pores with the size of several hundred nanometers are observed in Fig. 3.6 (b). Both micro-sized and nano-sized pores exist from the observation of Figures 3.6(c) and 3.6(d), which could, although speculative, be caused by both the release of the reaction product N_2 and the low-packing-density powder bed. Nano-sized pores were also observed by the studies of Chen [206] and Pérez del Pino [177], which were reported most likely caused by the reaction between TiN and O_2.

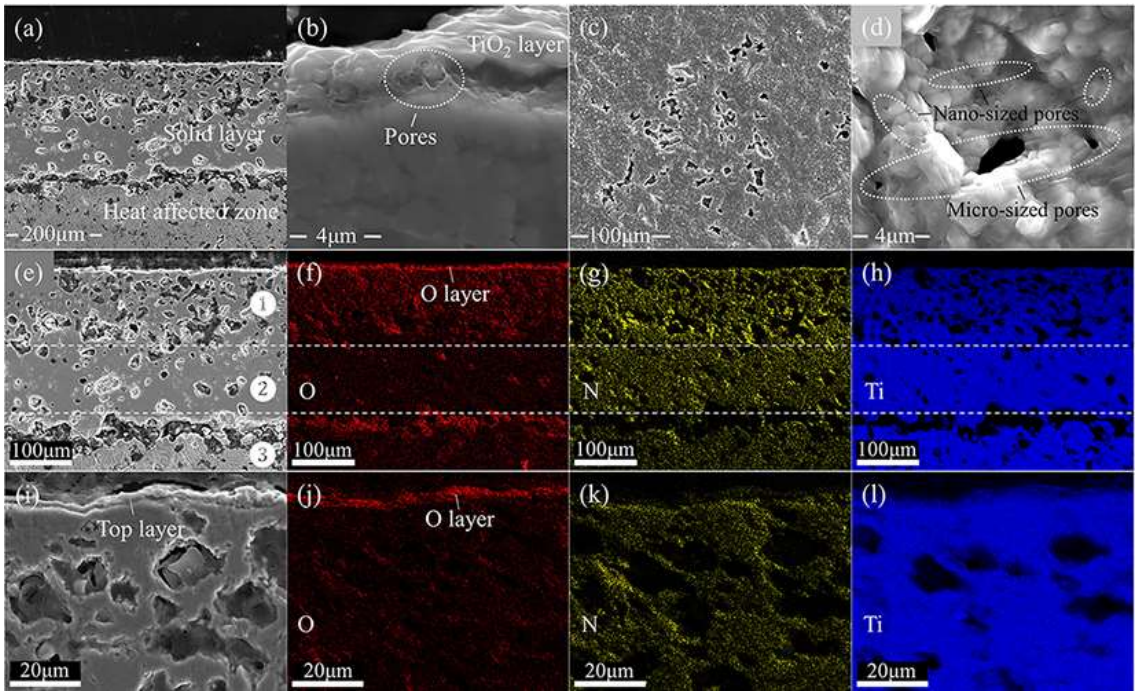

Figure 3.6. Images showing the microstructures and composition distribution of the laser processed pure Ti surface under air atmosphere after SXRD testing. (a), (b) illustrate the cross-section microstructures with differing magnifications. (c), (d) demonstrate the top surface microstructures of the laser processed area. (f)-(h) depict the EDS mapping composition testing results, representing oxygen (O), nitrogen (N) and Ti respectively, of the cross section indicated by (e). (j)-(l) again show the EDS mapping results of the sample cross section with larger magnification of the area indicated by (i).

The $D^{N}_{Ti(O,N)}$ and $D^{O}_{Ti(O,N)}$ values can be estimated with the observed results after SXRD testing. The thickness of the oxygen-enriched outermost surface layer is around 2.5 μm (Fig. 3.6 (j)), which is in line with previous study [159]. However, at the bottom of the porous solid layer, oxygen signal is still seen, indicating a diffusion depth of around 120 μm. The outermost oxygen-enriched layer resulted from the oxidation of TiN, therefore, the diffusion depth of oxygen in TiN during the laser irradiation process is approximately 2.5 μm. Nitrogen signal can be detected in the bottom solid layer, therefore, the diffusion thickness of nitrogen is estimated to be around 240 μm. According to the following formula (3-2), $D^{O}_{Ti(O,N)}$, $D^{N}_{Ti(O,N)}$ and D^{O}_{TiN} (diffusion coefficient of O in TiN) values can be estimated. Besides, the relationship between the absolute temperature (T) and diffusion coefficient (D) is shown as

$$D = D_0 \exp(-E/RT) \tag{3-3}$$

Where E, R represent the activation energy and gas constant, respectively. Clearly, the higher temperature, the larger the diffusion coefficient. Besides, high-temperature diffusion plays the dominant role in the oxygen and nitrogen absorption, when taking the fast heating and cooling rate of the laser processing into consideration. Referring to Fig. 3.4, the high temperature period lasts 3.6 seconds in total (from time frame 41 to 77). TiN starts to generate at time frame 41, while TiO_2 appears at time frame 77. Because Ti shows a stronger affinity for oxygen than nitrogen [208], the temperature at time frame 41 must be higher than the melting point of titanium oxide (or TiO_2). Therefore, the temperature from time frame 41 to 77 is estimated above the melting point of TiO_2 (1843 ℃) but lower than the melting point of TiN (2930 ℃). Accordingly, the estimated results are displayed in Table 3.3.

$D^{O}_{Ti(O,N)}$ is approximately 1.0×10^{-5} cm^2/s while $D^{N}_{Ti(O,N)}$ is around 4.0×10^{-5} cm^2/s, which are about four orders of magnitude larger than that of D^{N}_{TiN} (around 4.34×10^{-9} cm^2/s).

Table 3.3. The estimated diffusion coefficients of oxygen and nitrogen on synchrotron testing

Diffusion type	Diffusion depth (μm)	Temperature range (°C)	t (s)	D (cm^2/s)
O in TiN	2.5 ± 0.6	1843-2930	3.6	$(4.34 \pm 2.33) \times 10^{-9}$
O in Ti(O,N)	120 ± 9.9	1843-2930	3.6	$(1.0 \pm 0.17) \times 10^{-5}$
N in Ti(O,N)	240 ± 20.3	1843-2930	3.6	$(4.0 \pm 0.71) \times 10^{-5}$

3.3.4 Discussion of Diffusion coefficients of oxygen and nitrogen in Ti

Through literature review, it was discovered that several studies investigated the diffusion coefficients of oxygen and nitrogen in Ti, titanium oxides, and titanium nitrides, i.e. diffusion coefficients of oxygen in αTi [186, 188], $D^{O}_{\alpha Ti}$, oxygen in βTi [189-191], $D^{O}_{\beta T}$, oxygen in TiO_2 [192], $D^{O}_{Ti_2}$, nitrogen in αTi [193, 194], $D^{N}_{\alpha Ti}$, nitrogen in βTi [195], $D^{N}_{\beta Ti}$, nitrogen in TiN [196], D^{N}_{TiN}, and nitrogen in Ti_2N [195], $D^{N}_{Ti_2N}$. However, these studies only focused on the diffusion behavior below 1700 ℃. Diffusion coefficients estimated in the present study are listed in Tables 3.2 and 3.3 far over the melting point of Ti, which can be the guidance for the design of laser-based surface modifications or additive manufacturing of Ti

alloys. Apparently, over the high temperature range, $D^{N}_{Ti(O,N)}$ is much higher than $D^{O}_{Ti(O,N)}$, which is due to the much higher solubility of nitrogen atoms in Ti at elevated temperatures, and the much larger enthalpy of formation of TiN (negative value, smaller absolute value).

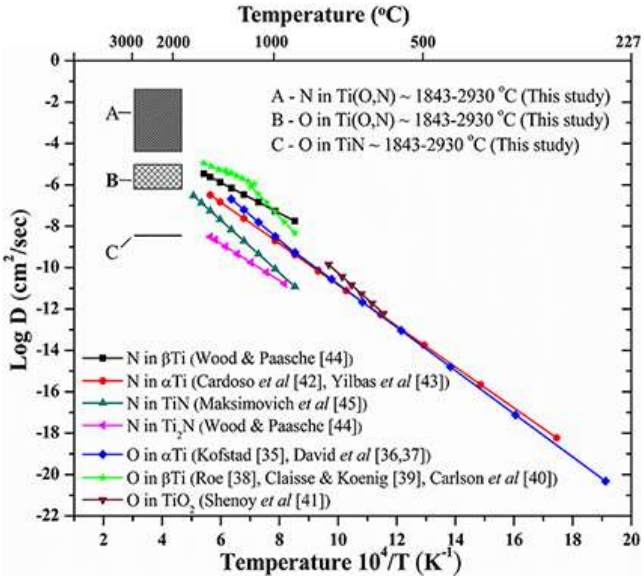

Figure 3.7. Diffusion coefficients of O in αTi, βTi and TiO_2, and the diffusion coefficients of N in αTi, βTi, TiN and Ti_2N (literature), together with the experimentally estimated diffusion coefficients of O and N into laser irradiated Ti in air (this study).

The diffusion coefficients generally increase monotonically with the increase of temperature according to literature survey (Fig. 3.7), and the linear relation between the inverse absolute temperature and the logarithmic function of diffusion coefficients follows the Arrhenius equation (3-3). Notably, the experimentally determined $D^{O}_{Ti(O,N)}$ and $D^{N}_{Ti(O,N)}$ (B and A range in Fig. 3.7, respectively) of this study are located on the extrapolated lines of the existing literature data, showing a strong alignment between the data obtained in this study and the previous results. The estimated $D^{O}_{Ti(O,N)}$ in Table 3.2 (8.00×10^{-7} cm^2/s) is clearly smaller than that acquired under the SXRD condition (1.0×10^{-5} cm^2/s), which is possibly resulted from the variance of localized laser energy density. For the tests described in Table 3.2, the laser energy density is significantly higher than that of the SXRD testing ascribed to the defocus; this observation is also reflected by the greatly improved rate of heating to melting/evaporation.

Therefore, a localized oxygen deprived zone caused by the evaporation of Ti vapor may generate and keeps the available oxygen from diffusing into the Ti substrate. Although the estimated $D^{O}_{Ti(O,N)}$ is from 8.00×10^{-7} to 1.0×10^{-5} cm^2/s (Fig. 3.7), the true value is more likely close to 1.0×10^{-5} cm^2/s. From the above discussion, $D^{N}_{Ti(O,N)}$ is known to be relying on laser energy density, the higher laser energy density, the larger $D^{N}_{Ti(O,N)}$ will be. This depicts the reason why the estimated $D^{N}_{Ti(O,N)}$ in Table 3.2 shows larger values than that under the SXRD condition. And due to the distinct laser energy density variance, the estimated $D^{N}_{Ti(O,N)}$ varies dramatically from 4.0×10^{-5} to 4.24×10^{-2} cm^2/s.

3.4. Conclusions

In this chapter, the reactions between commercially pure Ti and ambient air are studied under typical laser additive manufacturing conditions. The microstructures and composition distributions of the cross sections after laser irradiation of the pure Ti samples are investigated. A synchrotron X-ray diffraction test is carried out to evaluate the dynamic reactions between pure Ti and ambient air under laser irradiation, which is beneficial for better elucidating the diffusion of oxygen and nitrogen into Ti throughout a large temperature range. Thanks to the material characterizations, high-temperature diffusion coefficients of nitrogen and oxygen into Ti under ambient air atmosphere are estimated. And the following conclusions are obtained.

(1) The phase transformation steps revealed by the synchrotron X-ray diffraction test under laser irradiation process are found to be αTi→ βTi→ αTi+βTi→ αTi+TiN+TiN_x (+LTO)→ liquid+TiN (+LTO)→ TiN+TiO_xN_y (+LTO)→ TiO_2+TiN. Titanium nitrides is observed during the melting process, while TiO_2 only appears during the cooling stage, originating from the reaction between TiN and O_2 or the solidification of the pre-existing liquid titanium oxides.

(2) After laser irradiation under an atmospheric environment, oxygen is discovered to only enrich in the outermost surface, while nitrogen mainly exists below the oxygen rich layer.

(3) For the first time, the diffusion coefficients (especially at elevated temperature) of nitrogen and oxygen into Ti samples in air under laser irradiation are calculated. And the diffusion coefficients of nitrogen and oxygen into Ti are estimated to be 4.00×10^{-5} - 4.24×10^{-2} cm^2/s and 8.00×10^{-7}-1.00×10^{-5} cm^2/s, respectively, from 1843 ℃ to 2930 ℃. Meanwhile, the diffusion coefficient of oxygen in TiN is estimated to be 4.34×10^{-9} cm^2/s. By adjusting laser parameters, TiO_2/TiN layers with controllable thickness can be acquired.

Chapter 4. Laser Nitridation of Titanium Surfaces for Biomedical Applications

4.1. Introduction

Due to the excellent properties, i.e. light weight and high strength to weight ratio, titanium and its alloys have been extensively studied [209-212]. Surface nitridation is usually performed to further improve the biocompatibility and corrosion resistance of titanium alloy parts. The generated titanium nitride (TiN) coating can both significantly enhance the hardness of surface [213-215], and improve chemical stability, corrosion resistance, and biocompatibility [216-218].

Laser surface nitridation of titanium parts has been extensively studied [75, 147, 149, 183, 219-224] for its obvious advantages, for example the capability to generate TiN layer with substantial thickness (> 1 μm), simplicity, and the negligible influence on the substrate. Dahotre et al. [149] performed laser nitridation on Ti-6Al-4V alloy in pure N_2 atmosphere, where three different laser energy densities (1.70, 1.89, and 2.12×10^6 J/m^2) were investigated and TiN dendrite layers with thickness of 9.5, 11.3, and 13.8 μm, respectively, were obtained. And it was pointed out that corrosion resistance, osseo-integration, and tribological properties were improved with the laser energy densities of 1.89 and 2.12×10^6 J/m^2. The effect of laser surface nitridation on the bio-performance of Ti-10Mo alloy was also investigated (scanning speed 100 mm/s, laser power 75 W, hatch spacing 50 μm, spot size 104 μm, pure N_2 environment). With a rough 8 μm thick TiN-dendrite layer, the bio-compatibility and corrosion resistance were greatly improved [225]. Laser surface nitridation was also conducted on

This chapter was previously published as Congyuan Zeng, Hao Wen, Ali Hemmasian Ettefagh, Bin Zhang, Juan Gao, Ali Haghshenas, Jonathan R. Raush, S.M. Guo. "Laser nitriding of titanium surfaces for biomedical applications", Surface and Coatings Technology, 2020. Reprinted by permission of Elsevier.

commercially pure (CP) titanium with pulsed laser and pure N_2 environment, and it was reported that corrosion resistance was significantly improved in Hank's solution [226]. Chan et al. [227] performed laser processing on Grade 2 CP titanium under a shielding high-purity N_2 (5 bar) with continuous wave (CW) fiber laser, and bacterial adhesion was dramatically reduced and the surface showed bactericidal effect.

In addition to the pure N_2 environment, laser nitridation process was also conducted in dilute N_2 atmosphere (balance of Ar). Sathish et al. [147] investigated laser surface nitridation on titanium under 0.2 bar N_2 atmosphere (Nd:YAG pulsed laser), and no clear TiN signal was seen with X-ray diffraction (XRD) characterization. The effects of N_2 contents, namely 0, 2.5, 50 and 100 vol.% with a laser power ~1.85 kW, on the generation of titanium nitrides on titanium surfaces were studied [183], and it was found that even with a N_2 content of 2.5 vol.%, the surface hardness was enhanced (from ~200 HV to ~400 HV). The influence of varying N_2 contents (80 and 100 vol.%) was also investigated by Xin et al. [224], and the titanium-nitride coating could remarkably enhance the wear property. Titanium surfaces partially covered by TiN (coexistence of TiN and Ti on the outermost surface) may be generated by laser nitridation in a dilute N_2 environment, which should possess unique corrosion resistance and biocompatibility characteristics. Ti6Al4V/TiN composite layers (with 0, 10, 15, 20 and 40 wt.% TiN) were deposited on pure titanium surface with the thickness around 3 mm using Laser Engineered Net Shaping (LENS^{TM}) [228]. And these composite coatings were discovered non-toxic and exhibited superior cell-material interactions compared to the Ti6Al4V counterparts. Similar study was also carried out by Zhou et al. [229], who prepared a Ti-5 wt.% TiN composite layer on CP titanium surface with selective laser melting method, which improved the corrosion resistance of CP titanium in 0.5M HCl solution. Besides, the generated surface layer also made the corrosion mechanism change from pitting to uniform corrosion.

Unfortunately, in spite of the study above, no systematic work has been published to look into the effect of nitrogen contents on the phase distribution and composition of titanium surfaces, and the influences of the acquired surfaces on corrosion property and bio-compatibility. To fill the knowledge gap, this chapter evaluated the effects of laser nitridation conditions on the performance of titanium, with the goal of discovering the critical surface characteristics for improved corrosion and bio- properties. By controlling the N_2 contents (from 0 to 100 vol.%) and varying laser scanning speeds, surface layers with varying TiN amount (from a negligible level to a thick layer of tens of microns in thickness) were generated and evaluated in this chapter.

4.2. Materials and methods

4.2.1 Laser nitridation of titanium surfaces

CP titanium pieces (10×10×3 mm^3, Grade 2, 99.2 wt.% purity) were studied. Prior to the laser processing, to remove surface contaminants, the surfaces of the samples were ground with SiC papers (320 and 600 grit, in sequential). After that, the samples were ultrasonically rinsed in acetone, ethanol, and deionized water successively (20 min each). Mixtures of pure Ar and N_2 (ultrahigh purity 5.0 grade, Airgas) were used as the laser processing atmosphere. To perform different laser processing conditions on the titanium pieces, a custom laser processing system (200 W, IPG ytterbium fiber laser, wavelength 1064 nm) was used. A Cambridge Technology ProSeries II scan head was used to control the scanning patterns to fulfill the entire surface processing. Three laser scanning speeds (100, 400, and 1600 mm/s) were investigated under pure N_2 atmosphere with a fix spot size of 207 μm and a fixed laser power of 175 W. In the remainder of this chapter, the samples are denoted as Ti-N100, Ti-N400 and Ti-N1600, respectively, for easy distinguishing. To figure out the influence of diluted N_2 on the formation of titanium nitrides (laser power 175 W, spot size 207 μm, scanning speed 400 mm/s), five different N_2 contents (100, 75, 50, 20 and 0 vol.%, balance of Ar) were

investigated, which are, similarly, named as Ti-N400, Ti-N75%, Ti-N50%, Ti-N20% and Ti-N0%, respectively. To ensure the credibility and repeatability of the tests, three samples for each laser processing condition were prepared. And the images for all the samples are exhibited in Fig. 4.1. The processing parameters for the samples are listed in Table 4.1.

Figure 4.1. Image of the as-processed samples, where 1, 2, 3, 4, 5, 6, 7 indicate samples Ti-N100, Ti-N400, Ti-N1600, Ti-N75%, Ti-N50%, Ti-N20%, and Ti-N0%, respectively.

Table 4.1. Laser processing parameters performed on sample surfaces

Sample	Parameters			
	Scanning speed (mm/s)	Hatch Spacing (μm)	N_2 content (vol. %)	Ar content (vol. %)
Ti-N100	100	120	100	0
Ti-N400	400	64	100	0
Ti-N1600	1600	35	100	0
Ti-N75%	400	64	75	25
Ti-N50%	400	64	50	50
Ti-N20%	400	64	20	80
Ti-N0%	400	64	0	100

4.2.2 Laser nitrided layer characterizations

SEM, EDS and XRD: Phase structures of the laser processed surfaces were evaluated with X-ray diffraction (XRD) from 20° to 80° with a scanning step of 0.026°. Microstructures were

characterized using the Scanning Electron Microscopy (SEM). The cell morphology and as-processed titanium surfaces were investigated using SEM with accelerating voltages of 20 KV and 5 KV, respectively. For the microstructure characterization of the cross sections of the laser processed samples, the samples were cut vertical to the laser scanning direction. Afterwards, the surfaces were ground with SiC papers (320, 600, 800, 1000 and 1200 grit, in sequential), and then polished with polycrystalline diamond suspension (6 μm, 3 μm, 1 μm, successively), followed by a final polishing with 50 nm silica suspension for 12 hours on a Vibratory Polisher (Pace Technologies GIGA 0900). Finally, the target surfaces were etched with the Kroll's Reagent purchased from PACE Technologies for 15 s, and cleaned with deionized water and dried in air. Energy dispersive spectroscopy (EDS) mapping test was carried out on the surfaces both before and after corrosion tests, revealing composition (especially oxygen) distribution on the surfaces.

Surface roughness test: Surface roughness test of the as-processed surfaces was carried out with Bruker GTK-17 optical profilometer. For assuring the credibility and repeatability of the surface roughness results, three samples of the same type were characterized.

Coating layer hardness test: Nanoindentation hardness test was performed on the cross sections of the laser irradiated Ti samples. Before hardness testing, the laser irradiated samples were cut, ground, and polished with the same procedure mentioned above. The hardness tests were performed with a Nanoindenter XP system (MTS Systems Corp., Knoxville, TN), with a maximum force of 100 mN and a force rate of 1 mN/sec in a force-controlled mode. Hardness was evaluated at three differing regions, and at each region, 15 testing points were lined in a row (with an interval of 15 um) vertically towards the substrate with the first testing point located around 5 μm below the laser processed surface.

4.2.3 Corrosion property test

A 3-electrode standard corrosion cell was applied for the testing. A platinum wire, a saturated calomel electrode (SCE), and a sample worked as the counter electrode, reference electrode, and working electrode, respectively. The electrochemical test was performed in simulated body fluid (SBF) with a corrosion test instrument (CHI-604C). SBF solution was applied for mimicking human body environment, and the following regents were used to prepare SBF solution with 1 liter, 0.350 g $NaHCO_3$, 0.224 g KCl, 7.996 g NaCl, 0.228 g $K_2HPO_4 \cdot 3H_2O$, 0.278 g $CaCl_2$, 0.305 g $MgCl_2 \cdot 6H_2O$, 6.057 g $(CH_2OH)_3CNH_2$, 0.071 g Na_2SO_4 and 40 mL 1M-HCl. The samples were firstly connected firmly with conductive wires. Then the samples were sealed with the SamplKwick powder and liquid mixture (volume ratio of 2:1) except a portion of the laser irradiated area (with exposed area of 0.9 cm^2). Prior to the tests, the samples were immersed in the SBF solution for 1 h. With a scan rate of 1.67 mV/s, Tafel curves were acquired from -1.0 V_{SCE} to 1.0 V_{SCE}. For each set of laser processing condition, three samples were characterized to assure the reproducibility and credibility of the tests.

4.2.4 Bio-compatibility examination

Mouse MLO-Y4 cells were applied for the cell response tests on the sample surfaces (original seeded density of 2×10^4 cells/cm^2). Prior to seeding cells, the samples were ultrasonically cleaned in acetone, ethanol, and deionized water for 5 min successively, followed by exposure to ultraviolet (UV) radiation overnight. After that, the samples were placed in a plate (six well) for examination. Each well placed three samples with the same processing condition and all the samples were immersed in alpha minimum essential medium (α-MEM), containing 5 % Calf Serum, 5 % Fetal Bovine Serum and 1% penicillin/streptomycin antibiotics. The samples were incubated in an incubator (37 °C, 5 % CO_2 balanced air) for 24 hours. Afterwards, 8 drops of NucBlue® Live reagent (Hoechst 33342) and propidium iodide were added to each well and incubated for 30 minutes. The nuclei of all

the cells were stained with NucBlue® Live reagent, which can be detected using a standard DAPI (4′,6-diamidino-2-phenylindole) filter, which is a prevailing nuclear and chromosome counterstain and emits blue fluorescence upon binding to AT regions of DNA. The nuclei of apoptotic cells were stained with propidium iodide and is visible using a standard red fluorescent protein (RFP) filter. Then the cultured cells were fixed with 3% glutaraldehyde and subsequently dehydrated using a series of ethanol with gradient concentrations, which were 25%, 50%, 75%, 95%, and 100%. The viable/apoptotic cells were observed by a fluorescent microscopy (Zeiss SteREO Lumar) with 80× magnification. The cell morphology was observed with SEM, and the numbers were determined with IMAGEJ software (NIH, Bethesda, MD) and the data were analyzed by one-way analysis of variance method. The detailed experiment procedures can be found elsewhere [37].

4.3. Results and discussions

4.3.1 Compositions, layer thickness and surface roughness of the laser nitrided surfaces

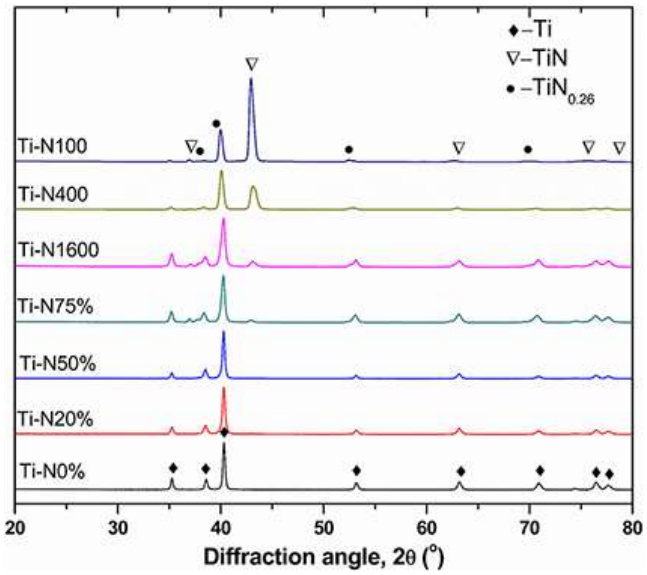

Figure 4.2. XRD test results indicating the phase structures on the laser irradiated sample surfaces.

To better understand the corrosion resistance and biocompatibility performance of the processed surfaces, coating compositions and layer thicknesses were evaluated. Figure 4.2

illustrates the phase structure test results of the sample surfaces. Clearly, the surfaces are made of αTi, TiN and $TiN_{0.26}$. Notably, peak intensities of titanium nitrides (i.e., ~43.0 ° for TiN and ~37.8 ° for $TiN_{0.26}$) are greatly weakened as N_2 content decreases or laser scanning speed increases. Moreover, the only clear diffraction peaks can be detected belong to αTi when N_2 content is below 50 %, demonstrating the negligible amount of titanium nitrides, which is in line with previous studies [147, 183]. According to the precious XPS analysis [230], the nitrogen absorption in the outermost surfaces for Ti-N400, Ti-N75%, Ti-N50%, Ti-N20% and Ti-N0% are 32.45, 25.00, 5.54, 4.53 and 1.38 at.%, respectively. Apparently, the nitrogen intake drops greatly as the N_2 content declines, which agrees with the XRD testing results.

Figure 4.3 shows the cross section microstructures of the samples after etching. The melt pool profiles are clear, by observation of the distribution of titanium nitrides, for the samples Ti-N100, Ti-N400 and Ti-1600N, and the melt pool depths are approximately 66 μm, 26 μm and 12 μm, respectively, which illustrates that melt pool depth decreases as laser scanning speed increases. However, for the dilute N_2 cases, insufficient nitrogen is absorbed by titanium, resulting in negligible thickness of titanium nitride layer (Figs. 4.3 (d), (e), (f) and (g)). It was reported that the formation of titanium nitride improves the laser energy absorption by the substrate [183], consequently increasing the sizes of melt pools of the samples irradiated under pure N_2 atmosphere. As shown in Fig. 4.3 (a), dense titanium nitrides are detected on the cross section of Ti-N100, while according to Figs. 4.3 (b) and (c), titanium nitrides distribute non-uniformly on the cross section of Ti-N400 and Ti-N1600. Most likely, the non-uniform distribution of titanium nitrides originates from the convection induced by Marangoni force [231]. In comparison with Ti-N100, the faster laser scanning speeds (i.e. Ti-N400 and Ti-N1600 cases) cause greatly reduced laser-sample interaction time, which is insufficient for the newly generated titanium nitrides to distribute uniformly throughout the melt pool by the convection flow. Figs. 4.3 (a), (b) and (c) demonstrates thick, dense and columnar TiN

dendrites near the surface region of Ti-N100, while thinner, uneven-distributed, and smaller-sized TiN dendrites in the surface regions of Ti-N400 and Ti-N1600. It is worth noting that a thin layer of titanium nitride is observed in the outermost surface of Ti-N75% (Fig. 4.3 (d)), which should be the microstructures of $TiN_{0.26}$. Similar microstructures were also reported by Dai et al. [232]. No obvious TiN dendrites are seen on Ti-N75% due to inadequate N_2 content for the generation of TiN. Meanwhile, no features of titanium nitrides can be observed on the top surfaces of Ti-N50%, Ti-N20% and Ti-N0% (shown as the inserted images in Figs. 4.3 (e), (f) and (g)), indicating negligible titanium nitrides on those surfaces. The observation of microstructures on the cross sections above agree with the XRD testing results in Fig. 4.2.

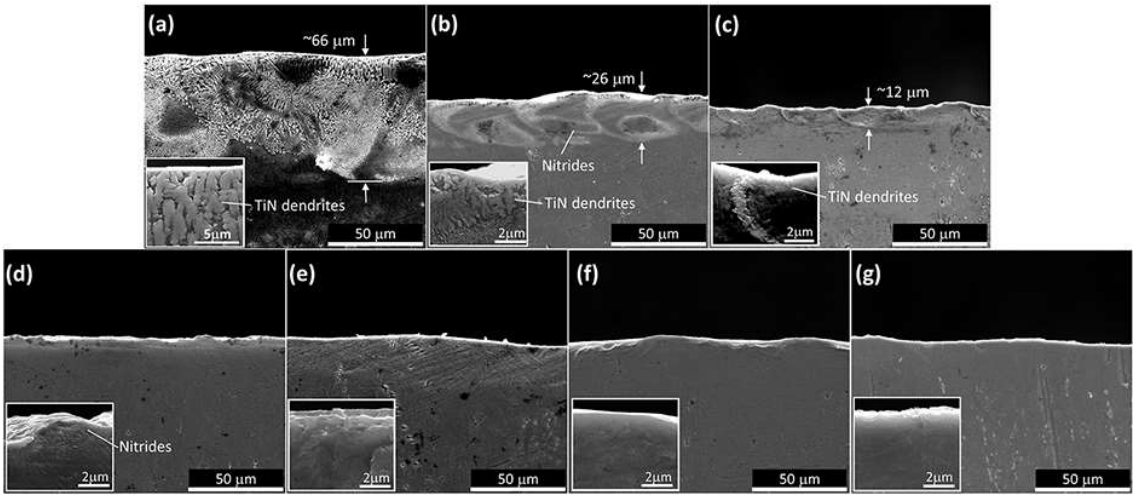

Figure 4.3. SEM images showing the microstructures of cross sections of the laser processed surfaces (a) Ti-N100, (b) Ti-N400, (c) Ti-N1600, (d) Ti-N75%, (e) Ti-N50%, (f) Ti-N20% and (g) Ti-N0%. The inserted images demonstrate the cross section morphology using larger magnifications.

Figure 4.4 displays the morphology of the laser processed surfaces with the laser parameters shown in Table 4.1. Evidently, the whole sample surfaces were fully covered with laser scanning tracks, and the slower the laser scanning speed yields the wider the laser scanning tracks (Figs. 4.4 (a), (b) and (c)). Cracks are observed on the surface of Ti-N100 in Fig. 4.4 (a), which are indicated by white arrows, while no obvious cracks were seen on the surfaces of the other samples. This phenomenon is due to the induced thermal stress, as well

as the thick TiN layer on Ti-N100 surface. And it was already reported that thermal stresses could cause cracks in brittle TiN layers [222]. Interestingly, the cracks show similar intervals and are orientated preferentially vertical to the laser scanning direction within one single laser scanning track. Similar observation was also reported by Abboud [222]. Based on Abboud's research, thermal stress energy gradually accumulates in the shrinkage melt volume, and when reaching a critical value, cracks generate to release the excess energy. Besides, the Gaussian energy distribution feature of the laser spot makes the center of laser scanning tracks hotter than the out edges [222], and cracks initiate from the first solidified edge section and then propagate to the hotter center zone during the cooling process. The wavy ripple morphology is obvious when pure N_2 is applied (Figs. 4.4 (a), (b) and (c)). Closer observation reveals that the ripples become finer with faster laser scanning speed. As shown in Fig. 4.4 (d), ripples are still observed on Ti-N75%, however, with irregular shapes, while no ripples are seen on Ti-N50%, Ti-N20% and Ti-N0% (Fig. 4.4 (e), (f) and (g)). This phenomenon is due to the quick nitrogen absorption during the laser nitridation process when N_2 content is over 75%. According to the precious study by the authors, under similar laser melting conditions, the diffusion coefficient of nitrogen (ambient air condition) into titanium was estimated from 4.00×10^{-5} to 4.24×10^{-2} cm^2/s [233]. The generated TiN greatly deteriorates the fluidity of the liquid phase, hence rending to retain the ripple features on the sample surfaces. Meanwhile, the intake of nitrogen is quite limited when N_2 content is below 50 %, and Ti-N50%, Ti-N20%, and Ti-N0% show quite similar behaviors of laser melted liquid phase on the surfaces, leading to almost identical surface morphologies.

Surface roughness test results (root mean square roughness, S_q; average roughness, S_a) of the laser nitrided titanium surfaces are indicated in Fig. 4.5 (a). Agreeing with the observations above (Fig. 4.4), the surface roughness of sample processed at low scanning speed is obviously higher than that of the samples irradiated with faster laser scanning speeds. For

example, the S_q of the surfaces of Ti-N1600, Ti-N400 and Ti-N100 are 0.944 ± 0.200, 2.534 ± 0.668, and 6.359 ± 0.109 μm, respectively. Besides, surface roughness enhances as nitrogen content reaches 100% (i.e. Ti-N400), while surface roughness changes marginally when nitrogen content is less than 75%. Therefore, surface roughness is controlled by both nitrogen content in the atmosphere and laser scanning speed, and the determined roughness results agree with previous study [147]. Figure 4.5 (b) shows the representative image indicating the roughness results obtained from the optical profilometer, which reveals the ridges and troughs features together with the ripple features.

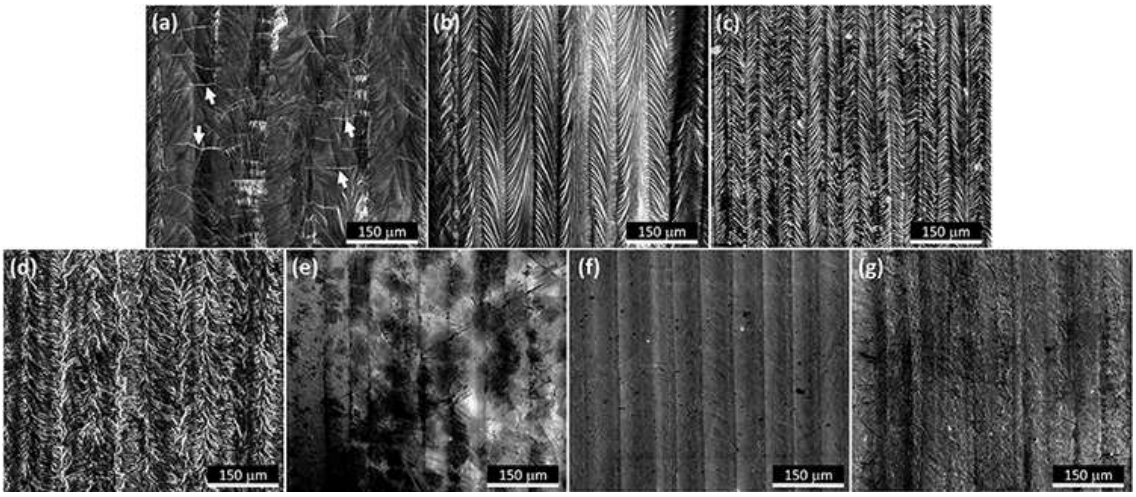

Figure 4.4. SEM images showing the top view of the laser irradiated surfaces (a) Ti-N100, (b) Ti-N400, (c) Ti-N1600, (d) Ti-N75%, (e) Ti-N50%, (f) Ti-N20% and (g) Ti-N0%.

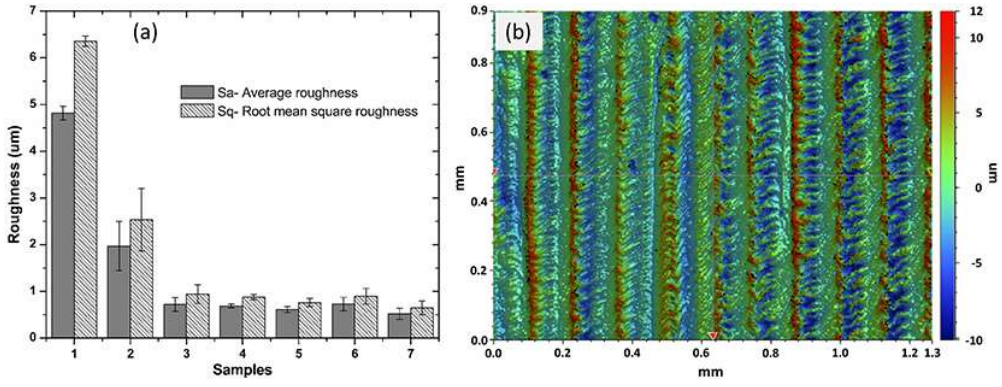

Figure 4.5. Images showing surface roughness test results of the processed sample surfaces. (a) The results of both the root mean square roughness (Sq) and the average roughness (Sa) and, (b) the representative image showing the surface roughness (Ti-N400).

Figure 4.6 depicts the hardness results obtained from the nano-indentation tests, and the standard deviation is also presented to show the variance of the tests. And it reveals differing hardness variation behaviors for the samples. Qualitatively, the hardness declines as it goes from the outermost surface to the base titanium, and gradually converges with that of other samples at the depth above 170 μm for the Ti-N100 case. And this observation agrees with previous studies [234, 235]. Ti-N0% shows almost constant hardness within the detection depth except the top surface area (with depth less than 20 μm), where slightly higher hardness (over 3.0 GPa at the depth 20 μm) than the base titanium (around 2.5 GPa) is observed, which is ascribed to the rapid cooling (quenching) effect of laser processing [236]. Ti-N50% and Ti-N20% show similar hardness variation behaviors with slight hardness increase on the outermost surface areas due to both the absorption of nitrogen and the fast cooling effect. Ti-N75% shows comparable hardness with Ti-N0%, Ti-N20% and Ti-N50% apart from the clearly increased hardness at the depth of 20 μm, which is attributed to the non-uniform phase distribution based on Fig. 4.3. The hardness profile of Ti-N100 behaves quite different, which can be divided into three regions, the depth less than 80 μm (region 1), from 95 μm to 155 μm (region 2) and above 170 μm (region 3), which are indicated in Fig. 4.6. Specifically, region 1 exhibits the maximum hardness among all the samples, and is determined over 6.9 GPa, around three times of the base titanium. The enhanced hardness in region 1 stems from the dense and hard phase (mainly TiN), which strongly hinders the movement of dislocations. However, it is worth noting that the reported hardness of compact TiN is approximately 17 GPa (testing force of 980 mN) [237], over twice of the maximum hardness acquired in this chapter. This can be interpreted by the distribution (or volume fraction) of TiN phase near the surface of Ti-N100 (shown in Fig. 4.3 (a)), where TiN exists as dendrites rather than a fully dense state, causing a decreased hardness. Katahira et al. [163] also observed similar results, with a 100-mN indentation force, a surface hardness of 12 GPa was obtained. Region 2 represents the heat-

affected zone (HAZ), the hardness of which is around 50 % higher than that of the base titanium, which is ascribed to the martensitic transformation resulted from the extremely rapid cooling rate during the laser nitridation process [142]. Noteworthily, the standard deviations in the two regions are large, which is due to the non-uniform phase distributions (i.e., grain boundary and grain interior). Region 3 displays almost identical hardness with the other samples at the same depth level, demonstrating negligible influence of laser irradiation on this region. Both of Ti-N400 and Ti-N1600 show high hardness 5 μm beneath the top surface (5.6 GPa and 5.3 GPa, respectively).

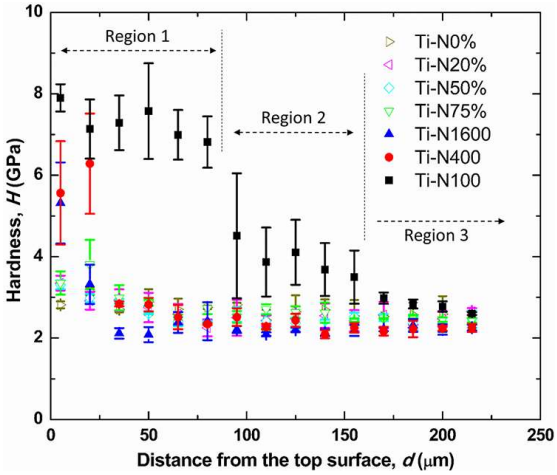

Figure 4.6. Surface hardness test results of the different samples by nanoindentation technique.

However, due to the inhomogeneous distribution of titanium nitrides (Figs. 4.3 (b) and (c)), the hardness is lower than that of the sample Ti-N100. However, when the detection depth reaches 20 μm, the hardness of Ti-N400 goes up to 6.3 GPa because of the enrichment of titanium nitrides (shown in Fig. 4.3 (b)), while the hardness of Ti-N1600 slips and becomes comparable to that of the samples processed under dilute N_2 environment. As the detection spots go deeper to 50 μm, the hardness of Ti-N400 becomes comparable with the samples treated with the same laser scanning speed, while Ti-N1600 exhibits lower hardness due to the negligible influence of laser irradiation at this depth, and the detected hardness is close to the

base titanium. When the depth is over 65 μm, the hardness testing results of all the samples except Ti-N100 overlap one another. Therefore, the generated TiN layer after laser processing can efficiently enhanced the surface hardness of titanium, while only a slight hardness improvement is achieved under dilute N_2 conditions due to the limited amount of titanium nitrides formed.

4.3.2 Bio-compatibility performance of laser nitrided surfaces

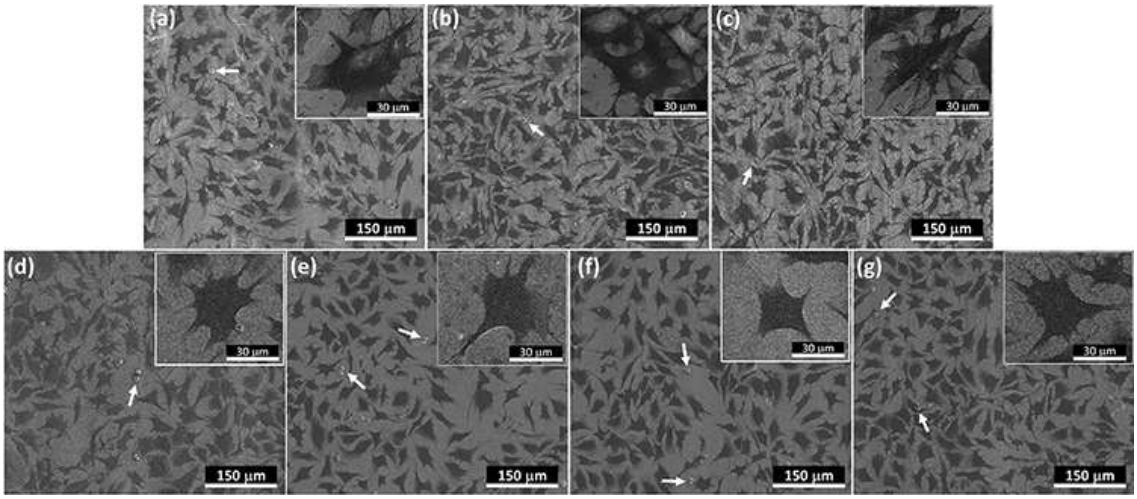

Figure 4.7. SEM images illustrating the cell adhesion on the laser processed sample surfaces (a) Ti-N100, (b) Ti-N400, (c) Ti-N1600, (d) Ti-N75%, (e) Ti-N50%, (f) Ti-N20% and (g) Ti-N0%. The inserted images show the cell morphology with a larger magnification. Round-shape apoptotic cells are indicated with white arrows.

Biocompatibility characterization as performed on Ti samples. Cell adhesion, proliferation and apoptosis rate investigations were conducted to examine the cellular response to the sample surfaces after 24 h incubation. According to Fig. 4.7, all the sample surfaces exhibit a good affinity for the MLO-Y4 cells. The cells distribute randomly but uniformly on the sample surfaces after incubation. Meanwhile, clear filopodia is observed from the incubated cells (inserted images in Fig. 4.7), distinguished from the initially cultured cells round shapes. However, several round-shape cells also exist on all the sample surfaces shown in Fig. 4.7, indicated by the white arrows. Initially, these cells attached on the sample surfaces, however, failed to grow and spread, finally remained the shapes. To distinguish the viable and apoptotic

cells, all the nucleus of the cells (including the viable and apoptotic) are stained in blue, while those of the apoptotic are stained in red. By capturing and overlapping these two images, nucleus in magenta (mixture of blue and red) indicate apoptotic cells, while those in blue represent viable cells. Figure 4.8 exhibits a representative image of Ti-N400 sample after overlapping. Inspiringly, the viable and apoptotic cells can be distinguished easily; and the proliferation and apoptosis behavior of the cells on the sample surfaces can be determined.

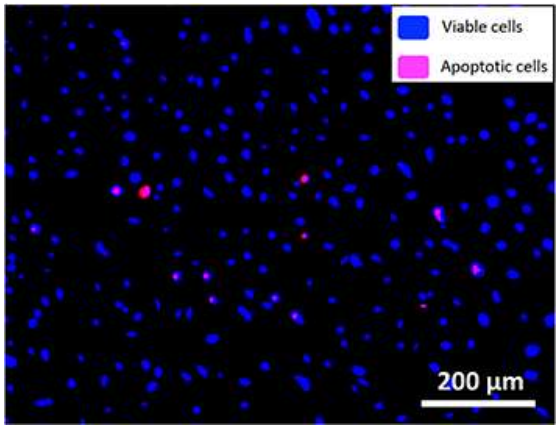

Figure 4.8. Representative composite cell viability image of Ti-N400.

According to Fig. 4.9 (a), no significant variance in terms of the cell numbers is observed after 24 h incubation, which agrees with a previous study [238], which discovered that TiN layer showed negligible effect on the proliferation of MG-63 cells. As the originally seeded cell density was 2×10^4 cells/cm^2, a two-time cell proliferation was achieved after 24 h incubation, showing a good biocompatibility with the α-Ti or TiN (or the α-Ti/TiN coexistence) surfaces. The apoptosis rate of the cells is shown in Fig. 4.9 (b), based on which, evidently, the samples can be divided into two groups. The first group of samples includes Ti-N50%, Ti-N20% and Ti-N0%, and the second group of samples includes Ti-N100, Ti-N400, Ti-N1600 and Ti-N75%. No remarkable difference is observed in terms of the apoptotic proportion within each group. However, the apoptosis rate of the second group is clearly lower than that of the first. It was reported that cell adhesion is controlled by chemical composition and surface topography

of the implant material [239]. A rough implant surfaces (micro-scale) can significantly improve primary fixation, mechanical anchorage, cell-implant attachment, and bone osseointegration [240, 241]. According to the observation above, surfaces of Ti-N100, Ti-N400, Ti-N1600, and Ti-N75% are clearly rougher than that of Ti-N50%, Ti-N20% and Ti-N0% (Figs. 4.4 and 4.5). Therefore, the surface features should be one of the reasons resulting in the higher apoptosis rate for the first group. Direct exposure of α-Ti phase to the cells, could be another possible reason leading to this phenomenon. The surface energy of TiN was discovered higher than that of titanium [238, 242, 243], and the increased surface energy improves cellular adhesion and proliferation on material surfaces [244, 245].

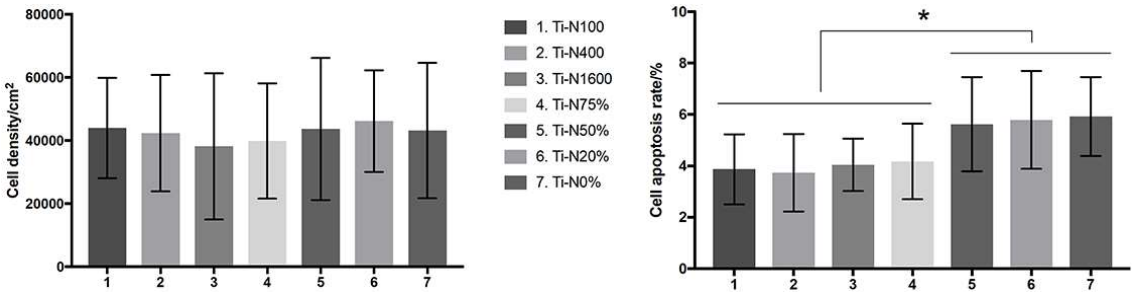

Figure 4.9. Images illustrating cell densities (a) and cell apoptosis rate of the samples (b). $p < 0.05$ indicates strategically significant and is denoted by *. The data is shown by standard deviation along with average.

4.3.3 Corrosion performance of the samples after laser nitridation

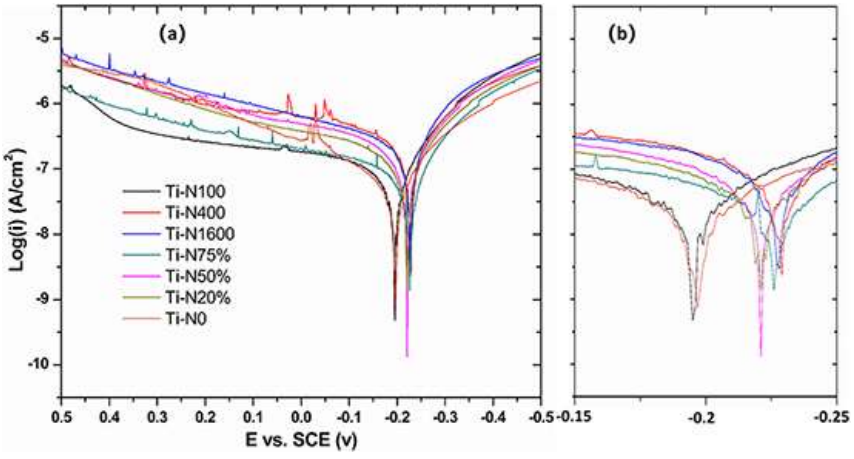

Figure 4.10. Images showing the potentiodynamic polarization curves of samples. (a) exhibits a wider range result, while (b) shows a narrower range result.

The representative potentiodynamic polarization curves of the samples in the SBF solution are shown in Fig. 4.10. Clearly, compared with the other counterparts, the curves of Ti-N0% and Ti-N100 are most positive-shifted, indicating the lowest tendency to corrosion. Based on Fig. 4.10 (b), Ti-N50% and Ti-N20% show slightly left-shifted curves compared with Ti-N400, Ti-N1600 and Ti-N75%, which demonstrates better corrosion performance. Table 4.2 shows the details of the corrosion properties, which reveals an increased corrosion potential (E_{corr}) (-0.199 V) for Ti-N100, followed by Ti-N50%, Ti-N20% and Ti-N0%, while Ti-N1600, Ti-N400 and Ti-N75% the lowest E_{corr}. The results obtained in this study are in line with previous studies [147, 246, 247] (shown in Table 4.2), i.e. the E_{corr} in Hank's solution of laser nitride surface of CP titanium (processed under pure N_2 atmosphere) is -0.220 V. Considering the smaller E_{corr} of CP titanium (Table 4.2), clear improvement of E_{corr} after laser nitridation was achieved. Ti-N100 is covered by thick TiN dendrites with columnar structures (Fig. 4.3 (a)), and the continuous and compact surface layer makes the surface less likely to be corroded [147, 149]. The improvement of E_{corr} Ti-N0% is due to the quick surface remelting in pure Ar environment, leading to a more uniform surface layer, making it less prone to corrosion [248].The nitrogen intake in the surfaces of Ti-N50% and Ti-N20% are most likely in the form of solid solution atoms. Consequently, in terms of corrosion performance, the surfaces of Ti-N50% and Ti-N20% behave similarly with that of Ti-N0%.

The oxygen distribution on top surfaces of the samples Ti-N100 was evaluated (Figs. 4.11 (a) (b)) and Ti-N1600 (Figs. 4.11 (c) (d)) both before and after corrosion characterization. Obviously, the possibility of localized corrosion types such as pitting is opted out, where corrosion products are confined to a small area due to the uniform distribution of oxygen after corrosion tests, which is in accordance with the polarization curves, where no sudden jump in corrosion current density in anodic branch is observed.

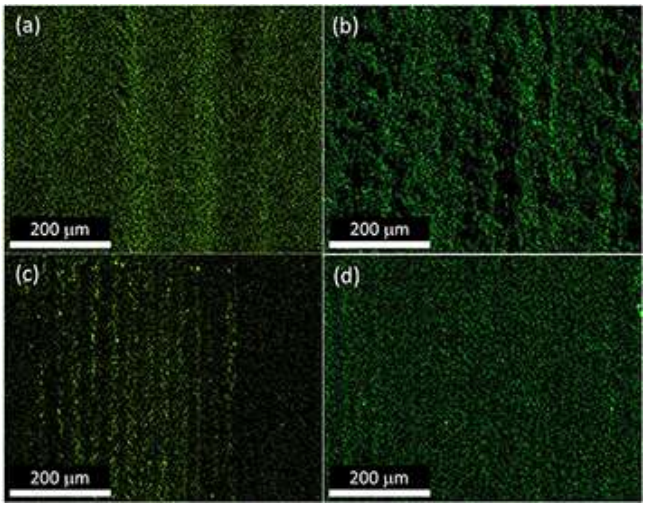

Figure 4.11. Images showing the EDS mapping results of oxygen distribution on the sample surfaces. Ti-N100 sample (a) before corrosion and (b) after corrosion, Ti-N1600 sample (c) before corrosion and (d) after corrosion.

Table 4.2. Corrosion potential (E_{corr}), corrosion current density (i_{corr}), and corrosion rate values of the samples, together with the corrosion results from literature review

Sample	Corrosion media	E_{corr} (V)	i_{corr} (μA cm^{-2})	Corrosion rate (× 10^{-3} mpy)
Ti-N100	SBF	-0.199 ± 0.023	0.054 ± 0.011	2.198 ± 0.448
Ti-N400		-0.227 ± 0.028	0.101 ± 0.037	4.110 ± 1.506
Ti-N1600		-0.227 ± 0.023	0.124 ± 0.035	5.046 ± 1.526
Ti-N75%		-0.232 ± 0.043	0.104 ± 0.020	4.232 ± 0.814
Ti-N50%		-0.218 ± 0.004	0.030 ± 0.012	1.221 ± 0.488
Ti-N20%		-0.215 ± 0.012	0.047 ± 0.001	1.913 ± 0.016
Ti-N0%		-0.210 ± 0.018	0.037 ± 0.009	1.506 ± 0.366
CP-Ti [147]	Hank's solution	-0.398	0.856	/
Nitrided Ti [147]		-0.220	0.634	/
CP-Ti [246]		-0.470	2.760	/
Cp-Ti [247]	Kokubo and Takadama's SBF	-0.491	2.000	19.8

The inferior E_{corr} of Ti-N400, Ti-N1600 and Ti-N75% is mainly ascribed to both galvanic corrosion and intergranular corrosion. Unlike Ti-N100, titanium nitrides on the surfaces of the three samples are non-uniformly distributed and clearly smaller sized. Galvanic coupling effect is caused by the inhomogeneous phase distribution, with the inert TiN phase and the matrix (titanium) acting as the cathode and anode, respectively, consequently accelerating the corrosion rate of titanium. Intergranular corrosion preferentially occurs along

the grain boundaries (GBs) for the higher energy condition of the localized regions. Finer grains leads to higher GBs density, making the surfaces prone to corrosion attack [249]. As a result, the small titanium nitrides with a low volume fraction on the surfaces of Ti-N400, Ti-N1600 and Ti-N75% provide more paths for corrosion agent to penetrate into the surface, causing higher corrosion tendency [147].

The corrosion current density (i_{corr}) and the corrosion rate results are summarized in Table 4.2. Clearly, the two parameters are directly proportional to each other, which can be described in the equation below,

$$\text{Corrosion Rate (Mils per year)} = 0.13 \times i_{corr} \times (EW)/d \quad (4\text{-}1)$$

where d and EW indicate the density (4.517± 0.060 g/cm^3) and the equivalent weight (11.975) of Ti, respectively. In accordance with the E_{corr}, Ti-N400, Ti-N1600 and Ti-N75% possess clearly larger corrosion rates. In additional to the aforementioned galvanic corrosion and inter-granular corrosion, this is also attributed to the surface roughness of the samples. According to previous studies [250], a rougher surface enlarges the interaction area with the corrosion solution, therefore increasing the corrosion current density and corrosion rate, making the surface prone to corrosion. Meanwhile, although the surface of Ti-N100 is rougher than that of Ti-N50%, Ti-N20%, and Ti-N0% (Fig. 4.5), thanks to the dense and compact TiN dendrites layer, the corrosion rate of the former is quite close to the latter three samples. It is reported that CP titanium laser nitrided under pure nitrogen displays smaller i_{corr} than that of untreated CP titanium in Hank's solution [147] (Table 2). Therefore, it is reasonable that the corrosion resistance of Ti-N100, Ti-N50%, Ti-N20%, and Ti-N0% should be higher than that of untreated pure titanium counterparts. A relatively well-defined passivation plateau formed in the anodic domain from -0.122 V to 0.368 V of the sample Ti-N100 (passivation range of 0.490 V), while all the other counterparts displays no passivation stages. Besides, the slope of the passivation curve and the passivation current density in the anodic domain of Ti-N100 are

always smaller than that of the other samples. This phenomenon reveals the reliability and stability of the surface of Ti-N100 in SBF. Ti-N0% shows the superior E_{corr} and i_{corr}, however, the largest slope of the polarization curve and the high corrosion current density in the anodic domain illustrate its inferior corrosion performance. Based on the discussion above, to acquire excellent corrosion performance, a thick and continuous TiN layer should be coated on the titanium surface.

4.4. Conclusions

In this chapter, laser nitridation of titanium was evaluated to improve both corrosion resistance performances and bio-compatibility. By adjusting N_2 atmospheres and laser scanning speeds, titanium nitride surface layers with varying thickness, phases, composition and roughness were acquired. Bio-compatibility and corrosion resistance tests were performed to identify the best laser nitridation parameters, and the conclusions below were reached.

(1) With the increase of laser scanning speed and the decrease of N_2 content, the thickness of titanium nitride layer decreases. A thick (~ 66 μm) titanium-nitride dendrites layer is generated on the surface of Ti-N100, while non-uniform titanium-nitride layers appear on Ti-N400 and Ti-N1600 (with thickness ~26 μm and ~12 μm, respectively). There is also a thin titanium-nitride layer on the surface of Ti-N75%. Under diluted N_2 conditions, no coating layer is detected on Ti-N50%, Ti-N20% and Ti-N0% samples. The surfaces of Ti-N100, Ti-N400, Ti-and N1600 after laser processing are rough and show wavy ripple surface features. Owing to the dense and thick titanium nitride layer, Ti-N100 shows the highest surface hardness, which is around three times of the base titanium matrix.

(2) No obvious differences in cell adhesion and proliferation are detected; the high apoptosis rates associated with Ti-N50%, Ti-N20% and Ti-N0% reveal the positive effect of laser nitrided coatings for improved bio performance.

(3) Due to the thick and dense layer of TiN dendrites in the outermost surface, Ti-N100 shows the best corrosion resistance, while the other samples exhibit inferior corrosion performance ascribed to the non-uniformly distributed phase constituents on the outermost surface.

(4) For achieving the optimal corrosion resistance performance and biocompatibility, a dense and thick titanium-nitride layer is beneficial, which can generate in a pure N_2 environment together with a high laser energy density, i.e. the Ti-N100 case in this study.

Chapter 5. Mechanical, Thermal, and Corrosion Properties of Cu-10Sn Alloy Prepared by Laser-Powder-Bed-Fusion Additive Manufacturing

5.1. Introduction

Cu-Sn alloys (tin-bronze) are widely applied for technological applications. For example, due to the high activation energy for electromigration, Cu-Sn (0~2 wt. % Sn) alloys are better chip interconnects than their Al-Cu counterparts [251]; Ascribed to the excellent mechanical properties, high thermal conductivity, and the good wear and corrosion resistance, Cu-10Sn alloy is qualified for making bearings [252]. Traditional methods, such as casting and mechanical alloying, for making Cu-Sn alloy parts have been extensively investigated [253, 254]. However, the Cu-Sn alloy parts made by additive manufacturing are less studied. Among all the metal additive manufacturing methods, laser-powder-bed-fusion based additive manufacturing (LPBF-AM) is one of the most prevailing strategies, where a focused laser beam is utilized to melt and fuse metallic powders to prepare parts with complex shapes and near full density [255]. Due to the extremely fast cooling rate and small size of the laser melt pool, LPBF-AM parts possess unique microstructures and/or phases that are varying from those made by traditional processes (wrought and cast) [255, 256]. Several Cu-Sn alloy parts have been reported successfully fabricated by LPBF-AM, i.e. Cu-4Sn alloy [124], Cu-4.3Sn alloy [125], Cu-10Sn alloy [126-128], and Cu-15Sn alloy [119]. However, microstructure and mechanical property evaluations are the main research focus for the AM Cu-Sn alloy mentioned above.

This chapter was previously published as Congyuan Zeng, Bin Zhang, Ali Hemmasian Ettefagh, Hao Wen, Hong Yao, W.J. Meng, Shengmin Guo. "Mechanical, Thermal, and Corrosion Properties of Cu-10Sn Alloy Prepared by Laser-Powder-Bed-Fusion Additive Manufacturing", Additive Manufacturing, 2020. Reprinted by permission of Elsevier.

For other applications, corrosion and thermal properties are of significance as well. Corrosion behavior and thermal conductivity of cast Cu-Sn alloys with controlled tin contents have been extensively studied [123, 257-262]. And it was pointed out that thermal conductivity of cast Cu-Sn alloys have a strong dependence on temperature and Sn content, which increases as the testing temperature increases and Sn content decreases [257]. Corrosion behaviors of Cu-Sn alloy parts (manufactured with traditional strategies) were well investigated for different Sn contents and environments [258, 261, 263, 264]. After immersion in a corrosive environment, two types of surface layers can be formed on Cu-Sn alloys. Type I is called noble patina, which is mainly a protective layer with copper oxide on the surface. Type II is called vile patina, which involves the generation of a copper chloride layer [123, 262]. In order to understand the overall performance of Cu-Sn alloy parts manufactured by additive manufacturing, the present chapter reports the study of corrosion and thermal properties, together with mechanical performance, of Cu-10Sn alloy parts fabricated by the LPBF-AM method.

5.2. Experimental procedures

5.2.1. Sample preparation

Cu-10Sn alloy powders (spherical shape, Concept-Laser GmbH) are used in a LPBF-AM system (Concept-Laser Mlab cusing R) with the shielding Ar gas to prepare the Cu-10Sn samples. Figure 5.1(a) demonstrates the shape and size of the Cu-10Sn powders. With the Mastersizer 3000 (Malvern AERO S, dry powder dispersion mode), the size distributions, d10, d50, and d90 were determined to be 15.5 μm, 25.9 μm, and 37.6 μm, respectively. The AM parameters are shown below, scanning speed 1200 mm/s, laser power 95 W, powder layer thickness 15μm, and hatch space 50 μm. “Islands laser scanning strategy” is applied with the island size of 5×5 mm^2 (shown in Fig. 5.1(b)), where Axis Z represents the building direction.

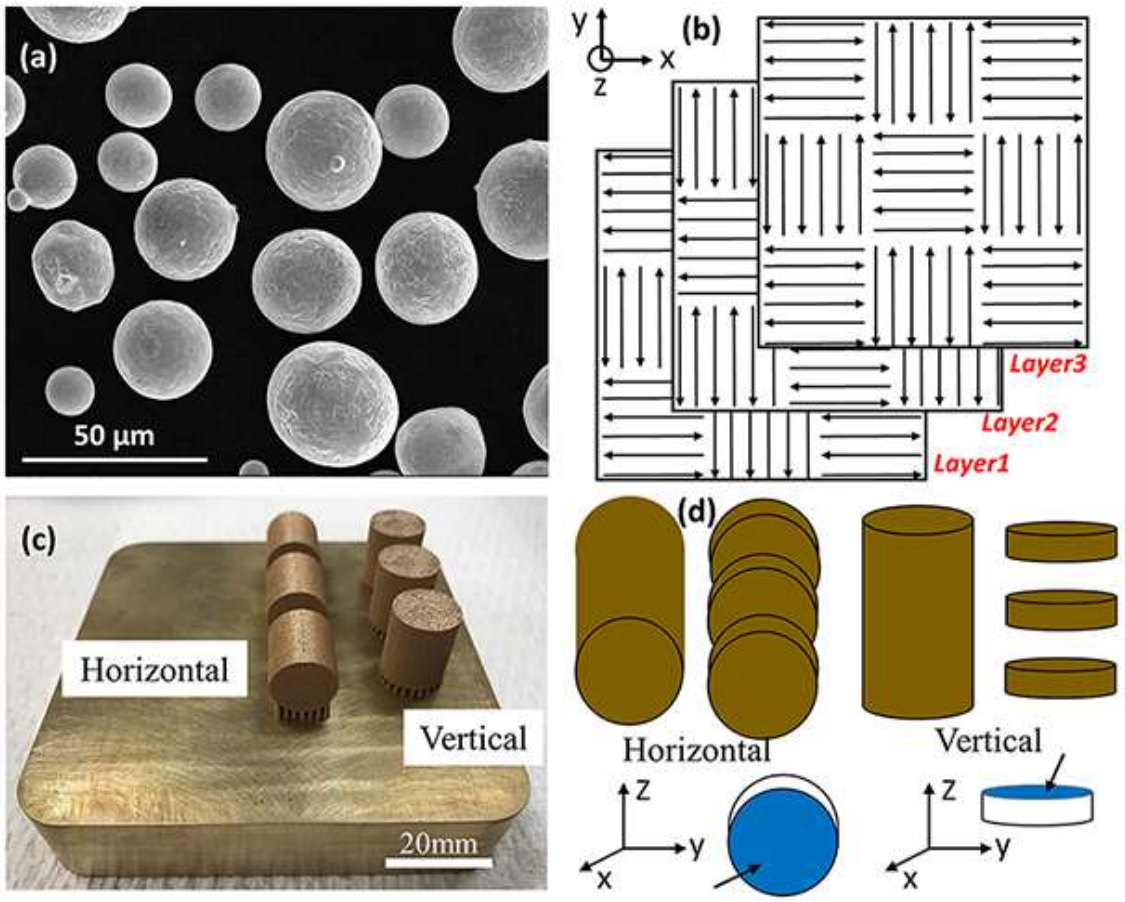

Figure 5.1. (a): A SEM image of Cu-10Sn powders; (b): A schematic showing the laser "islands scanning strategy"; (c): As-fabricated samples, Vertical and Horizontal building orientations; (d): A schematic illustration of Vertical and Horizontal samples with shaded surfaces subject to the following microstructural and phase evaluations.

To investigate the effect of building orientation on the properties, two groups of cylindrical rod samples were fabricated, according to Fig. 5.1(c), with the central axis oriented in either vertical or horizontal direction. Figure 5.1(d) demonstrates the machining procedures for microstructural, phase, thermal conductivity, mechanical property, and corrosion evaluations of as-fabricated and annealed samples. To unveil the influence of heat treatment on microstructure/phase evolution and properties of LPBF-AM samples, vacuum annealing was performed (~10^{-7} torr) at temperatures of either 600 ℃ or 800 ℃ for 1 hour, with the programmed heating and cooling rates of 10 ℃/min. In this chapter, samples are denoted by

both the building orientations and the heat treatment conditions, namely AF-Horizontal, AF-Vertical, 600-Horizontal, 600-Vertical, 800-Horizontal, and 800-Vertical.

5.2.2. Testing procedures

Cylindrical rod samples (Φ3.0 mm × 4.0 mm) were machined from the LPBF-AM parts for mechanical compression testing. Both the top and bottom surfaces of the testing samples were mechanically ground and polished with SiC papers of 320, 600, 800, 1000 and 1200 grits, successively, to a mirror finish. To assure the credibility of the testing results, three samples for each fabrication and heat treatment condition were tested at room temperature using a custom-built compression stage on a MTS 858 uniaxial testing system. The previous study [265] illustrates further details of the protocol for uniaxial compression testing.

A Netzsch LFA 467 HT HyperFlash®- light flash apparatus was utilized to characterize the thermal diffusivity values, with a measuring temperature range from 25 ℃ to 1250 ℃. The dimensions of the as-fabricated samples were Φ14×15 mm, as shown in Fig. 5.1(c). Disk samples with the size of Φ12.56×2.55 mm were machined with a wire electrical discharge machining (EDM) system. And the top/bottom surfaces of the disks were ground with SiC papers to remove the contaminants after the wire EDM machining, followed by the cleaning process with ethanol and dried in air. Thermal conductivity (K) was calculated with the following equation,

$$K = \alpha \cdot C_p \cdot \rho \tag{5-1}$$

Where α, C_p, and ρ are thermal diffusivity, specific heat, and the density of the sample, respectively. The densities (ρ) of the samples were measured with Archimedes principle before the thermal conductivity testing. The surfaces of the reference sample and the target samples were coated with a thin and uniform graphite layer to insure identical heat absorption. Thermal diffusivity was measured directly with LFA 467 apparatus between 25 ℃ and 250 ℃, for the credibility of the testing results, three samples for the same fabrication and heat treatment

condition were tested, while specific heat was calculated after the testing with the equation below,

$$C_{pr} \cdot m_r \cdot \Delta T_r = C_{pt} \cdot m_t \cdot \Delta T_t \quad (5\text{-}2)$$

where ΔT indicates the maximum temperature rise of the sample within each flash light shot, m represents the mass of the sample; Subscripts t and r indicate the target and reference samples, respectively. This calculation is based on the assumption that both the reference and target samples absorb the same amount of heat. With the already known specific heat of the reference sample, specific heat of the tested samples can be estimated.

A 3-electrode standard corrosion cell was used to conduct the electrochemical characterizations, applying a platinum counter electrode, a saturated calomel electrode (SCE) as the reference electrode, and the target samples as the working electrode (exposed area around 1.13 cm^2). 3.5 wt.% NaCl water with naturally dissolved oxygen was used as the corrosion solution, and the corrosion tests were conducted at room temperature with a CHI-604C corrosion tester (CH Instruments, Inc). The duration for the open circuit potential (OCP) recording was ~60 hours, and Tafel curves were also obtained from -1.5 VSCE to 0 VSCE (rate of 1.67 mV/s). The sample surfaces were prepared by polishing with SiC paper with grit sizes of 320, 600, 800 and 1000 successively, then rinsing, and soaking in the test solution for 1 hour before the corrosion testing. To assure the reproducibility and credibility of the test results, all of the corrosion tests were conducted over three times. Weight loss test was also performed, and samples were then immersed in the solution for 11 days and the weight of corroded samples was measured every 24 hours. Before the measurements, all the samples were rinsed by deionized water, ethanol, and acetone, and dried in air.

5.2.3. Materials characterization

A ZEISS X-ray micro-CT system (Xradia 620 Versa) was used to obtain the 3D visualizations for distribution of internal porosity. AF-Horizontal and 800-Horizontal samples

(cubic shape, with the size around 3×3×3 mm^3) were evaluated with a 160kV/25W of energy/power and 3mm×3mm view field. Phase structures (θ-2θ scans) were characterized with X-ray diffraction on all the samples and the raw powders from 20° to 120° with a scanning step size of 0.026°. XRD Rietveld refinement was also conducted to determine the quantitative phase constituents of the AF sample with a FullProf package, which applies a fifth order polynomial function, a pseudo-voigt algorithm, and a least square refinement to model the background, fit the peak shape, and model the refinement weighting, respectively. The refinement process was kept performing until a close fit between the calculated and experimental patterns was obtained.

Scanning electron microscope (SEM) with electron backscatter diffraction (EBSD) and energy dispersive spectroscopy (EDX) attachments, was used for the composition and microstructure evaluation. Before the EBSD characterization, the samples were ground and polished with the exactly same procedure above-mentioned to a mirror finish. The obtained EBSD data were also analyzed with the TSL OIM software to determine the grain size of the samples. Prior to the SEM examination, the polished samples were etched with the etching solution (mixture of 5g $FeCl_3$, 10 ml HCl, and 100 ml deionized water) at room temperature.

5.3. Results and discussions

5.3.1. Microstructure characterization

The XRD θ-2θ scan results were obtained for the Cu-10Sn pre-alloyed powders and all the powders (Figure 5.2). Obviously, two phases, α-Cu(Sn) phase (a Cu-rich phase) and the intermetallic compound δ-$Cu_{40.5}Sn_{11}$ phase (a Sn-rich phase), were identified. Meanwhile, the two phases (α and δ phases) are also observed in the AF-Horizontal and AF-Vertical samples, which is in accordance with other studies [119, 126]. However, a careful observation reveals that the diffraction peaks of α phase in AF samples shift to smaller angle side compared with that in the pre-alloyed powders. For example, the (111) peak of α phase in AF-Horizontal

sample is 42.87º (Fig. 5.2(b)), which is slightly smaller than that of raw Cu-10Sn powders (43.01º). This observation indicates Sn diffusion into the α phase during the LPBF-AM process. It is worth noting that, according to Figs. 5.2(a) and 2(b), all the samples contain only α phase after annealing, demonstrating a homogeneous distribution of Cu and Sn elements after annealing at 600℃/800℃ for 1 hour. Besides, the diffraction peaks of the samples after annealing became narrower than those of the AF samples, indicating grain growth as well as compositional homogenization. To figure out the quantitative phase constituents of AF samples, Rietveld refinement analysis of the XRD data of the representative AF-Vertical sample was performed (Fig. 5.2(c)). And when the phase constituents are assumed as the face-centered cubic (FCC) α-Cu phase and the δ-$Cu_{40.5}Sn_{11}$ phase, the XRD pattern of AF-Vertical sample fits well with the weighted profile reliability factor (R_{wp}) of 9.02 %. This further verifies that a coexistence of the $Fm\bar{3}m$ α-Cu (Sn) phase and the $F\bar{4}3m$ δ-$Cu_{40.5}Sn_{11}$ phase is in the as-fabricated sample. And the content of the δ-$Cu_{40.5}Sn_{11}$ phase in the AF-Vertical sample is determined as 25.9 wt.%.

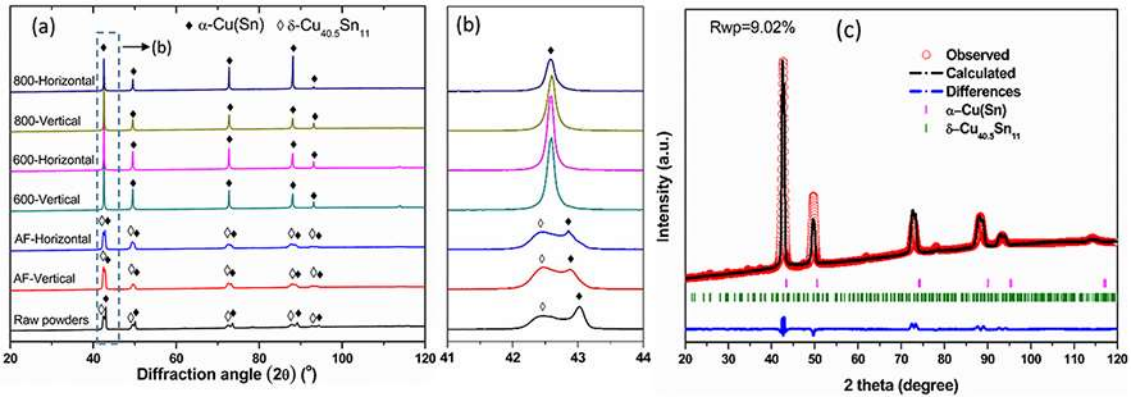

Figure 5.2. XRD analysis results and XRD Rietveld refinement analysis result. (a): The XRD results of the raw powders, and all the samples from 20˚ to 120˚; (b): The XRD results with a narrow angle range of 41-44º; (c) Rietveld refinement analysis of XRD spectrum of the AF-Vertical sample.

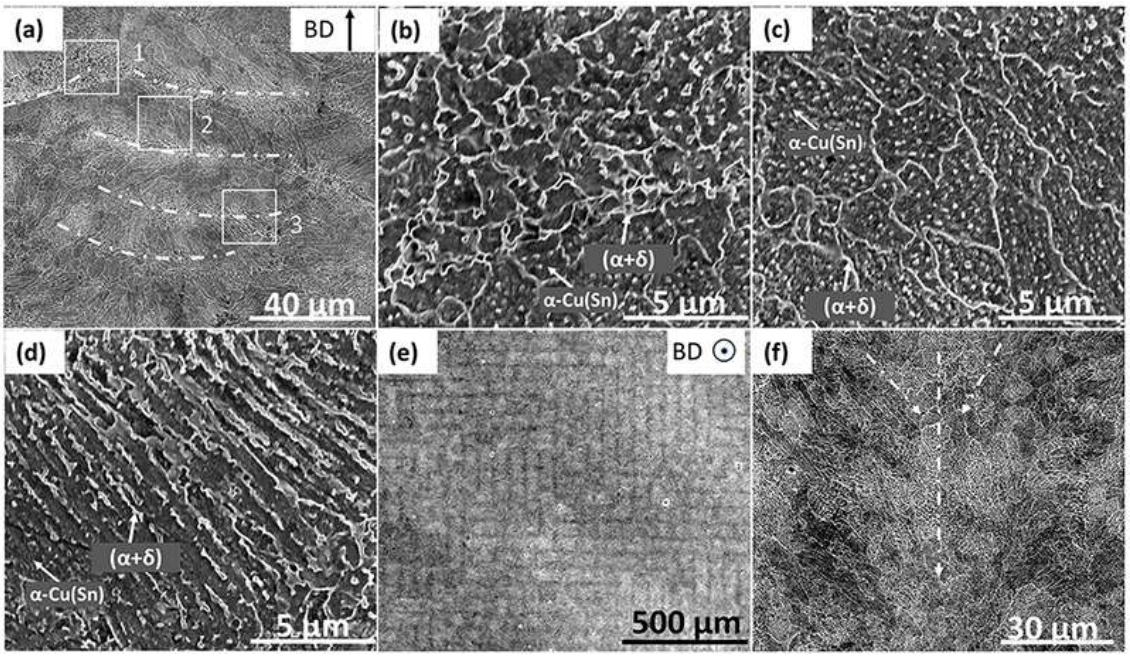

Figure 5.3. SEM images illustrating the microstructures of the AF samples. (a): AF-Horizontal sample; (b),(c),& (d): SEM images of microstructures of area 1,2,3, respectively; (e)&(f): SEM images of microstructures of an AF-Vertical sample.

The microstructures of the AF samples after etching are shown in Fig. 5.3. Figure 5.3(a) indicates a typical melt pool profile of the as-fabricated samples, marked with dash lines. And it reveals that the microstructure is not homogeneous, and due to the distinct microstructures, three different regions were divided, which are shown in Fig. 5.3(a), marked with squares 1, 2, and 3. Square 1 locates at the intersection region of two adjacent melt tracks, and the microstructures are shown in Fig. 5.3(b) with larger magnifications. According to Fig. 5.3(b), the microstructures are mainly cellular shaped, and a combination of α phase (grey regions) and (α+δ) eutectoid phase (bright rings) are observed, with the widths of the bright rings around 100 nm. Region 2 locates in the center of the melt track, and the microstructures are described in Fig. 5.3(a), where the α phase matrix and the (α+δ) phase white rings are detected, however, with the size larger than that in region 1. Region 3 is located across the boundary of melt pools with columnar structures (with spacing between them less than 1 µm, Fig. 5.3(d)), which grow preferentially towards the center of the melt pool along the temperature gradient direction.

Similar microstructure information was also reported elsewhere for the LPBF-AM Cu-10Sn alloy [126] and Cu-15Sn alloy [119]. The microstructures of the AF-Vertical sample are shown in Figs. 5.3(e) and 5.3(f), which clearly show the laser tracks, micron-sized pores, and the 50 µm laser scanning track width.

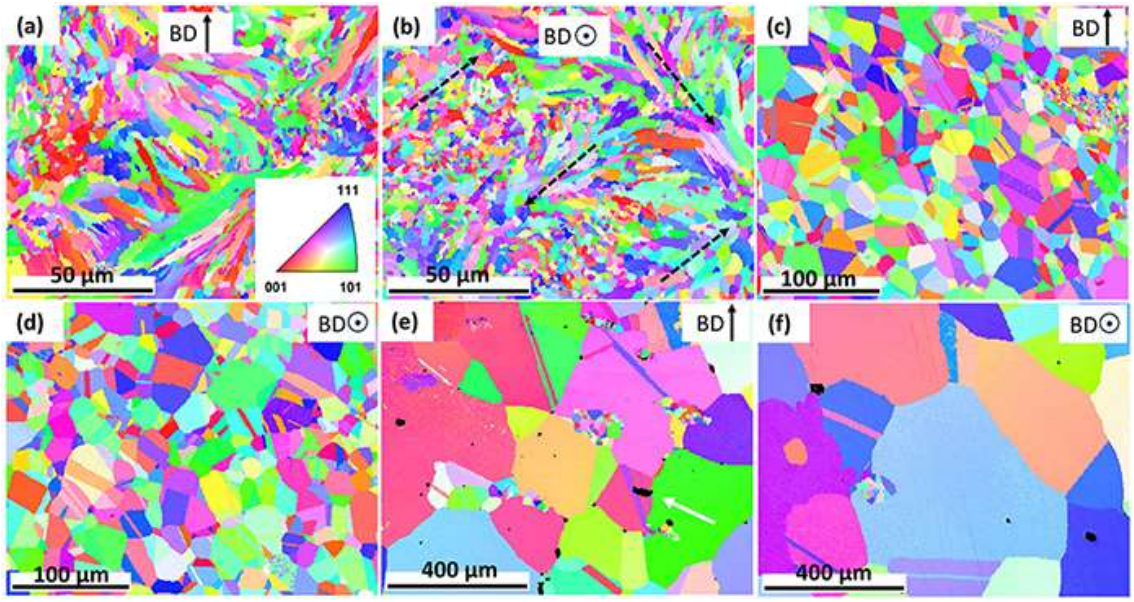

Figure 5.4. EBSD inverse pole figure (IPF) maps of microstructures of the samples (a): AF-Horizontal sample; (b): AF-Vertical sample; (c): 600- Horizontal sample; (d): 600-Vertical sample; (e): 800-Horizontal sample; and (f): 800-Vertical sample.

Fig. 5.4 illustrate the EBSD inverse pole figure (IPF) orientation maps of samples, and surfaces investigated are parallel to the building direction for Figs. 5.4(a), (c) and (e) (Horizontal samples), while the surfaces are perpendicular to the building direction for Figs. 5.4(b), (d) and (f) (Vertical samples). Figure 5.4(a) depicts the microstructure of the AF-Horizontal samples, which shows the complex shaped grains with both equiaxed and elongated grains. The elongated grains are tens of micron in length and grow across several layers. Similar to the columnar structures observed in Fig. 5.5 (d), the elongated grains do not grow strictly along the building direction, which is attributed to the complex thermal gradients originated from the island laser scanning strategy and the zigzag laser scanning directions used in this work. Similar microstructures were also observed in LPBF-AM AlSi10Mg parts [258]. Besides,

it is worth noting that when comparing Figs. 5.3(a) to (d) with Fig. 5.4(a), the microstructures revealed by SEM images and etching process are not necessarily grains because of the obvious size difference. And the microstructures observed in Fig. 5.4(a) should be more likely the sub-grain cellular structures, which were also reported in LPBE-AM alloy [266] and 316L alloy [267]. TSL OIM software was used to estimate the average size of the grains with the linear interception method, and for the AF-Horizontal sample the value of *d* was found ~2.1 μm. The EBSD orientation map of the AF-Vertical sample is shown in Fig. 5.4(b). Laser scanning tracks are easily distinguished (indicated by the black dashed arrows) based on the fact that grains preferentially grow towards the center of melt pools. Besides, the same with the AF-Horizontal sample, grains with different shapes are observed. And the measured size for the AF-Vertical sample is around 1.9 μm, comparable to that of the AF-Horizontal sample.

EBSD IPF orientation maps of VA samples are summarized in Figs. 5.4(c)-(f). Compared with the AF samples, after annealing grain morphologies change significantly, where the grains are almost equiaxed, and plenty of annealing twins are observed as well. The grain morphology of the 600-Horizontal sample is shown in Fig. 5.4(c). However, a small cluster of grains with sizes remarkably smaller than the other grains are observed, which should be due to the insufficient holding time at 600 ℃. Considering all the features in the 600-Horizontal sample, including the abnormally fine grains and intersection with twins, the average grain size was measured to be around 6 μm. Similarly, the average grain size of the 600-Vertical sample was determined to be around 8 μm, shown in Fig. 5.4(d). Dramatic grain growth was observed after annealing at 800 ℃ for 1 hour (depicted in Figs. 5.4 (e) and 4(f)). Abnormal grain growth occurred during the annealing process due to the observation of clusters of finer grains. And the estimated grain size of the for the 800-Horizontal and 800-Vertical samples are ~66 μm and ~120 μm, respectively, again including the twin intersections and finer grains. The huge difference in terms of the grain size observed in the two samples is

due to the existence of many more clusters of extremely fine grains in the 800-Horizontal sample.

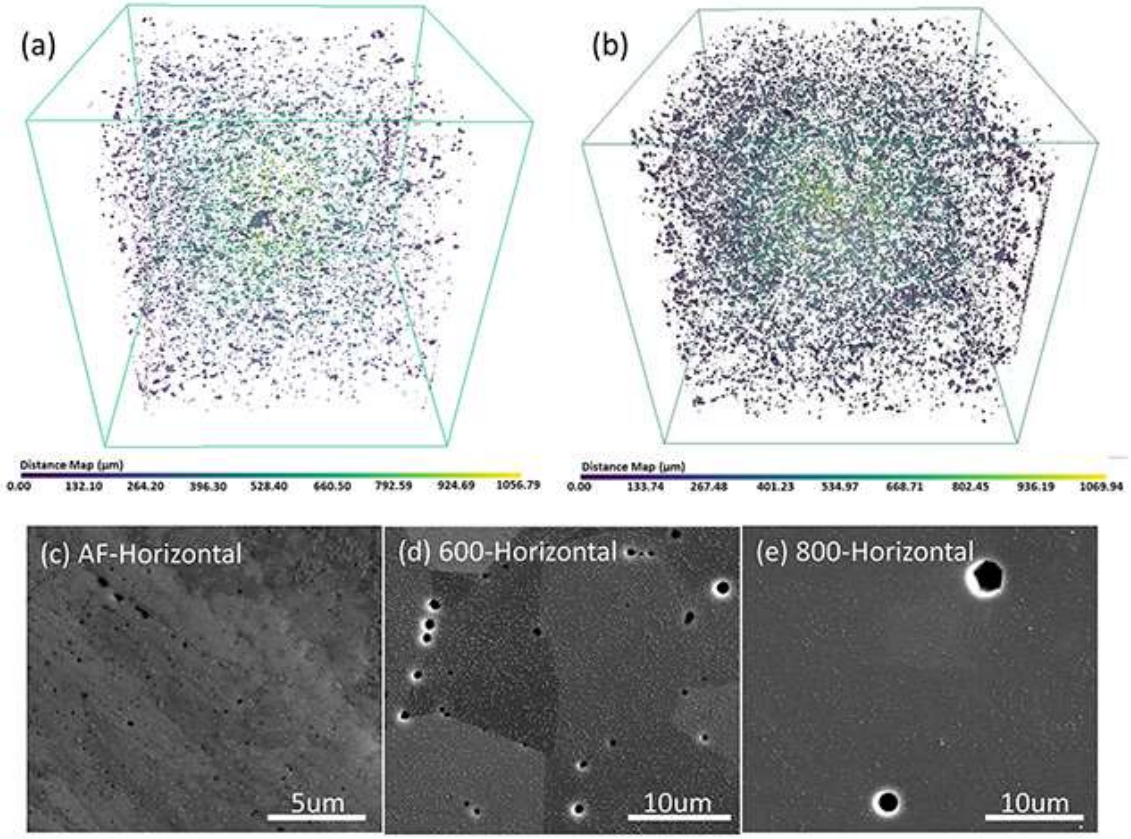

Figure 5.5. Images showing the pore structures. (a), (b) display the 3D visualization of pore structures of AF-Horizontal and 800-Horizontal samples, respectively. (c), (d) and (e) are SEM images demonstrating the sizes of pores for samples AF-Horizontal, 600-Horizontal and 800-Horizontal, respectively.

The 3D visualization results of the representative AF-Horizontal (Fig. 5.4 (a)) and 800-Horizontal (Fig. 5.4 (b)) samples are displayed in Fig. 5.5, which clearly reveal the pore structures and distributions in the samples. Generally, pores distribute uniformly in both the samples, and the pores in the AF-Horizontal sample are smaller than that in the 800-Horizontal sample. Besides, the porosities estimated are around 0.11% and 0.33% for the AF-Horizontal and 800-Horizontal samples, respectively. However, according to the bulk density evaluation results in Table 5.2, the densities of the two samples are nearly identical, which indicates almost the same porosity for the two samples. Take the pixel size (1.5 μm) used in the 3D visualization

examination into consideration, pores with the sizes greatly smaller than pixel size could not be captured. This reflects nano-scale pores existing in AF-Horizontal samples. Pore sizes distributions in the samples are exhibited in Figs. 5.5(c)-(e). Obviously, pore size increases with the increase of heat treatment temperature.

5.3.2. Mechanical response in uniaxial compression

The true stress vs true strain (σ-ε) curves of the samples acquired from the uniaxial compression characterization are summarized in Fig. 5.6. Early onset of plastic deformation occurred, which is most likely due the not perfectly aligned contacts between the top and bottom surfaces and the steel plates may still, though the top and bottom surfaces of the samples have been polished. As a result, significantly lower slopes compared to the theoretical elastic modulus of Cu-10Sn alloy of the initial part of the measured σ-ε curves are observed, which diminish at larger strains, indicating the compression stress is more reliable at larger strains. Obviously, the AF samples show the highest compression strength, while the VA samples possess lower strength values inversely related to the heat treatment temperature. Orientations of samples have negligible effect on the compression strength. The observation is clear for the samples after vacuum annealing for the grains are mainly equiaxed, which is, however, quite interesting for the as-fabricated case, where anisotropy usually happens that show significant influence on mechanical performance [268]. However, the heterogeneous distribution effect of the grains may be alleviated by the laser scanning strategy used in the present study. Compared to the Zig-Zag laser scanning strategy, island scanning strategy is beneficial for reducing the texture index and improving isotropic properties of LPBF-AM Inconel 718 parts [269] and LPBF-AM AlSi10Mg parts [270].

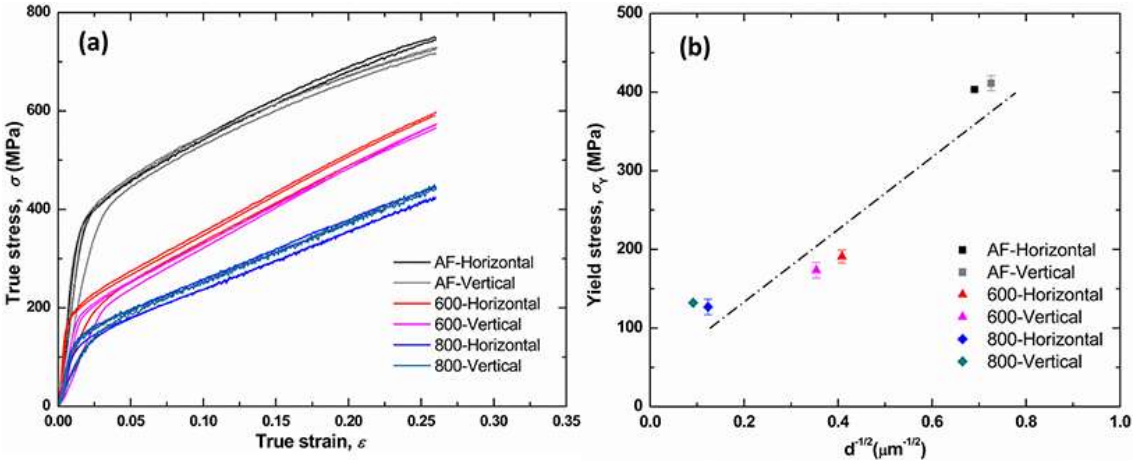

Figure 5.6. Mechanical response of as-fabricated and vacuum-annealed Cu-10Sn alloy 3mm diameter rod samples. (a): true stress-true strain curves obtained from uniaxial compression testing; (b): plot of yield stress vs. the inverse square root of the average grain size.

Interestingly, linear strain hardening, i.e., within the strain range of $0.05< \varepsilon <0.25$, is observed, where the measured true compression stress increases nearly linearly with the increase of true compression strain. Therefore, all the σ-ε curves within the strain range of 0.05 to 0.25 behave as straight lines in the form of

$$\sigma = \sigma_Y + k\varepsilon \tag{5-3}$$

where k, σ_Y are a constant and the intercept on the stress axis, respectively, and σ_Y was taken as the yield stress. The relation between the determined yield stress and the inverse square root of the average grain size of the samples are demonstrated in Fig. 5.6(b). The error bars on yield stress result from averaging the repeated compression test results. The clear linear relation between σ_Y and $1/\sqrt{d}$ (Fig. 5.6(b)) illustrates that the compression yield stress of samples follows the Hall-Petch scaling, specifically the yield stress correlates linearly with the inverse square root of the average grain size [271]. The yield stresses of 800-Horizontal and 800-Vertical samples are nearly the same (Fig. 5.6(b)), ~ 128.7 MPa, while the yield stresses of the 600-Horizontal and 600-Vertical samples are around 179.4 MPa, close to the value corresponding to conventional cast counterparts [126, 272, 273] (Table 5.1). The yield stress of as fabricated samples is approximately 410 MPa, about twice of the value reported of LPBF-

AM Cu-10Sn parts [126]. Inspiringly, the compression yield stress obtained in the present study is even slightly higher than the best properties reported (~399 MPa) [127], where Cu-10Sn samples were prepared by adjusting laser intensity. This reasons why the yield stress of AF sample is improved are summarized below. Laser energy density (E) can be described as the equation below [127],

$$E = \frac{P}{v \cdot h \cdot t} \tag{5-4}$$

where, v, h, t, and P represent laser scanning speed, hatch space, powder layer thickness, and laser power, respectively. Based on the equation above, the laser energy density of the present study, reference [126] and [127] were determined, which are 105.6 J/mm^3, 159.3 J/mm^3, and 220.0 J/mm^3, respectively. The reference [126] shows the medium laser energy density, therefore, the remarkably reduced yield stress in reference [126] is most likely due to the significantly increased Cu-10Sn powder size, which is ~85 μm compared with ~25.9 μm in the present study and ~60 μm in reference [127]. And more defects are expected in the sample investigated in reference [126] and degrade the mechanical performance. The slightly lower yield stress in reference [127] comparing with the as-fabricated sample is mainly due to the limited formation of δ phase the relatively larger grain size (5.1 ± 1.8 μm).

Cu-10Sn alloys were also reported fabricated and treated with several other fabrication and post treatment methods, for example hot press sintering (HPS) [274, 275], laser engineered net shaping (LENSTM) [128], equal channel angular pressing (ECAP) [273]. And the corresponding mechanical properties of the samples prepared with the above-mentioned methods are listed in Table 5.1, which are apparently smaller than that in this study. With a closer observation of the data, due to the significantly reduced grain size after severe plastic deformation [33], the samples treated with ECAP method possesses clearly higher yield stresses than the rest two methods (HPS, LENS^{TM}). However, it is worth noting that, the grain size in the sample after ECAP treatment is still not comparable with that of the as-fabricated

sample. LENS^{TM} process has the feature of considerably larger laser energy input than the LPBF process, which causes significantly larger melt pool size and greatly reduced cooling rate [230], and consequently obtaining larger grain sizes and deteriorating the grain boundary strengthening effect. It is even more severe for the HPS process, which possesses a much slower cooling rate (several tens of degrees per minutes [276]) than the LPBF process (over 10^4 °C/min [277]). In addition, it remains challenging to fully eliminate voids/pores inside the samples with the HPS treatment process, for example voids were reported existing around Cu3Sn precipitates [274], which deteriorate the overall mechanical performance of the samples. Ultimate stress and ductility of the samples are also listed in Table 5.1. With the preset testing strain limit of 25% in the present study, it is found that at the strain limit no sample failed, indicating superior ductility compared with that of the counterparts listed. The stress of the as-fabricated samples, and samples vacuum-annealed at 600 °C and 800 °C at the strain limit of 25% are 724.2 ± 13.8 MPa, 564.9 ± 12.6 MPa, and 426.6 ± 10.0 MPa, respectively. Again, the stress of the AF samples is greatly improved. The comparison above indicates that LPBF-AM is a promising technique to produce AM parts with excellent mechanical properties using the sample fabrication parameters applied in this chapter.

Besides, two other factors, namely the formation of two phase constituents (α-Cu (Sn) phase and fine (α+δ)-eutectoid phase) and the high dislocation density existing in the as-fabricated samples, are also responsible for contributing to the good mechanical properties of LPBF-AM Cu10Sn samples. According to the microstructures in Fig. 5.3, it is discovered that (α+δ)-eutectoid structures are distributed uniformly throughout the α-Cu (Sn) phase, and because of the extremely high cooling rate of the LPBF-AM process, (α+δ)-eutectoid structures in the as-fabricated samples are much smaller than that in cast counterparts. Similar with the grain boundary strengthening effect, the dispersed fine (α+δ)-eutectoid structure can increase the α/(α+δ)-eutectoid interfaces, which acts as barriers for the motion of dislocations, resulting

in the increase of mechanical strengths. Besides, due to the significant residual stress resulted from the thermal gradients and repeated heating and cooling cycles in the LPBF-AM process, a high dislocation density is usually induced. Previous studies have reported dislocation cell structures in LPBF-AM parts, e.g., LPBF-AM CM247LC Ni-based superalloy [278] and Cu-4.3Sn part [125], which further increase the mechanical strength of LPBF-AM parts.

5.3.3. Thermal conductivity evaluation

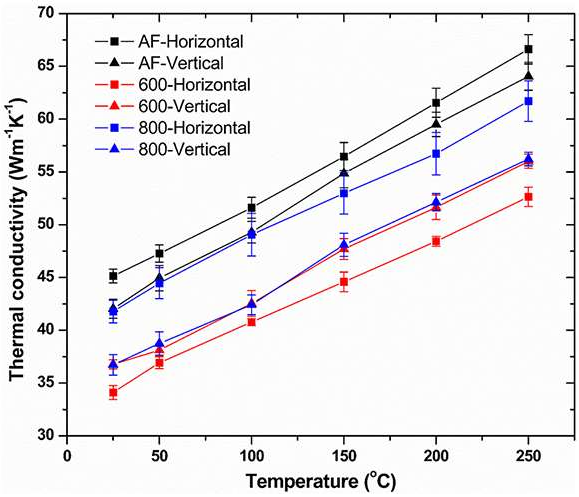

Figure 5.7. Thermal conductivity of both as-fabricated and vacuum-annealed samples vs. temperature.

The measured density values of the samples are listed in Table 5.2, which exhibit close values among all the samples. These density values together with the measured specific heat and thermal diffusivity were used to determine thermal conductivity, which is plotted in Fig. 5.7 versus testing temperatures. The error bars are also shown together with the thermal conductivity values, originated from averaging the thermal conductivity values of repeated tests. And the curves show qualitatively similar variation behaviors, i.e., as temperature rises from 25 ℃ to 250 ℃, thermal conductivity values increase almost linearly for all the samples. However, the AF-Horizontal and 800-Horizontal samples exhibit slightly higher thermal conductivity values than those of AF-Vertical and 800-Vertical samples, while the thermal conductivity of the 600-Horizontal sample is slightly higher than that of 600-Vertical sample.

It is worth noting that the thermal conductivity values of the as-fabricated samples are around 10% and over 20% higher that of the counterparts annealed at 800 ℃ and 600 ℃, respectively. And Table 5.1 shows the detailed thermal conductivity values. Through literature review, thermal conductivity of Cu-10Sn was only reported by Bhat et al. [128] before, who prepared the Cu-10Sn sample with LENS process, and the reported thermal conductivity is in accordance with the present study from 25 ℃ to 250 ℃.

Table 5.2. Densities of the samples measured by Archimedes principle

Sample name	Density (g/cm^3)
AF-Horizontal	8.85 ± 0.06
AF-Vertical	8.88 ± 0.01
600-Horizontal	8.87 ± 0.01
600-Vertical	8.86 ± 0.03
800-Horizontal	8.85 ± 0.02
800-Vertical	8.83 ± 0.04

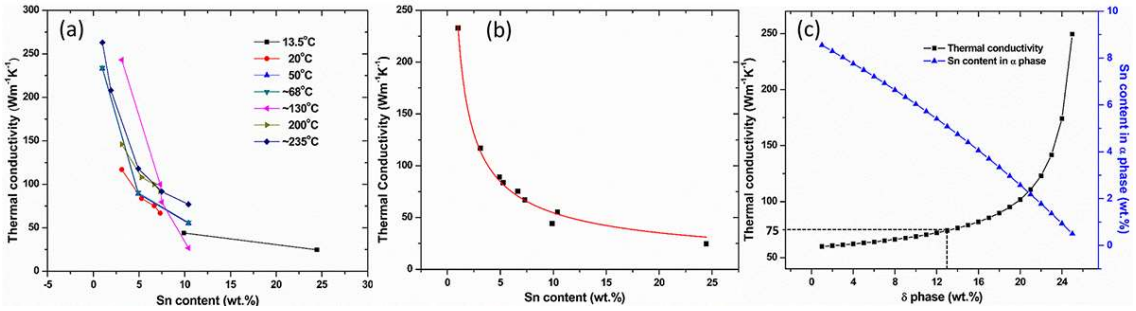

Figure 5.8. (a): Thermal conductivity of Cu-10Sn ally vs. Sn content at varying temperatures, all the data was researched from literature [279-281]; (b): thermal conductivity under 50 ℃ shown in Fig. 7(a) and a corresponding curve fitting; (c): The estimated thermal conductivity and Sn content in α phase as a function of δ phase fraction in the as-fabricated samples.

Thermal conductivity is composed of two main parts, i.e. lattice thermal conductivity and electronic thermal conductivity, with heat carriers of phonons and electrons, respectively. Pores in the samples can affect thermal conductivity [282], and in this study mainly by their sizes. According to previous studies, when the pore size was comparable with the mean free paths of phonons and electrons (~39 nm at 25 ℃ [283, 284]) or even smaller, thermal resistance was significantly increased due to the strong scattering between the heat carriers (electrons and

phonons) and the pores [282, 285]. Therefore, the as-fabricated samples should reduce thermal conductivity more effectively than the vacuum-annealed counterparts, owing to the remarkably smaller sizes in nano-scale (shown in Fig. 5.5). This observation, however, is contrary to the results obtained. Therefore, there must be another decisive factor influencing the thermal conductivity results.

Based on the XRD results (Fig. 5.2(a)), the vacuum-annealed samples only have single α phase, while the as-fabricated samples are made of two phases, a Sn-rich δ phase and a Cu-rich α phase. To discover the effect of the two-phase constituents on the thermal performance of the as-fabricated sample, literature review for the Cu-Sn alloys (as-cast or annealed state) was performed at temperatures below 50 ℃ vs. the Sn content [257, 280, 281]. And thermal conductivity values obtained are plotted in Fig. 5.8 (a), a least-squares fit to this data collection is also shown as the red curve, with the expression of

$$K = 233.37 \times (100 \times w_{Sn})^{-0.63} \tag{5-5}$$

where K and w_{Sn} are thermal conductivity and Sn content of the samples, respectively. Because the Cu-Sn alloys in the literature are in cast or annealed states, Equation (5-5) can be used to determine thermal conductivity of single-phase Cu-Sn alloys. The thermal conductivity (25.4 W/(m·K)) of the δ phase was estimated by extrapolating the fitted curve to the δ phase composition of 33.7 wt.% Sn. The thermal conductivity for the samples annealed at 600 ℃ and 800 ℃ are 61.5 W/(m·K) and 61.9 W/(m·K), respectively, for the Sn contents in them are 8.3 wt.% and 8.2 wt.%. Maxwell's equation was applied to calculate the thermal conductivity of the as-fabricated samples, which is described below [286],

$$\frac{K_{eff}}{K_m} = 1 + \frac{3\emptyset}{\frac{K_l + 2K_m}{K_l - K_m} - \emptyset} \tag{5-6}$$

where K_{eff}, K_m and K_l are the effective thermal conductivity of the as-fabricated Cu-Sn alloy, α phase, and δ phase, respectively (K_m was estimated from equation (5-5)), and ∅ represents the volume fraction of δ phase, which was determined with the expression below,

$$\emptyset = \frac{\frac{w_\delta}{\rho_\delta}}{\frac{w_\delta}{\rho_\delta}+\frac{w_\alpha}{\rho_\alpha}} \tag{5-7}$$

where, w_α and w_δ are the mass contents of α phase and δ phase, respectively, and $w_\alpha + w_\delta = 1$, while ρ_α, ρ_δ represent the densities of α phase and δ phase (8.68 g/cm^3 [287]). The equation below can be used to determine the density of α phase, when assuming the specific volumes of Cu and Sn stay constant after the diffusion of the latter into the former,

$$\rho_\alpha = V_{Cu} \times \rho_{Cu} + V_{Sn} \times \rho_{Sn} \tag{5-8}$$

where V_{Cu} and V_{Sn} are the volume fractions of Cu and Sn, respectively, and $V_{Cu} + V_{Sn} = 1$, while ρ_{Cu} and ρ_{Sn} stand for the densities of Cu (8.96 g/cm^3) and Sn (7.31 g/cm^3), respectively. The relation between the mass content of Sn, w_{Sn}, and the volume fraction of Sn, V_{Sn}, in α phase can be described as follows,

$$V_{Sn} = \frac{\frac{w_{Sn}}{\rho_{Sn}}}{\frac{w_{Sn}}{\rho_{Sn}}+\frac{w_{Cu}}{\rho_{Cu}}} \tag{5-9}$$

where w_{Cu} is the mass content of Cu in α phase, and $w_{Sn} + w_{Cu} = 1$. According to the characterization, Sn fraction in the as-fabricated samples is determined as 8.8 wt.%, and the relation between mass content of δ phase, w_δ, and w_{Sn} can then be described as

$$w_{Sn} = \frac{0.337 w_\delta - 0.088}{w_\delta - 1} \tag{5-10}$$

Combine all the equations above, it is obvious that the thermal conductivity of as-fabricated samples, K_{eff}, is also a functions of w_δ. The overall results are depicted in Fig. 5.8(b). Accordingly, when w_δ is 13 wt.%, K_{eff} is estimated to be 75 W/(m·K), around 20% higher than those of annealed samples. In addition, the calculated thermal conductivity is consistent with the experimental observations (Fig. 5.7). The reasons why the experimentally obtained thermal conductivity of the as-fabricated samples is higher than that of the vacuum-annealed samples are explained below. 1) The thermal conductivity of δ phase is significantly smaller than that of the α phase. 2) The as-fabricated samples contain both α and δ phases,

while the vacuum-annealed samples contain only the α phase. 3) The Sn content of α phase in the vacuum-annealed samples goes up as the δ phase is dissolved within the α phase, leading to a decrease in the thermal conductivity of α phase.

Thanks to the Rietveld refinement analysis of XRD results, w_δ is estimated to be 25.9%, K_{eff} would be even higher in which case. This observed discrepancy between the estimated and experimental thermal conductivity values of as-fabricated samples should be due to the existence of defects inside the samples, i.e. point defects, dislocations and grain boundaries, strongly scattering heat carriers and leading to declined thermal conductivity [288].

5.3.4. Corrosion performance

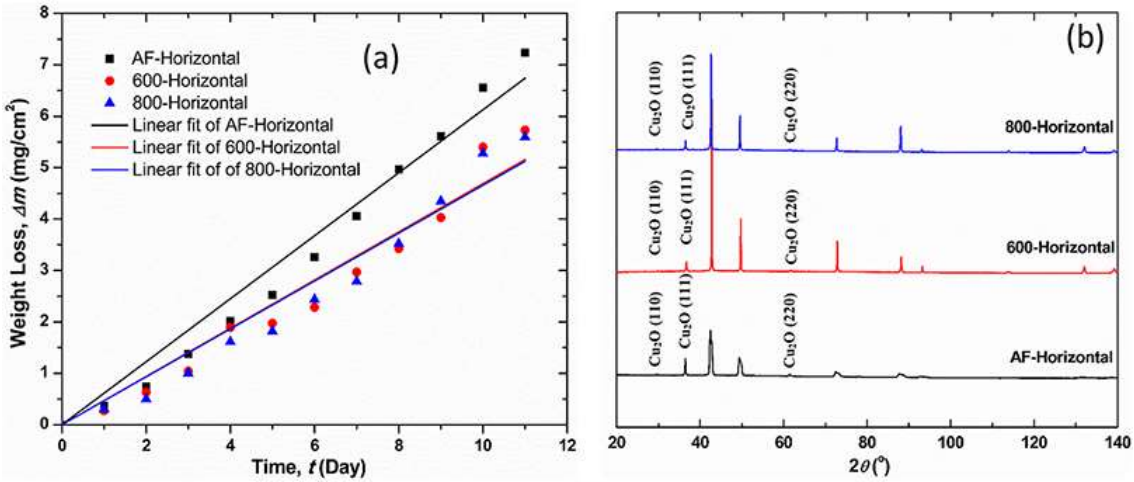

Figure 5.9. (a): Weight loss test results of samples in 3.5 wt% NaCl water solution with a duration of 11 days; (b): XRD patterns of the surfaces of samples after weight loss test, indicating the formation of Cu_2O phase.

Weight changes of the samples, namely AF-Horizontal, 600-Horizontal, and 800-Horizontal, in a NaCl water solution (3.5 wt. % concentration) were recorded daily for 11 consecutive days, and the results are exhibited in Fig. 5.9(a) and Table 5.3, which depict the relative corrosion rates. Obviously, the corrosion rate of as-fabricated samples is higher than that for the vacuum-annealed samples. Based on Fig. 5.9(a), both the vacuum annealed samples at 600 ℃ and 800 ℃ show quite similar curves. The θ-2θ XRD patterns of the as-fabricated and vacuum-annealed samples after weight loss testing are presented in Fig. 5.9(b). Cu_2O

phase are identified on all the sample surfaces. As shown in Fig. 5.2, the remaining peaks belong to the α and δ phase. The absence of chloride compounds on the surface after the immersion test confirms the formation of noble patina (type I) on the surface and low aggressive corrosive environmen.

Table 5.2. Slopes describing the weight loss rate of the samples immersing in the solution for 11 days

Sample	Slope ($mg/cm^2.day$)	R^2
AF-Horizontal	0.612	0.98
600-Horizontal	0.469	0.96
800-Horizontal	0.466	0.96

The change of sample surface potential as a function of time in an open circuit potential (OCP) test is shown in Fig. 5.10(a). Qualitatively, the curves are similar for all the three samples, due to dissolution of pre-formed compounds on the surfaces, the potential decreases for the first couple of hours, then increases because of the formation of a protective layer (Cu_2O), and finally achieves a steady state that is known as OCP. Minute fluctuations are observed on the curves, indicating dynamic the precipitation and dissolution process of the compounds resulted from the reaction process between the sample surfaces and the solution. Almost the identical curves are accquired for the two cacuum-annealed samples, same as weight loss results. However, compared with the vacuum-annealed sample (~ -0.155 V and 8 hours), the as-fabricated sample shows a more negative OCP value (~ -0.17 V) and a much longer time (30 hours) was needed for the surface to reach the steady state. By improving the passive layer quality and/or thickness, the heat treatment process has a stabilizing effect on the formed passive layer.

The potentiodynamic polarization testing results are summarized in Fig. 5.10(b) and Table 5.3. Little difference is seen for both vacuum-annealed samples (Fig. 5.10(b)), while the curve of as-fabricated sample shifts to lower potentials and higher current densities compared

to that of the vacuum annealed sample, demonstrating a more active surface of the as-fabricated sample. The corrosion current density of the as-fabricated sample is 7.586 μA/cm^2 (Table 5.3), which is more than two times of that of the 800-Horizontal sample (3.236 μA/cm^2). In accordance with the results obtained from weight loss and OCP tests, the corrosion rate for both vacuum-annealed samples are similar. Besides, in the potential range of -0.2 ~ -0.35V, all potentiodynamic curves show a region in the anodic branch with a constant current density. This phenomenon verifies the generation of a passive layer, mainly containing Cu_2O, as suggested by the XRD results (Fig. 5.9(b)).

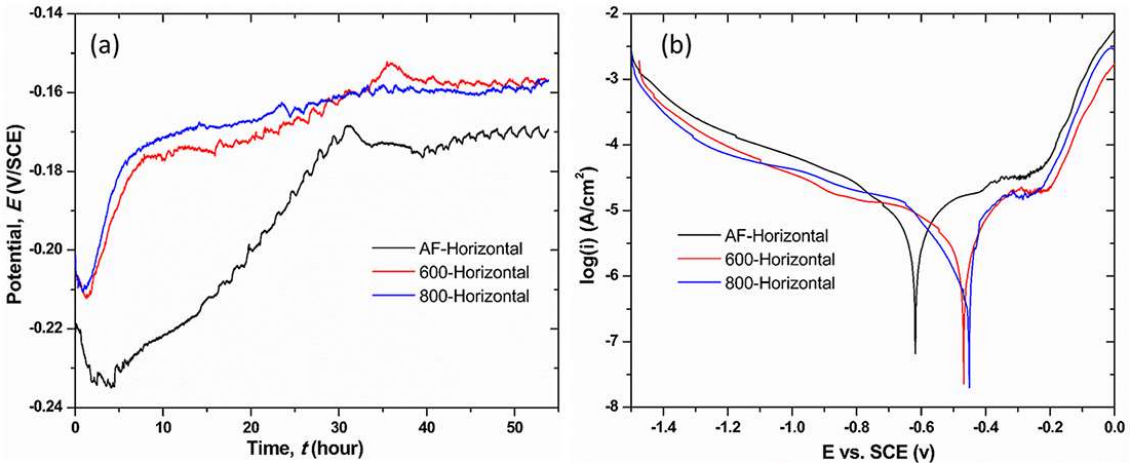

Figure 5.10. (a): Open circuit potential curves as a function of time in 3.5 wt.% NaCl water solution; (b): Potentiodynamic polarization test results of AF-Horizontal, 600-Horizontal and 800-Horizontal samples in 3.5 wt.% NaCl water solution.

Table 5.3. Detailed corrosion test results obtained from potentiodynamic polarization tests

Sample	E_{corr} (v)	i_{corr} (μA/cm^2)	i_p (μA/cm^2)	E_p (v)
AF-Horizontal	-0.620	7.586	31.623	-0.262
600-Horizontal	-0.468	3.388	21.380	-0.204
800-Horizontal	-0.451	3.236	16.218	-0.223

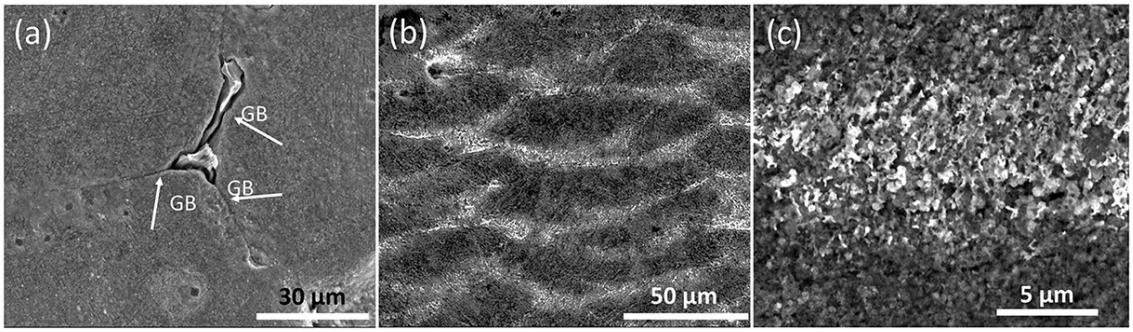

Figure 5.11. SEM images showing surface morphologies after weight loss test. (a): Intergranular corrosion on 800-Horizontal sample surface; (b)& (c): Galvanic corrosion on AF-Horizontal sample surface.

Intergranular corrosion attacks along grain boundaries (GBs) because of the higher energy state of GBs, which is a localized form of corrosion. Finer grains yield a higher GBs density, leading to a higher rate of intergranular corrosion rate [190, 289]. Besides, this passive layer can be less protective for samples with finer grains, because of the possible intervention of GBs in passive layer formation, which leads to a higher corrosion rate [290, 291]. Surface morphology of the 800-Horizontal sample after weight loss evaluation is shown in Fig. 5.11(a). Obviously, as indicated by the white arrows, intergranular corrosion attack occurred along grain boundaries. Galvanic corrosion is another reason for the higher corrosion rate of the as-fabricated sample, which is known occurred on a surface consisting of two phases in a corrosive media, with more resistive phase serves as cathode and causes the corrosion of the other phase [292]. The as-fabricated samples contain both α and δ phases, while only the α phase is contained in the vacuum annealed sample. It has been reported that δ phase shows a superior corrosion performance than the α phase [123, 261]. Therefore, preferential corrosion attacks on the α phase and the δ phase works as a cathode. The surface morphology of the as-fabricated sample after corrosion test is shown in Fig. 5.11(b). According to Fig. 5.11(c), melt pool profiles are seen with the white structures mainly distributed on the melt pool borders, which protrude out of the sample surface, similar with etched microstructures (Fig. 5.3(d)). Therefore,

the above observations can be attributed to galvanic corrosion resulted from the co-existence of α and δ phases.

5.4. Conclusions

LPBF-AM method was used successfully to make Cu-10Sn alloy samples. The influence of buliding orientations and heat treatment condictions on mechanical, thermal, and corrosion properties of Cu-10Sn alloy samples were investigated with the conclusions below.

(1) The as-fabricated samples show small grain size (~2 μm), and two-phase constituents, a Cu-rich α phase and a Sn-rich δ phase, owing to the extremely fast cooling rate of LPBF-AM process. Meanwhile, vacuum-annealed samples contain only α phase and exhibit equiaxed grains with increased sizes.

(2) Building orientations (perpendicular/vertical to the building orientation) are discovered to have minimum influence on the compression strength, thermal conductivity, and corrosion properties of the as-fabricated samples.

(3) Due to the existence of phase interfaces, smaller grain size, and high dislocation density, the as-fabricated samples show a much increased compression strength than that of the vacuum-annealed samples.

(4) Thermal conductivity of the as-fabricated samples is ~10% and over 20% higher than that of the samples annealed at 800 ℃ and 600 ℃, respectively, which is mainly due to the two-phase constituents.

(5) Due to the modification of passive layer morphology and the decrease of the susceptibility to internal galvanic corrosion and intergranular corrosion, heat treatment shows a substantial enhancement in corrosion property by reducing the corrosion rate by almost 50%.

Chapter 6. Thermal and Mechanical Properties of Additively Manufactured Cu-1.5Cr-0.5Zr Alloy Samples

6.1. Introduction

NASA and aerospace industry partners are exploring metal additive manufacturing methods for manufacturing liquid rocket engine components in order to reduce overall mission costs. One of the primary technologies of interest is Laser Powder Bed Fusion (L-PBF), which has beem applied by NASA and aerospace industry partners for making monolithic copper combustion chambers aimed at establishing a long-term supply chain [129, 130]. Metallic 3D parts are fabricated sussesstively and selectively melting thin powder layers according to CAD-directed laser scanning strategies during the L-PBF process. In which case, desired 2D section shapes are formed with multiple laser line scans (molten tracks), and similar repeated cycles generate complex 3D metal/alloy parts. L-PBF is an ideal tool to fabricate parts with complex shapes as the laser molten tracks are about 25 to 50 μm in depth and 50 to 100 μm in width, i.e. regeneratively-cooled combustion nozzles and chambers, cotaining internal coolant channels. However, as-fabricated L-PBF parts are believed to have unique thermal and mechanical properties because of the extremely fast melting and cooling rate of those fine laser tracks.

Copper-alloy C-18150 is a CuCrZr alloy, which is a precipitation-hardened alloy. Due to the high conductivity and high strength, CuCrZr alloys have been considered as the primary candidate for the heat sink material of the International Thermonuclear Experimental Reactor (ITER) first wall [293]. Conventional fabrication method was used for making CuCrZr alloy parts, and the mechanical/physical properties and heat treatment processes have been studied extensively [294-302]. Dur to the superior performance, NASA is evaluating C-18150 for the application of additive manufacturing of regeneratively-cooled combustion nozzles and chambers. The hotwall side of the regeneratively-cooled liquid rocket engine chambers is subjected to the high temperature combustion gas, while the opposite wall flows cryogenic or

heated propellants to help to cool the hotwall. Due to the severe service environments, the alloys qualified for the application of regeneratively-cooled rocket engine must possess high thermal conductivity, high strength, and resistance to low cycle fatigue and creep. The microstructures and phases formed during the fabrication processes show strong effects on the physical/mechanical properties. Unfortunately, limited research has been performed to investigate the thermal and mechanical properties of C-18150 L-PBF parts (especially for high-temperature situations). To fill this knowledge gap, the above-mentioned properties was investigated in this chapter. This study focused on high-temperature thermal and mechanical performances to mimic the real application conditions. And this study discussed the relations between the phases/microstructures and the thermal/mechanical properties.

6.2. Materials and methods

6.2.1 Samples and aging treatments

In this chapter, cylindrical shaped Cu-1.5Cr-0.5Zr parts was used, which was made with L-PBF method (with the size of Φ12.7mm × 76.2/101.6 mm), provided by NASA. Three different orientations were used to fabricate the samples (shown in Fig. 6.1), i.e. namely vertical, angled, and horizontal to the building direction. To distinguish the samples easily, in the remainder of the chapter, the samples built horizontal, vertical, and angled to the building direction are denoted as Horizontal, Angled and Vertical, respectively. The central axes of the Angled samples has an angle of 45° relative to the building direction, while Vertical and Horizontal are parallel and perpendicular to the building direction, respectively.

A Neytech Vulcan 3-550 Dental Furnace (air atmosphere) was used to perform heat treatment on the Vertical samples to investigate the effect of the heat treatment temperatures. Stainless steel foils were used to tightly wrap the samples to minimize the effect of oxidation during the heat treatment. Four aging temperatures, namely 420 °C, 500 °C, 575 °C, and 650 °C, were set as the target temperatures. During the aging treatment process, the samples were first

heated to the temperatures, with a heating rate of 10 °C/min. After holding the temperatures for 2 hours, the samples were cooled within the furnace. And the programmed aging treatment temperature profiles are shown in Fig. 6.2.

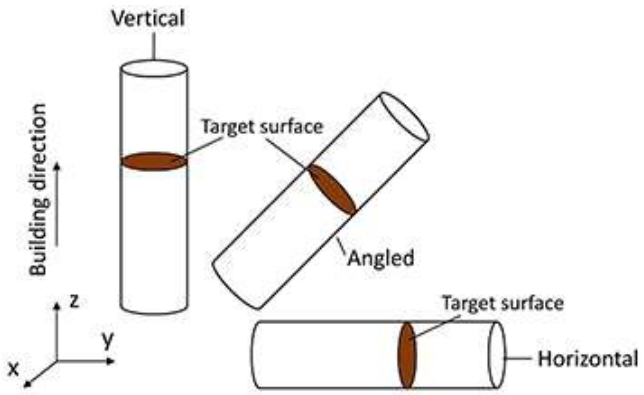

Figure 6.1. Schematic image showing the orientations of the L-PBF samples.

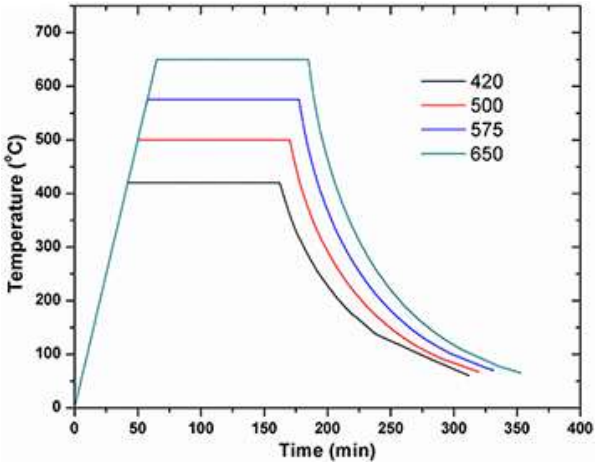

Figure 6.2. Temperature profiles of the aging processes.

6.2.2 Tensile and hardness tests

An MTS Alliance RF/100 tester (equipped with an MTS 653 furnace) was used to investigate the high-temperature tensile performance. To enable the tensile test setup shown in Fig. 6.3, a set of custom designed gripers was made of Alloy-X using a wire EDM machine with matching sample shoulder profiles. The tests were conducted at three different temperatures, namely room temperature, 204 °C (400 °F), and 427 °C (800 °F). The samples were heated up to the temperatures with a heating rate of 100 °C/min, after soaking for 8 min,

the tests were performed with a fixed strain rate of $8.3x10^{-4}$ /s based on the crosshead speed, followed by the cooling process to room temperature. For the credibility of the testing results, two or three samples were tested for each fabication and heat treatment condition.

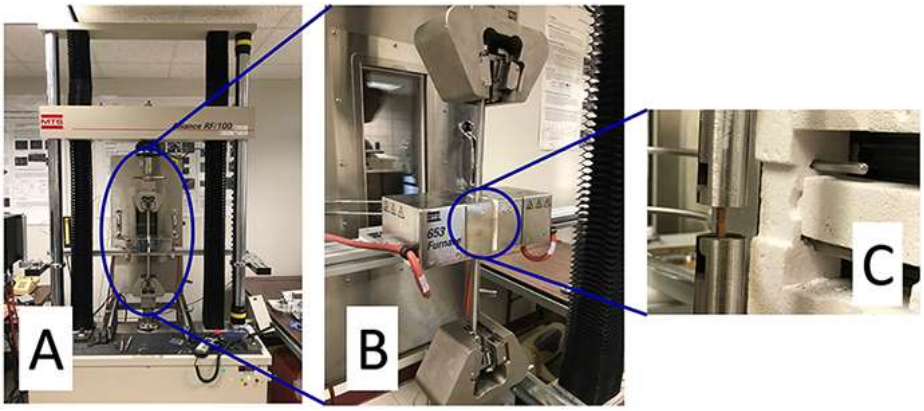

Figure 6.3. Images indicating the high-temperature tensile test setup.

A Clark Microhardness tester (model CM-802AT) was used to perform hardness testing at room temperature, with a testing load of 1000 g and dwell time of 15 secs. Before the tests, the sample surfaces were ground with SiC papers, up to 1200 mesh, and polished with MetaDiTM Supereme polycrystalline diamond suspension (1 μm) to a mirror finish. After polishing, the samples were rinsed with distilled water and dried in air. Five hardness tests were performed at differing spots for each sample to ensure the repeatability of the results.

6.2.3. Thermal conductivity tests

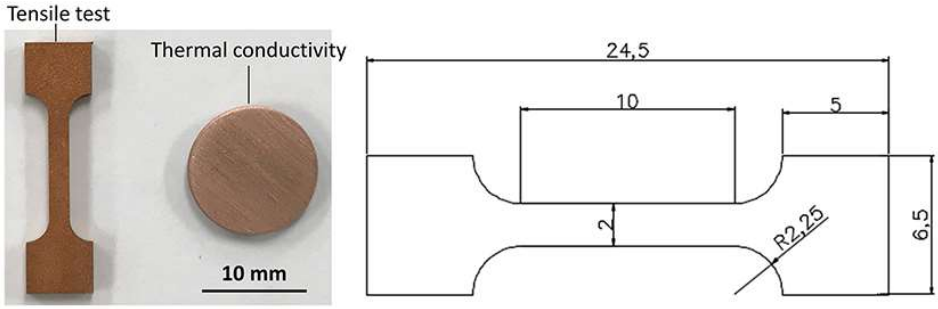

Figure 6.4. Images showing the shapes and sizes of samples (left) and the detailed geometry of the tensile testing sample (right, with the unit mm).

A Netzsch LFA 467 HT HyperFlash®- light flash apparatus was used to perform the thermal property measurements, with the sample size of Φ12.55×2.50 mm. Prior to the tests,

the surfaces of the samples were ground with SiC papers, 320, 600 grit, successively, to remove the surface contamination. To ensure the same heat absorption, the surfaces of both the target samples and the reference sample were sprayed with a uniform thin graphite layer. The thermal diffusivity, α, was directly measured by the LFA 467 device from 25 ℃ to 1000 ℃, with a heating rate of 25 ℃/min, and the samples dwell at each testing temperature (except room temperature) for ~30 min. The specific heat, C_p, was calculated using a reference sample. Again, for the credibility of the testing results, at least three measurements were performed at each measuring temperature. And the detailed thermal property testing was described in Chapter 5. The shapes and sizes of the testing samples are shown in Fig. 6.4 (left), and the detailed size of the tensile testing samples are exhibited in Fig. 6.4 (Right).

6.2.4. Sample characterization

The phase transformation temperatures of different phases were pinpointed with high temperature differential scanning calorimeter (DSC) using alumina pans (Model DSC 404 F1 Pegasus, NETZSCH Group, Germany). A baseline test was conducted and recorded using two empty pans under the same experimental conditions as would be used later for sample testing before each measurement.

During the DSC testing, a small piece of sample was loaded into the pan, then placed into the DSC chamber, and finally two consecutive thermal circles (from room temperature to 1075°C /1120 °C) were performed. The temperature ramp was maintained at a typical rate 10 °C/min and argon gas was used as both purging and protective gas flowing at 20 ml/min [303]. Scanning electron microscope (SEM) instrument was utilized for microstructural examination. The targeted testing surfaces for SEM and XRD tests are indicated as the shaded areas in Fig. 6.1. Before the microstructure characterization, the sample surfaces were mechanically ground and polished to a mirror finish, followed by an etching procedure with a solution (mixture of 5 g $FeCl_3$, 10 ml HCl, and 100 ml deionized water) at room temperature

for 15 seconds. Energy dispersive spectroscopy (EDS) was used to evaluate the elemental distribution in the sample. Phase identification was conducted using X-ray diffraction (XRD) from 20° to 110° with a scanning step size of 0.026°.

6.3. Results and discussions

6.3.1 Phases of the Cu-1.5Cr-0.5Zr alloy

CALculation of PHAse Diagrams (CALPHAD) calculations were carried out using the ThermoCalc software package with the TCCU3 database to guide the design of the heat treatment process [304], which provides the information about the formation of precipitates and the solidification process at different temperatures (Fig. 6.5). According to the CALPHAD calculations, the dominant phase is the copper phase at room temperature. And at high temperatures, the precipitates are found to include Cr, Cu51Zr14, and Cr2Zr, however, with the amount less than 2%. This result is in accordance with the mass amounts of Cr and Zr addition in the sample. The liquidus and solidus temperatures are 1073 °C and 949 °C, respectively. At 630 °C, Cu51Zr14 transforms into Cu2Zr, which is a precipitant phase in Cu-1.5Cr-0.5Zr alloy.

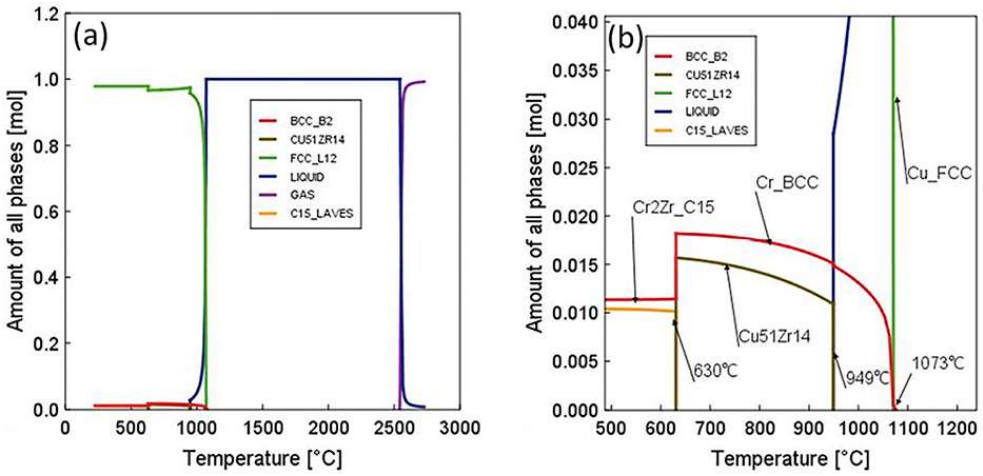

Figure 6.5. Images showing the CALPHAD study results of Cu-1.5Cr-0.5Zr alloy. (a) Full range calculation results, (b) minor phases.

Based on the Thermo-Calc calculations, the melting point the Cu-1.5Cr-0.5Zr alloy was determined as 1073 °C. Therefore, the first set of DSC test was conducted on the Angled

sample was from room temperature to 1075 °C (Fig. 6(a)). However, no melting peaks are observed within this period of temperatur. Therefore, the maximum temperature was increased to 1120 °C for the remaining tests. And the obtained melting temperatures are 1102 °C and 1103 °C, respectively, in Figs. 6.6(b) and 6.6(c), which is slightly higher than the melting point 1073 °C by the Thermo-Calc prediction. The difference between the DSC furnace and the sample in the transient heating process should be the reason of the phenomenon.

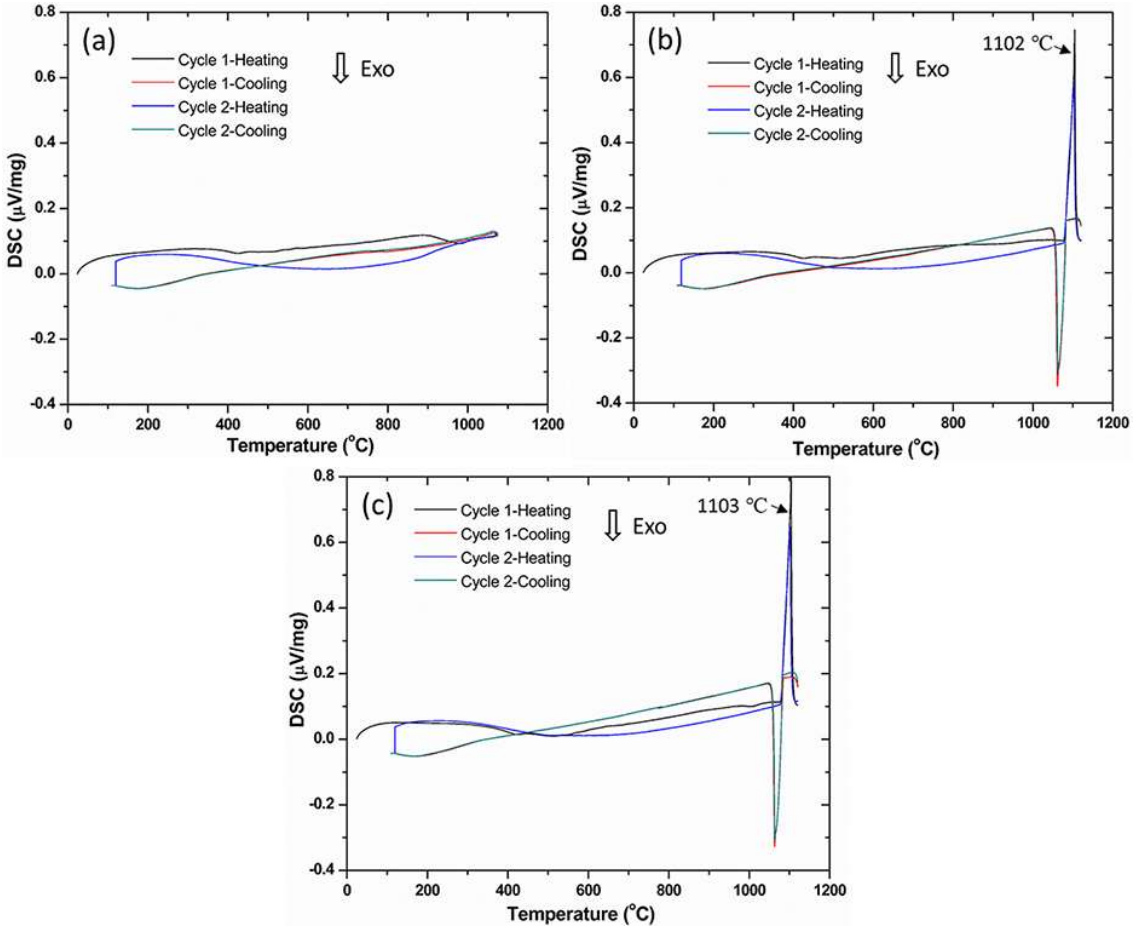

Figure 6.6. Images showing the DSC testing results of samples with differing orientations, (a) 25-1075 °C Angled, (b) 25-1120 °C Vertical, and (c) 25-1120 °C Horizontal.

According to the Thermo-Calc results, due to the limited amounts of secondary phases, only the melting and solidification peaks of copper phase can be detected. For all three as-fabricated samples (Angled, Vertical, and Horizontal), the DSC curve of the first heating cycle is different from that the second heating process. Based on Fig. 6, the two curves deviate from

each other at around 250 °C and merge together at a high temperature close to the melting point of copper. By comparing the two sets of curves, the first heating cycle is related to the crystallization (nucleation and precipitation) of precipitates from the supersaturated Cu-1.5Cr-0.5Zr L-PBF samples, which was found to be an endothermic process (Fig. 6.6). Besides, three consecutive thermal cycles from room temperature to 1120 °C were conducted on the Vertical sample, to further confirm the endothermic process associated with the crystallization (nucleation and precipitation) of precipitates, which is shown in Fig. 7 (top). At the same time, it is found that the cooling curves perfectly overlap one another with three consecutive DSC thermal circles, which indicates that the crystallization of precipitates from the supersaturated as-fabeicated parts was completed in the first heating process.

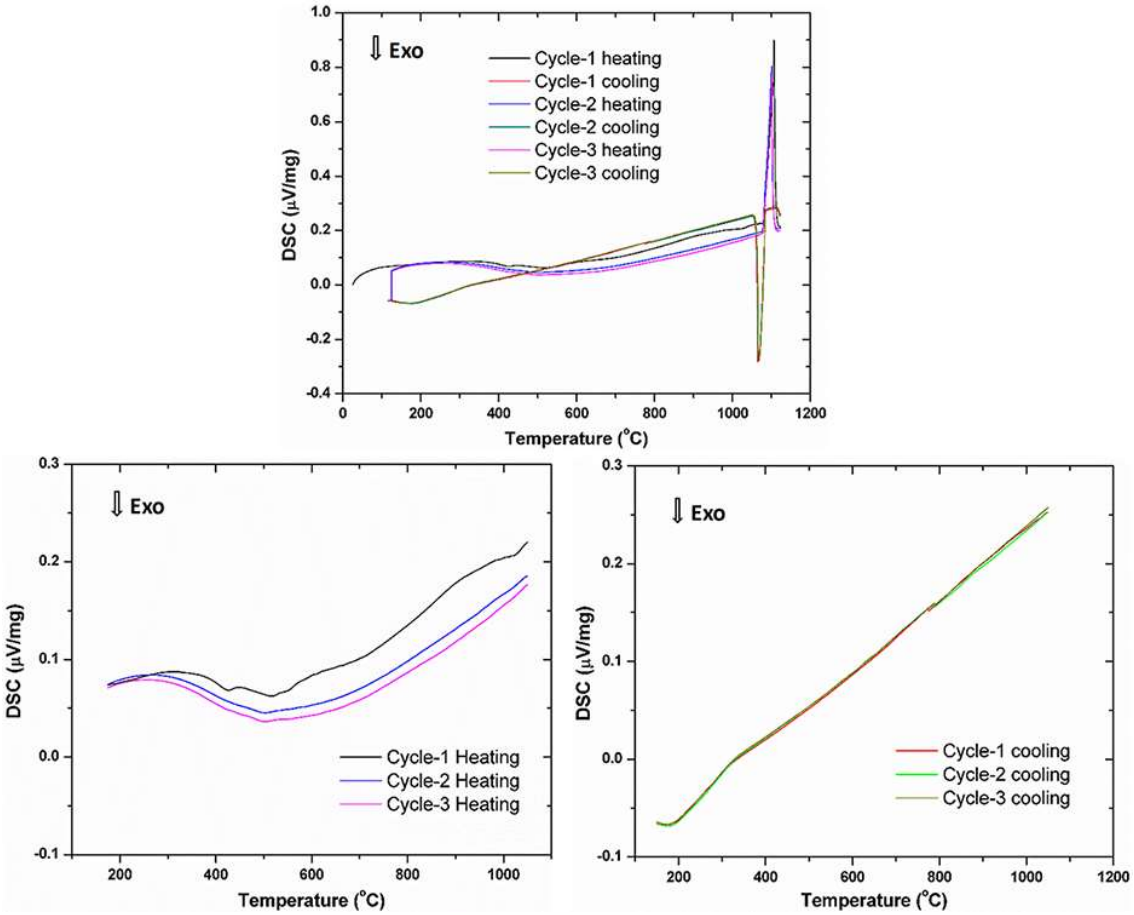

Figure 6.7. Images indicating three consecutive DSC heating and cooling thermal cycles on Vertical sample.

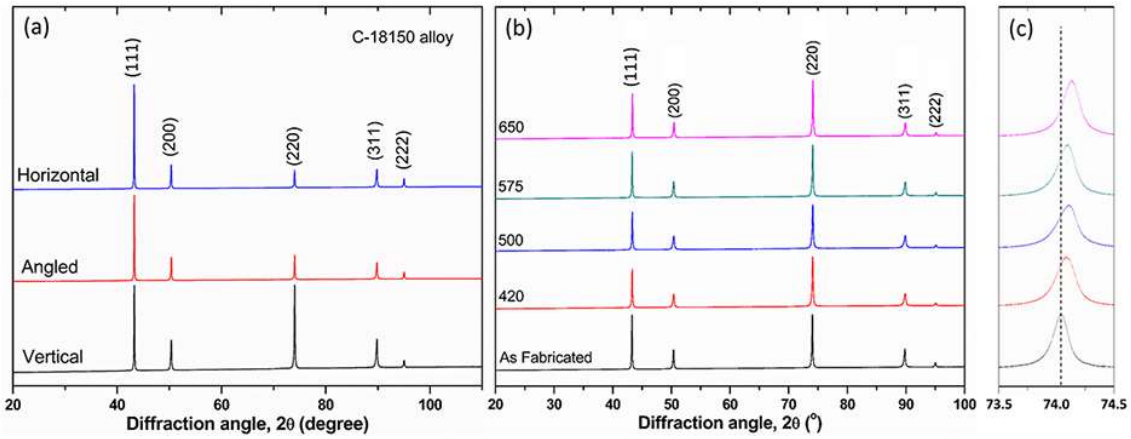

Figure 6.8. Images showing XRD test results of the samples. (a) samples with different building orientations. (b) samples aged at varying temperatures. (c) diffraction angles of the samples over a narrow angle range.

The XRD results of the samples are exhibited in Fig. 6.8. Clearly, the dominant phase is FCC copper phase. Meanwhile, when the sample orientation changes from horizontal to vertical, the copper (220) peak gradually becomes stronger, which indicates preferential grain orientation of copper (220) on the target surface. Figure 6.9 verifies this phenomenon, where columnar grains grow towards the center of the molten tracks along the thermal gradient direction, causing the grain anisotropy, which is expected to cause varied mechanical performance. Figures 8(b)(c) illustrate the XRD results performed on the samples both before and after aging treatments, which, again, reveal the main peaks to be the copper phase. With the increase of aging temperature, the diffraction peaks shift slightly towards the larger diffraction angle side, with the help of Bragg's equation, this phenomenon indicates the decrease of interplanar spacing, correspondingly the decrease of lattice parameter. This observation can be explained by the chromium solution atoms decomposing from copper matrix and forming precipitates. As the aging temperature increases, more and more chromium atoms decompose from the matrix and form precipitates. Considering the copper matrix is cubic structure, the lattice parameter decreases from 3.619 Å to 3.615 Å when it increases from room temerature to 650 ℃.

6.3.2 Microstructures of the C-18150 alloy

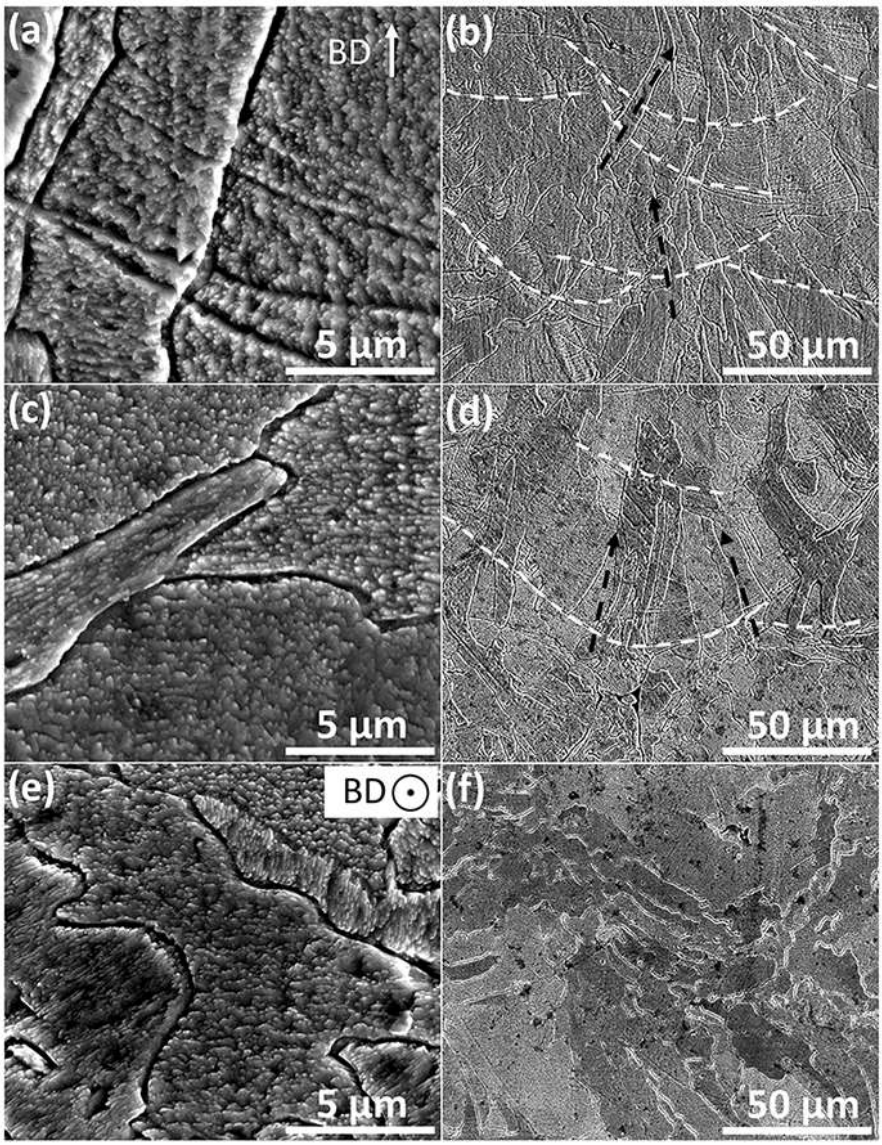

Figure 6.9. Microstructures of Cu-1.5Cr-0.5Zr alloy samples with differing orientations and magnifications. (a)(b) Horizontal sample. (c)(d) Angled sample. (e)(f) Vertical sample.

The microstructures of Vertical, Horizontal, and Angled samples are shown in Fig. 6.9. Obviously, layer-by-layer AM structures are observed in both Horizontal and Angled samples, and the melt pool boundaries are marked with dashed curves in Fig. 6.9, with the solidification directions indicated by black dash arrows. Besides, with the orientation preferentially along the thermal gradient direction columnar grains grow through several fabrication layers, pointing to the center of the molt pool. Metastable microstructures with a size less than 1 μm are also

observed, together with the columnar structures (with a width of several microns and a length of several tens of microns). Obvious, hierarchical structures are generated in the as fabricated samples, which are originated from the fast cooling rates and complex temperature gradients during the L-PBF process.

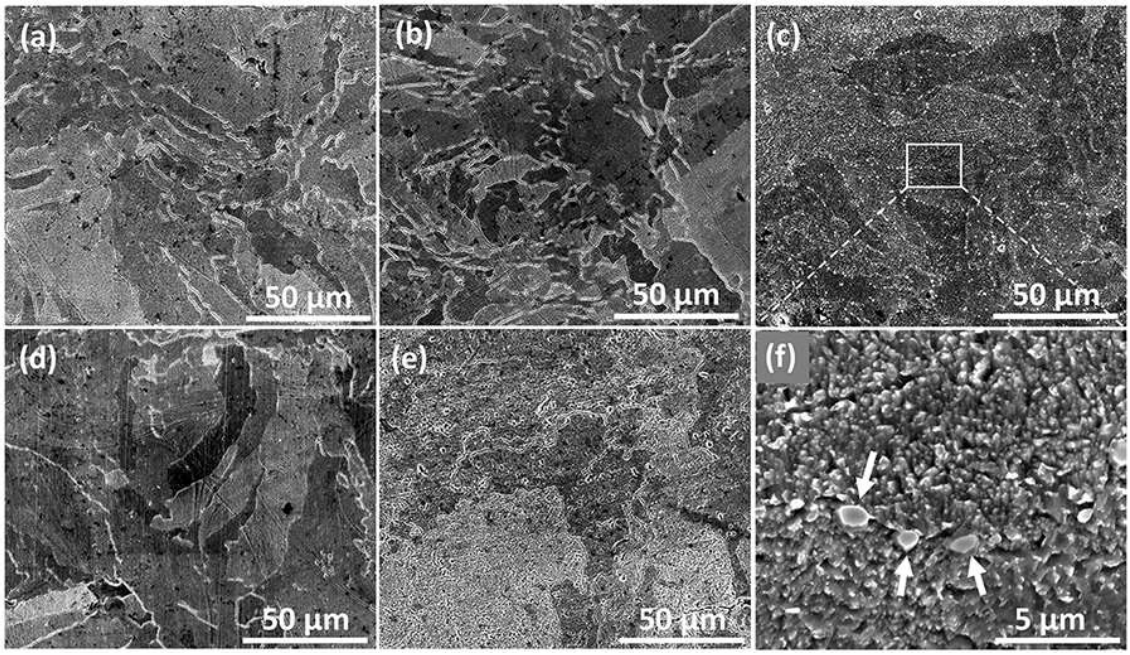

Figure 6.10. Microstrures of as-fabricated Vertical sample (a), and the Vertical samples aged at (b) 420 ℃, (c) 500 ℃, (d) 575 ℃, and (e) 650 ℃, respectively. (f) illustrates the microstructures of the Vertical sample aged at 500 ℃ with a larger magnification; the precipitates are indicated by the white arrows.

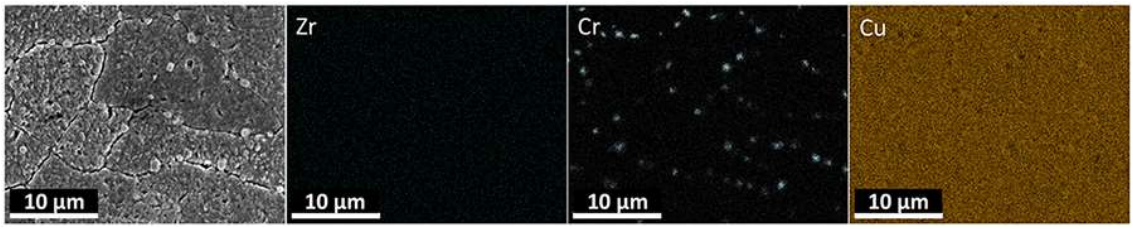

Figure 6.11. Images showing the composition distribution results investigated with EDS mapping of the sample aged at 500 ℃ for 2 hours.

For the widely accpted heat treatment strategy, water quenching is used to obtain supersaturated solid solution state [295]. Intrestingly, the as-fabricated samples are also in the supersaturated solid solution state after the L-PBF process, resulting from both the low solubility of chromium in copper matrix and the extremely fast cooling rate, leading to

quenching effect [101, 305, 306]. In view of this, direct aging treatment were performed on the samples. According to Fig. 6.10(a) to (e), substantial grain growth was observed with the increase of aging temperature, which indicates the occurance of recrystallization of the samples after aging treatment. Precipitates are visible along the grain boundaries (Fig. 10(f)), after aging at 500 ℃ for 2 hours with the grain size of several hundred nanometers. Elemental composition distribution information was investigated with EDS mapping, and the results are shown in Fig. 11, which reveal that the precipitates are mainly the enrichment of chromium. Similar results were also reported previously [116].

6.3.3 Thermal conductivity

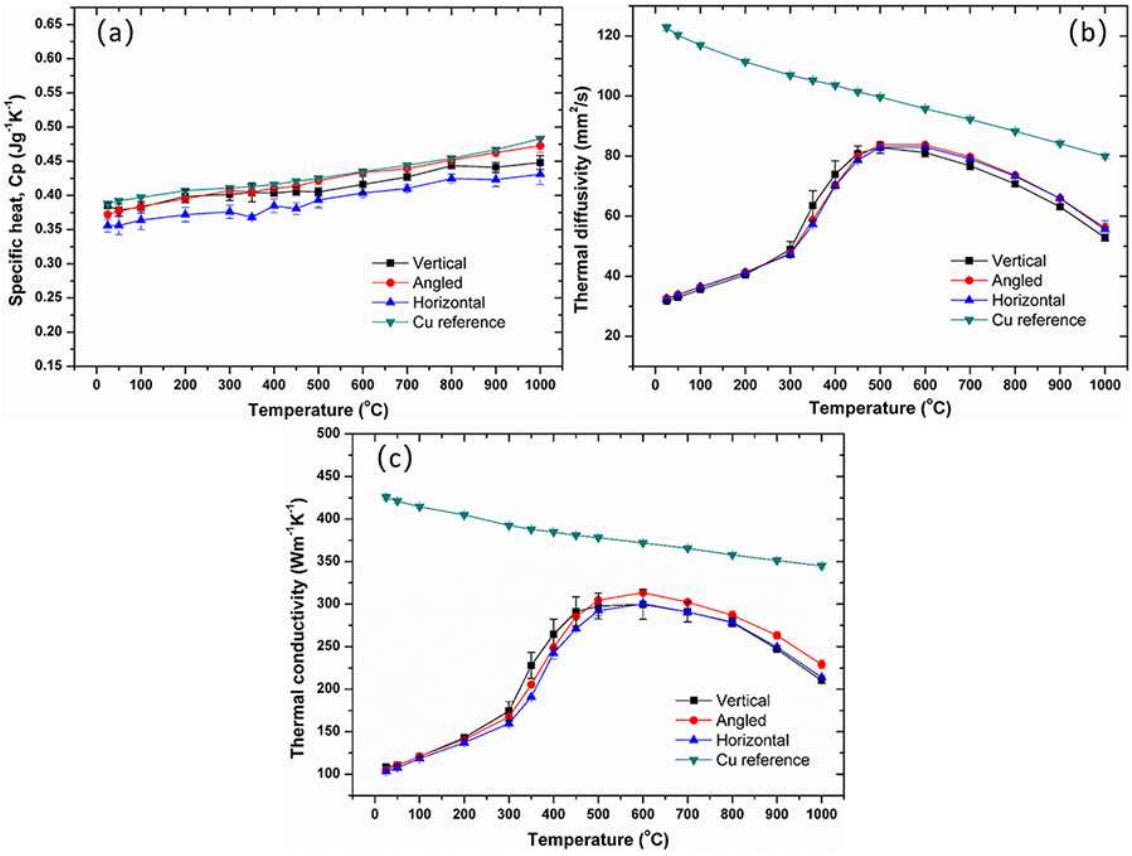

Figure 6.12. Images showing the thermal properties of the L-PBF AM Vertical, Angled, and Horizontal samples, together with a pure copper reference sample for the first-cycle testing. (a), (b) and (c) show the variation behaviors of specific heat, thermal diffusivity and thermal conductivity as a function of temperature, respectively.

Densities of the samples were evaluated with the Archimedes principle before the light flash testing, the results of which are listed in Table 6.1. The Vertical and Horizontal samples show almost the same densities, while the Angled sample possesses a little bit samller density value. Figure 12(a) illustrates the specific heat of the samples, which, qualitatively, increases monotonically with the increase of the testing temperatures, which is in accordance with previous studies [307]. By comparison, the specific heat values of the Vertical and Angled samples are approximately 7 % larger than that of the Horizontal sample. Thermal diffusivity of the as-fabricated AM samples are shown in Fig. 6.12(b), which obviously increases as the testing temperature increases from room temperature to 500 ℃, then declines as it goes up to 1000 ℃. With a closer observation, the period from room temperature to 500 ℃ can be divided into two stages, the slow increasing stage (room temperature to 300 ℃) and a rapid increasing stage (from 300-500 ℃).

From room temperature to 1000 ℃, marginal changes are observed for densities and specific heats of the samples. To be specific, specific heat increases by only approximately 20 %. However, the change in thermal diffusivity is about three times for the as-fabricated samples. Evidently, thermal diffusivity is the dominant factor of thermal conductivity, and these two parameters shows similar variation behaviors. Besides, even though grain anisotropy exists, negligible difference are observed for the thermal conductivity between the samples, indicating thermal conductivity is a grain orientation insensitive property. From room temperautre to 300 ℃, thermal conductivity increases from ~105 to ~165 W/(m·K) with a relatively slow increasing rate, then rapidly increases to ~300 W/(m·K) when reaching 500 ℃, finally declines to approximately 220 W/(m·K) when it increases to 1000 ℃. The reason of the thermal diffusivity/conductivity variation can be explained below.

For solid materials, heat is transferred by heat carriers, mainly phonons (lattice vibrations) and free electrons [308], hence thermal conductivity (λ) can be expressed as below [309]:

$$\lambda = \lambda_e + \lambda_p \tag{6-1}$$

where λ_e and λ_p indicate electronic thermal conductivity and lattice thermal conductivity, respectively. Electronic thermal conductivity is closely related to electrical resistivity, based on the Wiedeman-Franz law [310]:

$$\lambda_e = LT/\rho \tag{6-2}$$

where T, L, and ρ represent the absolute temperature, Lorenz number, and electrical resistivity, respectively. Electrical resistivity depends on both temperature and solute atoms, which can be described by the Matthiessen's law [111]:

$$\rho = \rho_{\text{pure}}(T) + \sum_i \rho_i C_i \tag{6-3}$$

whereC_i, ρ_i, and $\rho_{\text{pure}}(T)$ are the specific electrical resistivity, relative content of the alloying element i, and temperature dependent electrical resistivity of the base metal, respectively. Hence thermal conductivity of a solid material can be estimated by equation (4):

$$\lambda = \frac{LT}{\rho_{\text{pure}}(T) + \sum_i \rho_i C_i\ (3)} + \lambda_p \tag{6-4}$$

Heat is mainly transferred by electrons in metals [311]. As C-18150 is a Cu alloy with dilute Cr/Zr addtions, based on expression (6-4), tiny amount of solute atoms would significantly increase electrical resistivity and dramatically decrease thermal diffusivity/conductivity [110, 112, 312, 313].

Thermal properties were evaluated at high temperatures, and the testing process can be treated as the dynamic heat treatment process of the samples. At high testing temperatures, the supersaturated chromium solution atoms decompose form the copper matrix, then diffuse and generate precipitates, which decreases the solid solution atoms in the matrix, leading to less scattering of heat carriers, beneficial for the increase of thermal conductivity of the samples.

Besides, aging temperature and aging time shows significant effects on the precipitation process [101, 314]. Insufficient energy was provided at low temperatures (below 300 ℃) to decompose the solid solutes to form precipitates, and slow precipitation kinetics were achieved. However, as the testing temperature increases (from 300 ℃ to 500 ℃), more energy were supplied to accelerate the precipitation process, rapidly increasing the thermal conductivity of the sample. From 500 ℃ to 600 ℃, slight thermal conductivity increase is also seen with a clearly slower increasing rate. Most of the Cr/Zr solution atoms already formed precipitates at the testing temperature of 500 ℃, and only a small amount of the Cr remained to form precipitates. And when it reaches 600 ℃, almost all the solution atoms transform to precipitates. Interestingly, over 600 ℃, thermal conductivity of the Cu-1.5Cr-0.5Zr alloy samples show similar variation behavior with that of the pure copper reference sample, which decreases monotonically with the increase of temperature, revealing that almost all the chromium atoms have formed precipitates. At this point, electron-phonon interaction becomes dominant, and the thermal resitance caused by this interaction rises as temperature goes up [308]. Therefore, a decrease of thermal diffusivity/conductivity is observed. Meanwhile, thermal conductivity of the samples decline faster than that of the pure copper reference, most likely due to the over aging effect that leads to non-coherency between the matrix and the precipitates, which introduces more thermal resistance into the sample.

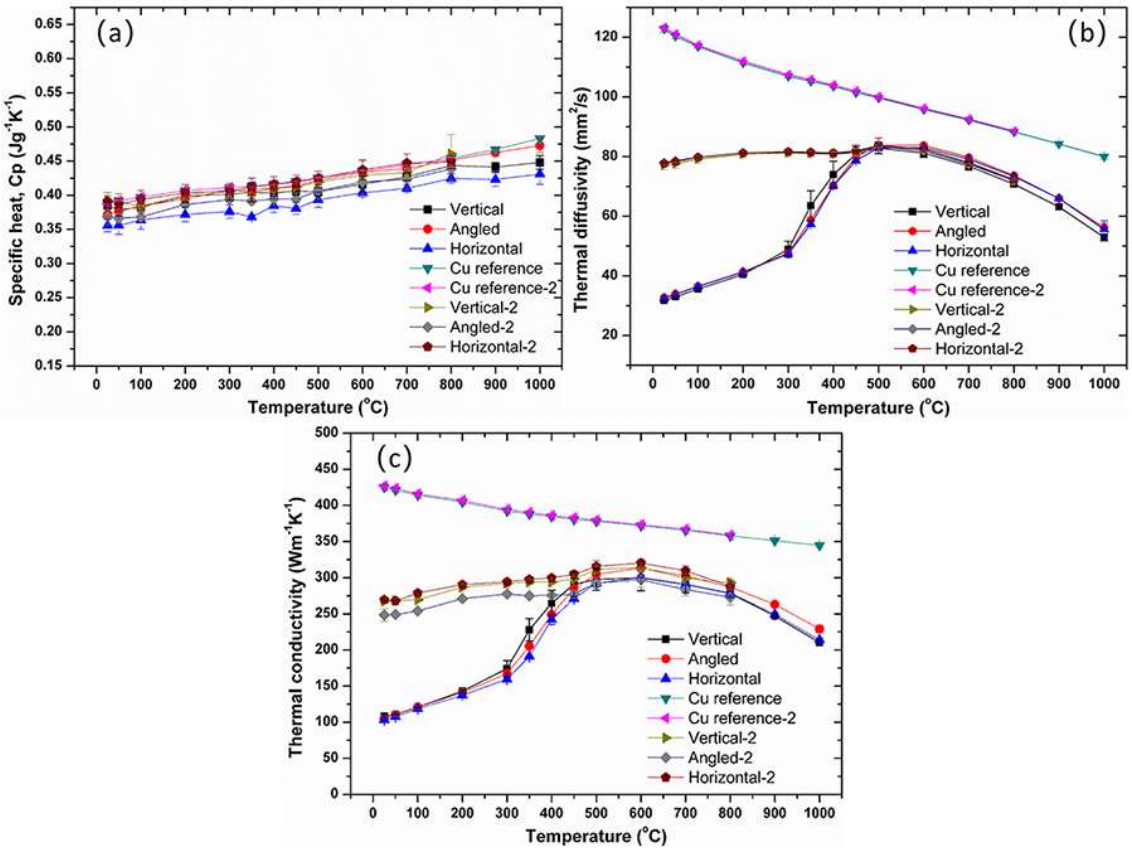

Figure 6.13. Images indicating the repeated tests of thermal properties of the as-fabricated samples with vertical, angled, and horizontal building orientations and a pure copper reference sample. (a), (b) and (c) exhibit the variation behaviors of specific heat, thermal diffusivity, and thermal conductivity versus testing temperature, respectively.

The variation behaviors of thermal diffusivity and thermal conductivity are quite unusual (as-fabricated samples). Therefore, the testing cycle was repeated a second time to discover the reasons. The thermal property testing process, with temperautres varying from room temperature to 1000 ℃, can be treated as a heat treatment process itself. As shwon in Fig. 13, the repeated tests show clear impacts on the thermal performace of the L-PBF samples. However, above 600 ℃, thermal conductivity of the two cycles overlap each other, indicating that complete decomposition of chromium from the copper matrix can be achieved when the testing temperature reaches 600 ℃. The decomposition and precipitation effect is negligible as the temperature further increases.

Based on the discovery above, thermal property can be effectively tuned with heat treatments on the as-fabricated samples. Therefore, aging treatment was conducted. After the aging processes under 420 ℃, 500 ℃, 575 ℃, and 650 ℃ for 2 hours, thermal property measurements were evaluated again from room temperature to 1000 ℃. At low testing temperatures (below 600 ℃), thermal conductivity increases with the increase of aging temperature, while over 600 ℃ negligible difference is seen. To be specific, thermal diffusivity increases as the aging temperature increases. Marginal differences are observed between the thermal diffusivity of the samples aged at high temperatures (575 ℃ and 650 ℃), while by comparison a little bit smaller value is seen in the sample aged at 500 ℃. This indicates that aging at 575 ℃ for 2 hours is sufficient for the complete precipitation of chromium solution atoms. Another possible explanation should be the formation of finer precipitates in the sample aged at 500 ℃, acting as the heat barriers for reducing the phonon mean free path [101]. When the testing temperatures is above 600 ℃, thermal diffusivities of all the samples overlap one another. Apparently, as shown in Fig. 6.14(b), with the second testing cycle, thermal diffusivities are almost identical for all samples over the entire temperature range.

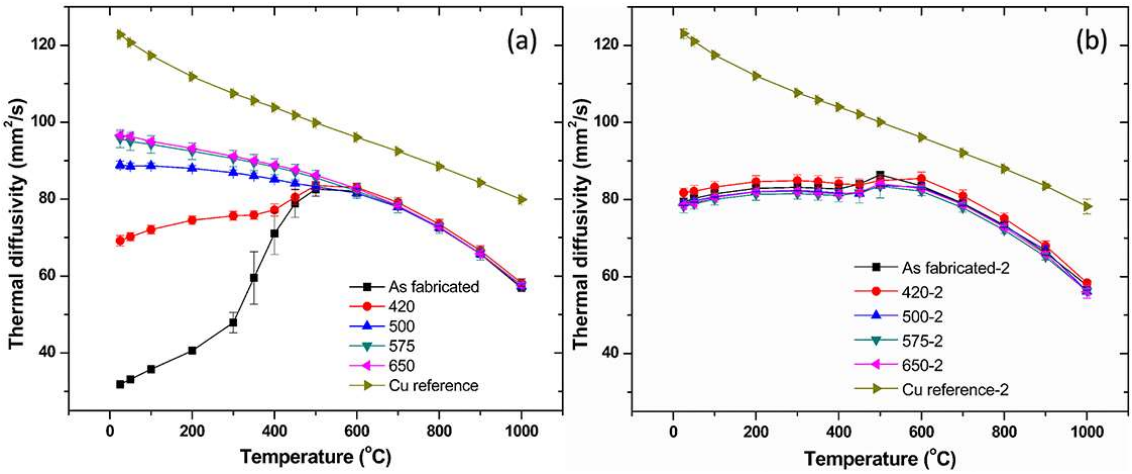

Figure 6.14. Thermal diffusivity of the samples before and after aging treatments. (a) First testing cycle (heating to 1000 ℃). (b) Second testing cycle (repeated heating to 1000 ℃).

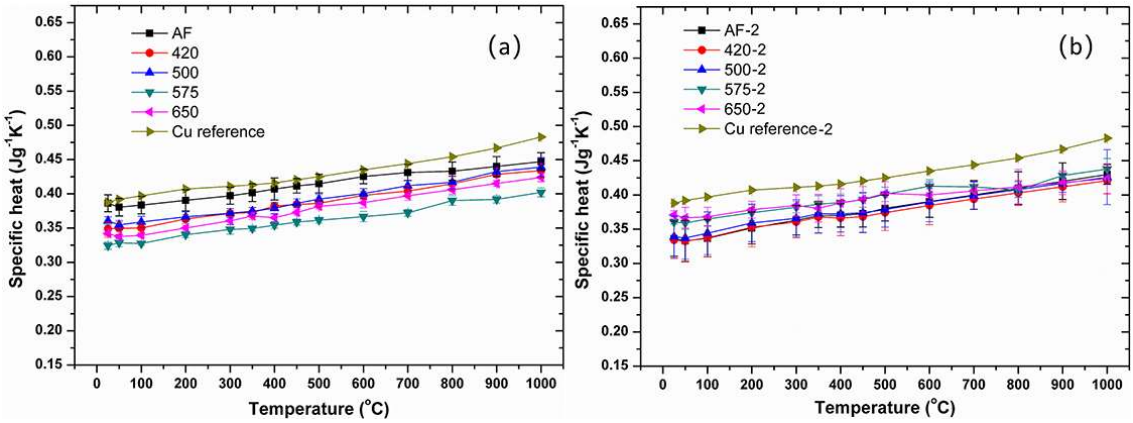

Figure 6.15. Specific heat of the Vertical samples before and after aging treatments. (a) First testing cycle (heating to 1000 °C). (b) Second testing cycle (repeated heating to 1000 °C).

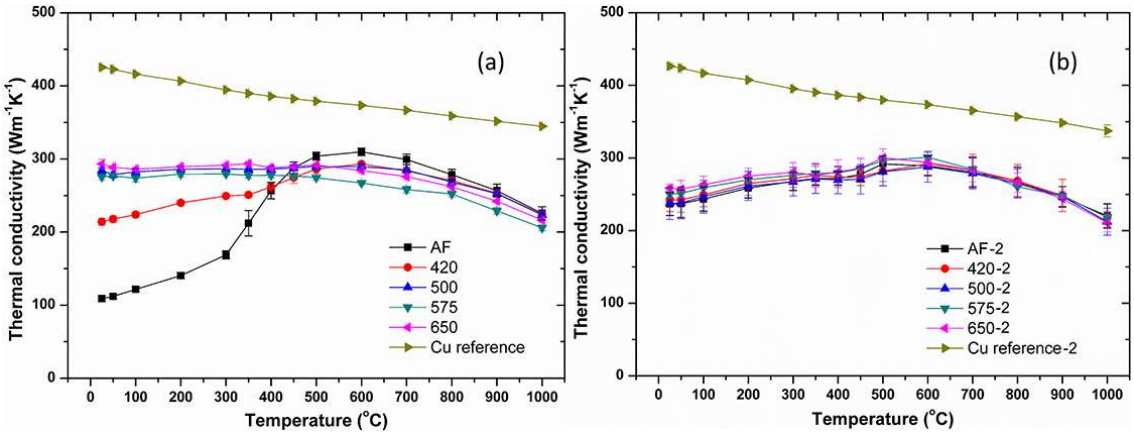

Figure 6.16. Thermal conductivity of the samples both before and after aging treatments. (a) First testing (heating to 1000 °C). (b) Second testing cycle (repeated heating to 1000 °C).

With the increase of testing temperature, specific heat of all the samples increases monotonically. Here again, it verifies that thermal diffusivity is the decisive factor of thermal conductivity. Based on Fig. 6.16(a), aging below 420 °C for 2 hours is inadquate to complete the precipitation process of the chromium atoms. And a good thermal conductivity of ~280 W/(m·K) at room temperature can be achieved when the aging temperature increases above 500 °C. According to Fig. 6.16, at low testing temperatures, thermal conductivity (the first testing cycle) of the samples aged above 500 °C is higher than that of the second testing cycle. This phenomenon can be explained by the over-aging effect after the first testing cycle (up to 1000 °C). Specifically, the non-coherency between the cooper matrix and precipitates enhances

the scattering effect, decreasing the thermal conductivity. Based on Fig. 6.16(b), the second testing cycle shows almost identical thermal conductivity values for all samples.

6.3.4 Tensile and hardness tests

Tensile strength and ductility of all the samples are inversely related to the testing temperature, which can be explained by the dynamic recrystallization process during the tensile testing at high temperatures. For the as-fabricated samples, the ductility for Horizontal and Angled samples is similar (~0.3) while Vertical samples show a decreased strain-to-failure value (~0.2) (Fig. 6.17). The strain-to-failure decreases as the testing temperature increases. Meanwhile, the proof stress of the Angled and Horizontal samples is slightly higher than that of the Vertical samples. Grain alignment along the elongated direction can be clearly seen in Figs. 6.18 (d) and (e) for the samples tested at room temperature and 204 ℃ due to the higher ductility. Based on the curves in Fig. 6.17, due to the work hardening effect, after the yield stress, the tensile stress keeps increasing almost linearly as a function of strain until the ultimate tensile stress is reached [315].

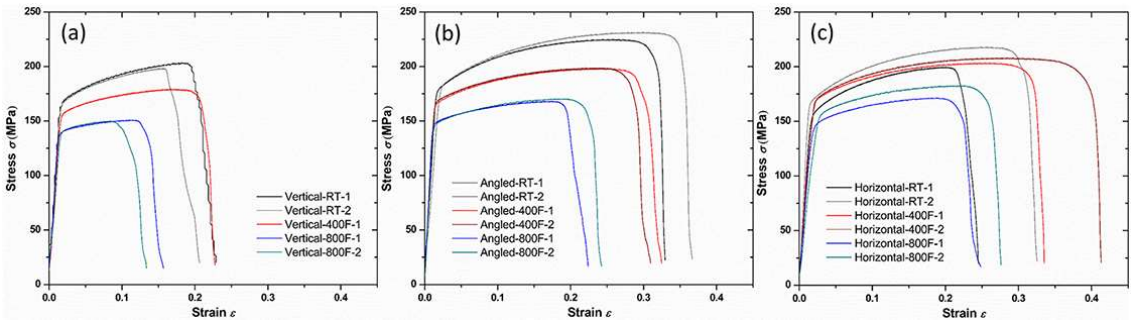

Figure 6.17. Images showing the tensile test results for as-fabricated samples with differing orientations at room temperature, 204℃ and 800 ℃, (a) Vertical, (b) Angled, and (c) Horizontal.

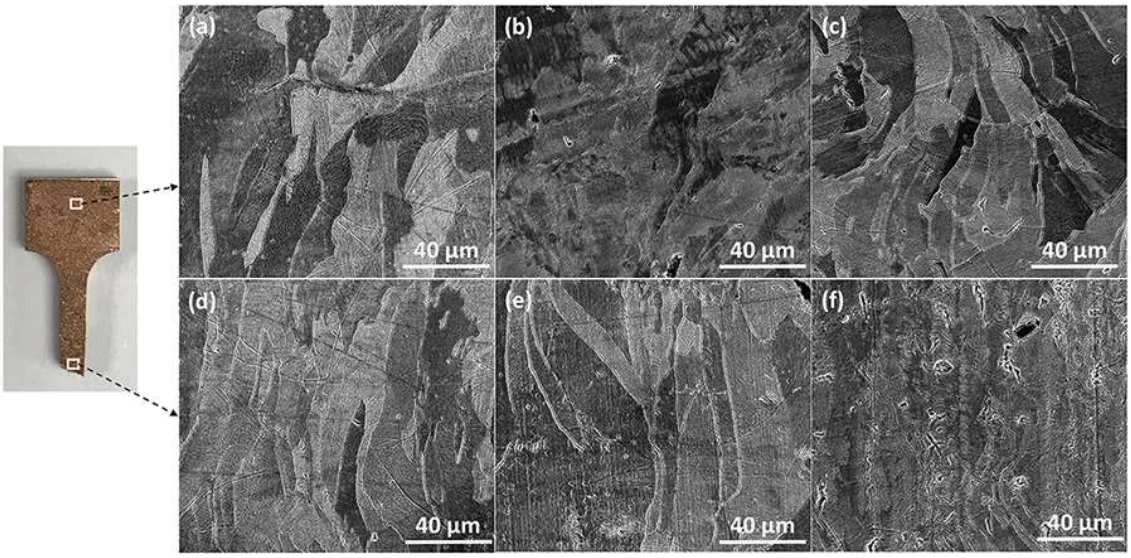

Figure 6.18. SEM images indicating the microstructures after tensile testing both near and remote from the fracture surface. (a)(d) Vertical, (b)(e) Angled, and (c)(f) Horizontal.

High-temperature tensile testing was also performed on aged Vertical samples under room temperature, 204 °C, and 427 °C, which are shown in Fig. 6.19. Again, the tensile strength and ductility of the samples are inversely related to the testing temperatures, which is consistent with previous studies [295, 298]. According to previous studies [116, 316], at low aging temperatures (i.e. below 420 °C), Guiner-Preston (GP) parts form, which are nanometer-sized clusters generated in a supersaturated solid solution during the early stage of aging [317]. The peak tensile strength while the lowest ductility are observed when the aging condition is 500 °C for 2 hours.

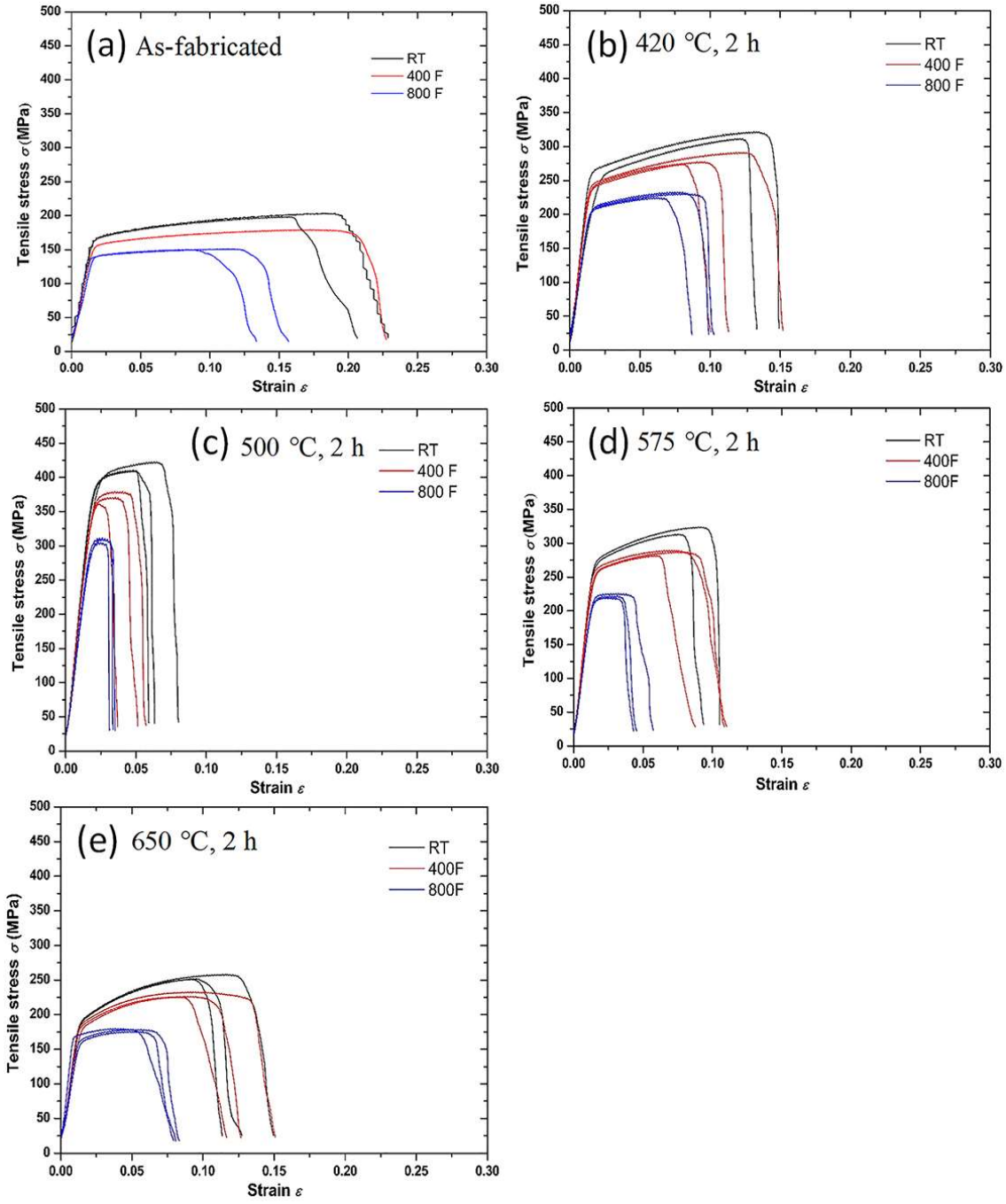

Figure 6.19. Tensile test results of Vertical samples tested under room temperature, 204 ℃, and 427 ℃. (a) As-fabricated samples. Samples after aging at (b) 420 ℃. (c) 500 ℃. (d) 575 ℃. (e) 650 ℃ for 2 hours.

First, the improvements of tensile stress is due to the fine dispersed precipitates formed during the aging process [118, 306, 318], which have coherency relation with the matrix. And it has been reported that the fine precipitates with sizes from a few nanometers to >10

nanometers can efficiently hinder the motion of dislocations, substantially enhancing the mechanical strength [114, 319, 320].

Second, coarse precipitates with the size of several hundred nanometers show neglectable influence on mechanical performance according to Wallis and Buchmayr [101]. And it was pointed out that coarser precipitates leads to larger interparticle spacing, in which case the particles cannot efficiently pin the dislocations [294]. However, in another research work, it was discovered that the chromium precipitates (with the size of several hundred nanometers) were surrounded by dense dislocations with the help of bright field TEM image [114], revealing the hardening effect of the coarse precipitates. Since the peak tensile strength and coarse precipitates were achieved when the aging temperature was 500 ℃, it is reasonable to believe that the strengthening of the sample originate from both the fine and coarse precipitates. Over-aging occurs at higher aging temperatures (i.e. 575 ℃ and 650 ℃), which makes the size of the precipitates coarser, deteriorating the coherency between copper matrix and precipitates [117], worsening the strengthening effect of the precipitates [116]. Orowan mechanism is responsible for the improvement of tensile strength [117], which is demonstrated with the equation below,

$$\Delta\tau = k \cdot f^{1/2} \cdot R^{-1} \tag{6-5}$$

where $\Delta\tau$, k, f, and R are the shear stress increase, constant, volume fraction of the precipitates and size of the precipitates, respectively. Obviously, smaller size and large friction of precipitates that have good coherency with the matrix lead to larger $\Delta\tau$ with which.

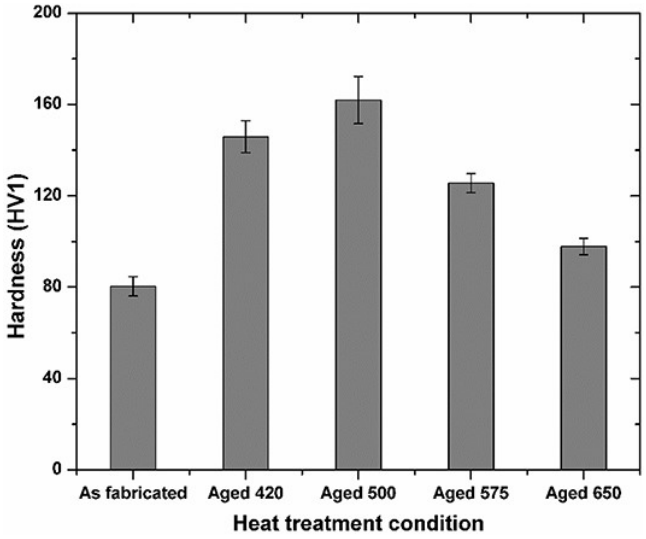

Figure 6.20. Image showing the hardness test results of the samples both before and after aging treatments.

Hardness of an alloy is typically linked with its ductility and tensile strength. Hardness tests were performed on the Vertical samples both before and after aging treatments, and clearly according to Fig. 6.20, the hardness test results were in accordance with the tensile testing results above. Apparently, when the sample was aged at 500 ℃ for 2 hours, the peak hardness is achieved, which is twice the hardness of the as-fabricated sample (Table 6.2). Similar studies were also performed by other researchers, where the sample was aged at 450 ℃ for 2 hours, and a hardness of 185 ± 2 HV1 was obtained [101]. Besides, Kalinin et al. [302] reported that the optimum aging profile was 480 ℃ and 2 hours. The relatively lower hardness values acquired in this study illustrates that the best aging temperature should be between 420 ℃ and 500 ℃. Therefore, further investigation on the aging temperatures between 420 ℃ and 500 ℃ to achieve the optimum mechanical properties is worth pursuing.

6.4. Conclusions

Cu-Cr1.5-Zr0.5 L-PBF samples have been examined to investigate the effect of sample preparation orientations and heat treatments on the microstructures, phase constituents, thermal properties, and mechanical properties. And the following conclusions are achieved.

(1) Due to the complex thermal gradients and fast cooling rate of the laser melting based L-PBF process, the typical small-sized, irregular-shaped, and hierarchical grain structures are seen. Anisotropy is observed in the sample due to the preferential growth of the columnar grains, which shows strong influences on the mechanical properties of the samples.

(2) Tensile testing shows that L-PBF parts with the angled and horizontal building orientations show higher tensile strength and ductility than the samples with vertical building orientation.

(3) According to Thermo-Calc calculations, FCC copper is found to be the dominant phase, in line with the results of DSC and XRD tests. Chromium and zirconium are supersaturated in the copper matrix due to the rapid cooling of the molten tracks. After the direct aging, chromium rich second phase are generated.

(4) The as-fabricated samples show much reduced thermal conductivity due to the supersaturated chromium and zirconium atoms in the copper matrix. Thermal diffusivity is the decisive factor of thermal conductivity. Thermal conductivity of the as-fabricated samples first increases relatively slowly from ~105 to ~165 W/(m·K), and then quickly goes up to ~300 W/(m·K), and finally declines to ~220 W/(m·K) from room temperature to 300℃, from 300 to 600℃ and from 600 to 1000℃, respectively. The low thermal conductivity caused by the supersaturated chromium/zirconium in the copper matrix can effectively be recovered by an aging temperature of 500 ℃ (2h). Aging at 500 ℃ also results in the highest yield strength and the best hardness value.

Chapter 7. Conclusions

This work investigated the laser surface engineering of pure titanium under controlled atmosphere (both nitrogen and ambient air) and the Cu-10Sn alloy samples prepared with LPBF-AM. The following conclusions can be reached.

(1) According to the results of SXRD test, the high temperature reactions steps between titanium and nitrogen were αTi→ βTi→ αTi+βTi→ liquid+αTi→ liquid+TiN→ solid+TiN. TiN and $TiN_{0.26}$ were identified, and the content of which decreased with the increase of scanning speed. Nitrogen content on sample surfaces increased with the increase of N_2 content in the processing chamber under the same laser processing parameters, which increased from 5.54% to 32.45% based on XPS results when N_2 content increased from 50% to 100%.

(2) The synchrotron X-ray diffraction test reveals the *in-situ* dynamic reaction steps between pure Ti and air. The phase transformation steps during the laser melting and cooling process are found to be αTi→ βTi→ αTi+βTi→ αTi+TiN+TiN_x (+LTO)→ liquid+TiN (+LTO)→ TiN+TiO_xN_y (+LTO)→ TiO_2+TiN. For the first time, the high-temperature diffusion coefficients of oxygen and nitrogen into laser irradiated Ti samples in air are estimated. Over the temperature range 1843 ℃ - 2930 ℃, the diffusion coefficients of nitrogen and oxygen into Ti are estimated to be 4.00×10^{-5} - 4.24×10^{-2} cm^2/s and 8.00×10^{-7}-1.00×10^{-5} cm^2/s, respectively, while the diffusion coefficient of oxygen in TiN is 4.34×10^{-9} cm^2/s.

(3) Under pure N_2, a thick and compact (~ 66 μm) titanium-nitride dendrites layer formed on the Ti-N100 surface, while inhomogeneous titanium-nitride layers appeared on Ti-N400 (~26 μm) and Ti-N1600 (~12 μm). A thin titanium-nitride layer was found on the surface of the Ti-N75% sample. However, with diluted N_2 conditions, coating layer are invisible. Although no clear differences in cell adhesion and proliferation were

observed, the high apoptosis rates associated with Ti-N50%, Ti-N20% and Ti-N0%. This shows the benefit of laser nitrided coatings for improving bio-compatibility performance. Ti-N100 has the best corrosion resistance due to the thick layer of TiN dendrites on the outermost surface. To achieve the optimal bio-compatibility and corrosion resistance performance, a dense and thick titanium-nitride dendrites layer is desirable.

(4) The as-fabricated Cu-10Sn samples under two different building orientations were found to have similar compression strength, thermal conductivity, and corrosion properties. The as-fabricated samples have fine grains with average grain size ~2 μm, and consist of a Cu-rich α phase and a Sn-rich δ phase due to the rapid cooling during the laser powder bed fusion additive manufacturing. Vacuum-annealed samples possess equiaxed grains, and grain sizes increase significantly. Only α phase can be detected in vacuum-annealed samples. The as-fabricated samples exhibit a much higher compression strength than vacuum-annealed samples due to the smaller grain size, existence of phase interfaces, and high dislocation density. Thermal conductivity of the as-fabricated samples is ~10% and over 20% higher than that of 800 ℃ and 600 ℃ annealed samples, respectively, which can be attributed to the high-thermal-conductivity of the α phase, lower porosity, and nano-sized pores in the as-fabricated samples. Heat treatment results in a significant improvement in corrosion performance by decreasing the corrosion rate by almost 50% due to the modification of passive layer morphology as well as the decrease of the susceptibility to intergranular corrosion and internal galvanic corrosion.

(5) The typical small-sized, irregular-shaped, and hierarchical grain structures are seen in the as-fabricated Cu-1.5Cr-0.5Zr alloy. Anisotropy in the sample shows strong influences on the mechanical properties of the samples, but no clear effects

on thermal properties. Tensile testing shows that as-fabricated parts with the angled and horizontal building orientations show higher tensile strength and ductility than the samples with vertical building orientation. FCC Cu is found to be the dominant phase at room temperature. After the direct aging, Cr rich second phase are generated. The as-fabricated samples show much reduced thermal conductivity due to the supersaturated Cr/Zr atoms in the Cu matrix. Thermal diffusivity is the decisive factor of thermal conductivity. Thermal conductivity of the as-fabricated samples first increases relatively slowly from ~105 to ~165 W/(m·K), and then quickly goes up to ~300 W/(m·K), and finally declines to ~220 W/(m·K) from room temperature to 300℃, from 300 to 500℃ and from 500 to 1000℃, respectively. The low thermal conductivity caused by the supersaturated Cr/Zr in the Cu matrix can be effectively recovered by an aging temperature of 500 ℃ (2h). Aging at 500 ℃ also results in the highest yield strength and the best hardness value.

Appendix. Reprint Permissions

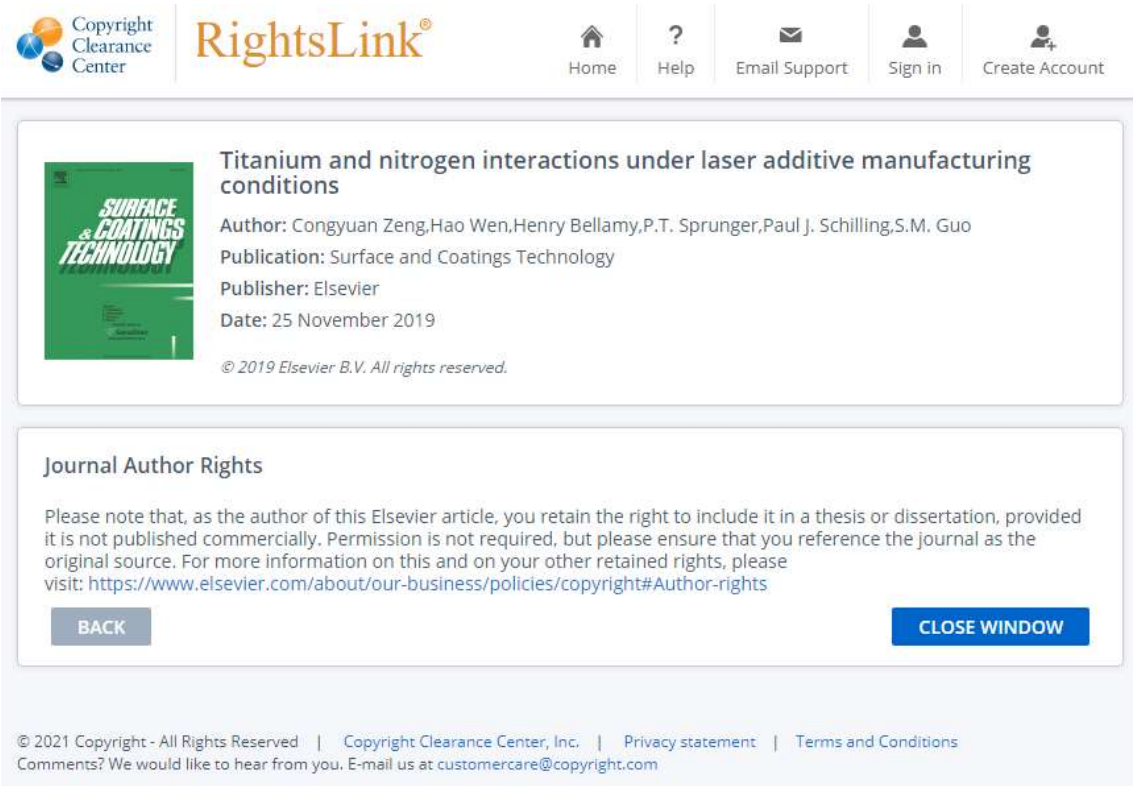

A.1. Reprint permission from the publisher for Chapter 2.

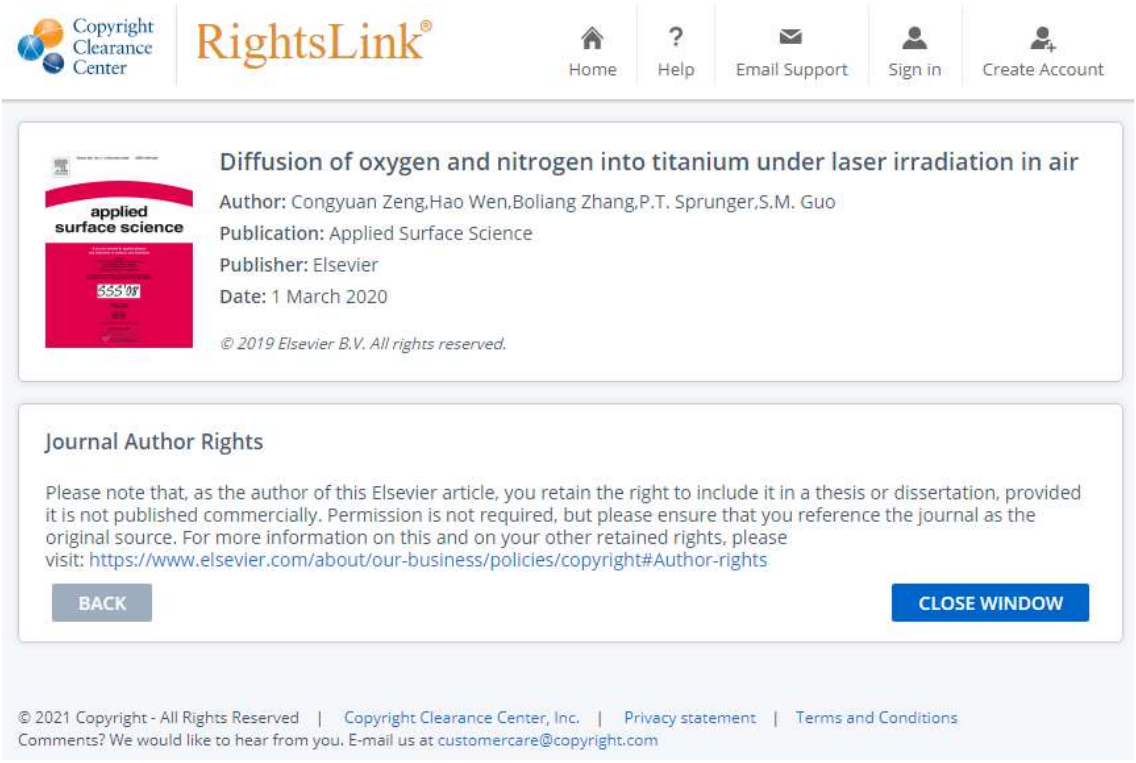

A.2. Reprint permission from the publisher for Chapter 3.

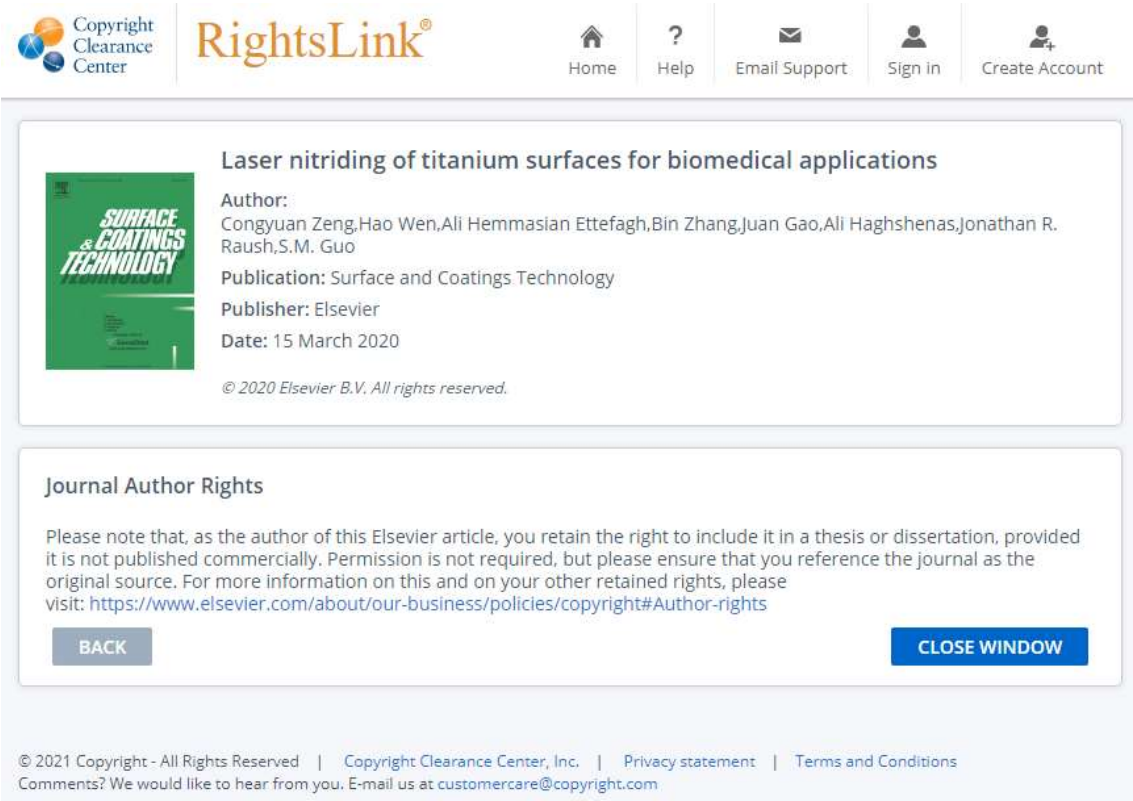

A.3. Reprint permission from the publisher for Chapter 4.

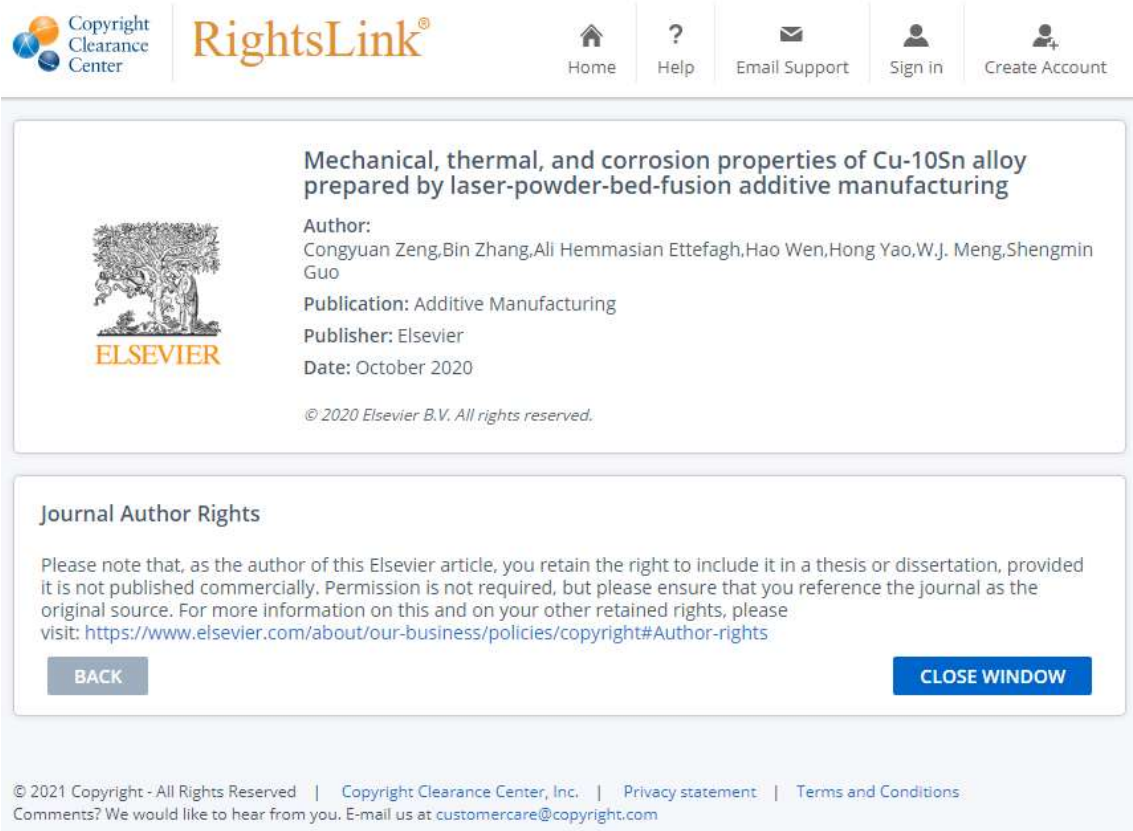

A.4. Reprint permission from the publisher for Chapter 5.

References

[1] J.D. Majumdar, I. Manna, Laser processing of materials, Sadha 28(3-4) (2003) 495-562.

[2] G. Padmanabham, R. Bathe, Laser materials processing for industrial applications, Proceedings of the National Academy of Sciences, India Section A: Physical Sciences 88(3) (2018) 359-374.

[3] L.R. Migliore, Laser materials processing, CRC Press2018.

[4] C. Kwok, H. Man, F. Cheng, K. Lo, Developments in laser-based surface engineering processes: with particular reference to protection against cavitation erosion, Surface and Coatings Technology 291 (2016) 189-204.

[5] A. Lisiecki, Study of optical properties of surface layers produced by laser surface melting and laser surface nitriding of titanium alloy, Materials 12(19) (2019) 3112.

[6] A. Keating, X. Sun, Selective Oxidation and Carbonization by Laser Writing into Porous Silicon, Advanced Materials Technologies 4(1) (2019) 1800334.

[7] Z. Sun, X. Tan, S.B. Tor, W.Y. Yeong, Selective laser melting of stainless steel 316L with low porosity and high build rates, Materials & Design 104 (2016) 197-204.

[8] Y. Hu, F. Ning, W. Cong, Y. Li, X. Wang, H. Wang, Ultrasonic vibration-assisted laser engineering net shaping of ZrO2-Al2O3 bulk parts: effects on crack suppression, microstructure, and mechanical properties, Ceramics International 44(3) (2018) 2752-2760.

[9] M. Leary, M. Mazur, J. Elambasseril, M. McMillan, T. Chirent, Y. Sun, M. Qian, M. Easton, M. Brandt, Selective laser melting (SLM) of AlSi12Mg lattice structures, Materials & Design 98 (2016) 344-357.

[10] H. Wei, J. Elmer, T. DebRoy, Crystal growth during keyhole mode laser welding, Acta Materialia 133 (2017) 10-20.

[11] W. Reimann, S. Pfriem, T. Hammer, D. Päthe, M. Ungers, K. Dilger, Influence of different zinc coatings on laser brazing of galvanized steel, Journal of Materials Processing Technology 239 (2017) 75-82.

[12] K.L. Wlodarczyk, A. Brunton, P. Rumsby, D.P. Hand, Picosecond laser cutting and drilling of thin flex glass, Optics and Lasers in Engineering 78 (2016) 64-74.

[13] D. Herzog, M. Schmidt-Lehr, M. Oberlander, M. Canisius, M. Radek, C. Emmelmann, Laser cutting of carbon fibre reinforced plastics of high thickness, Materials & Design 92 (2016) 742-749.

[14] W. Zhao, J. Wu, A. Hu, M. Li, D. Mao, An investigation into copper oxidation behavior, 2010 11th international conference on electronic packaging technology & high density packaging, IEEE, 2010, pp. 319-323.

[15] F. Weng, H. Yu, C. Chen, J. Liu, L. Zhao, J. Dai, Z. Zhao, Effect of process parameters on the microstructure evolution and wear property of the laser cladding coatings on Ti-6Al-4V alloy, Journal of alloys and compounds 692 (2017) 989-996.

[16] N. Dai, L.-C. Zhang, J. Zhang, Q. Chen, M. Wu, Corrosion behavior of selective laser melted Ti-6Al-4 V alloy in NaCl solution, Corrosion Science 102 (2016) 484-489.

[17] S. Bagherifard, M. Guagliano, Fatigue behavior of a low-alloy steel with nanostructured surface obtained by severe shot peening, Engineering Fracture Mechanics 81 (2012) 56-68.

[18] A. Solouk, B.G. Cousins, H. Mirzadeh, A.M. Seifalian, Application of plasma surface modification techniques to improve hemocompatibility of vascular grafts: A review, biotechnology and applied biochemistry 58(5) (2011) 311-327.

[19] J. Yang, F.-z. Cui, I.S. Lee, X. Wang, Plasma surface modification of magnesium alloy for biomedical application, Surface and Coatings Technology 205 (2010) S182-S187.

[20] K. Bazaka, M.V. Jacob, R.J. Crawford, E.P. Ivanova, Plasma-assisted surface modification of organic biopolymers to prevent bacterial attachment, Acta biomaterialia 7(5) (2011) 2015-2028.

[21] S. Jiang, C. Xu, H. Li, S. Liu, J. Gong, C. Sun, Preparation and oxidation behaviour of an AlSiY diffusion coating on a Ni-based single crystal superalloy, Corrosion Science 52(2) (2010) 435-440.

[22] J. Hirmke, M.-X. Zhang, D. StJohn, Surface alloying of AZ91E alloy by Al–Zn packed powder diffusion coating, Surface and Coatings Technology 206(2-3) (2011) 425-433.

[23] J. Hirmke, M.-X. Zhang, D. St John, Influence of chemical composition of Mg alloys on surface alloying by diffusion coating, Metallurgical and Materials Transactions A 43(5) (2012) 1621-1628.

[24] S. Akhtar, A. Arif, B.S. Yilbas, Evaluation of gas nitriding process with in-process variation of nitriding potential for AISI H13 tool steel, The International Journal of Advanced Manufacturing Technology 47(5-8) (2010) 687-698.

[25] L. Ge, N. Tian, Z. Lu, C. You, Influence of the surface nanocrystallization on the gas nitriding of Ti–6Al–4V alloy, Applied Surface Science 286 (2013) 412-416.

[26] D. Peng, T.-H. Kim, J.-H. Chung, J.-K. Park, Development of nitride-layer of AISI 304 austenitic stainless steel during high-temperature ammonia gas-nitriding, Applied Surface Science 256(24) (2010) 7522-7529.

[27] X. Pham, A. Hoang, D. Nguyen, V. Le, Effect of Factors on the Hydrogen Composition in the Carburizing Process, International Journal of Applied Engineering Research 12(19) (2017) 8238-8244.

[28] M. Tsujikawa, D. Yoshida, N. Yamauchi, N. Ueda, T. Sone, S. Tanaka, Surface material design of 316 stainless steel by combination of low temperature carburizing and nitriding, Surface and Coatings Technology 200(1-4) (2005) 507-511.

[29] M. Boniardi, F. D'Errico, C. Tagliabue, Influence of carburizing and nitriding on failure of gears–A case study, Engineering Failure Analysis 13(3) (2006) 312-339.

[30] A. Kohli, H. Singh, Optimization of processing parameters in induction hardening using response surface methodology, Sadhana 36(2) (2011) 141-152.

[31] H. Kristoffersen, P. Vomacka, Influence of process parameters for induction hardening on residual stresses, Materials & Design 22(8) (2001) 637-644.

[32] T.J. Stich, J.K. Spoerre, T. Velasco, The application of artificial neural networks to monitoring and control of an induction hardening process, Journal of Industrial Technology 16(1) (2000) 1-11.

[33] Y. Ni, G. Dong, Z. Tong, X. Li, W. Wang, Effect of laser remelting on tribological properties of Babbitt alloy, Materials Research Express 6(9) (2019) 096570.

[34] R. Xiao, X. Zhang, Problems and issues in laser beam welding of aluminum–lithium alloys, Journal of Manufacturing Processes 16(2) (2014) 166-175.

[35] A. Agarwal, N.B. Dahotre, Laser surface engineering of steel for hard refractory ceramic composite coating, International Journal of Refractory Metals and Hard Materials 17(4) (1999) 283-293.

[36] C. Draper, J. Poate, Laser surface alloying, International metals reviews 30(1) (1985) 85-108.

[37] P. Molian, Surface modification technologies-An engineers guide (ed.) TS Sudarshan, NY: Macel Dekker (1989) 421.

[38] A. Lisiecki, J. Piwnik, Tribological characteristic of titanium alloy surface layers produced by diode laser gas nitriding, Archives of Metallurgy and Materials 61(2A) (2016) 543--552.

[39] C.-W. Chan, S. Lee, G. Smith, G. Sarri, C.-H. Ng, A. Sharba, H.-C. Man, Enhancement of wear and corrosion resistance of beta titanium alloy by laser gas alloying with nitrogen, Applied Surface Science 367 (2016) 80-90.

[40] M. Ansari, M.H. Sohi, R. Soltani, M.J. Torkamany, Effect of pulsed Nd: YAG laser re-melting on chromium surface alloyed AA6061-T6 aluminum, The International Journal of Advanced Manufacturing Technology 83(1-4) (2016) 285-291.

[41] Y. Chi, G. Gu, H. Yu, C. Chen, Laser surface alloying on aluminum and its alloys: A review, Optics and Lasers in Engineering 100 (2018) 23-37.

[42] C. Park, A. Sim, S. Ahn, H. Kang, E.-J. Chun, Influence of laser surface engineering of AISI P20-improved mold steel on wear and corrosion behaviors, Surface and Coatings Technology 377 (2019) 124852.

[43] O.S. Fatoba, A.P. Popoola, V.S. Aigbodion, Electrochemical studies and surface analyses of laser deposited Zn-Al-Sn coatings on AISI 1015 steel, International Journal of Surface Science and Engineering 12(1) (2018) 40-59.

[44] I. Khadka, S. Castagne, Z. Wang, H. Zheng, Investigation of wettability properties of laser surface modified rare earth Mg alloy, Procedia Engineering 141 (2016) 63-69.

[45] J. Hlinka, Z. Weltsch, Analysis of Laser Treated Copper Surfaces, Periodica Polytechnica Transportation Engineering 47(2) (2019) 140-145.

[46] S.N. Dahotre, H.D. Vora, K. Pavani, R. Banerjee, An integrated experimental and computational approach to laser surface nitriding of Ti–6Al–4V, Applied surface science 271 (2013) 141-148.

[47] G.H. Frydman, R.P. Marini, V. Bakthavatchalu, K.E. Biddle, S. Muthupalani, C.R. Vanderburg, B. Lai, P.K. Bendapudi, R.G. Tompkins, J.G. Fox, Local and systemic changes associated with long-term, percutaneous, static implantation of titanium alloys in rhesus macaques (Macaca mulatta), Comp. Med. 67(2) (2017) 165-175.

[48] Z. Sun, I. Annergren, D. Pan, T. Mai, Effect of laser surface remelting on the corrosion behavior of commercially pure titanium sheet, Materials Science and Engineering: A 345(1-2) (2003) 293-300.

[49] V. Weerasinghe, D. West, J. De Damborenea, Laser surface nitriding of titanium and a titanium alloy, Journal of materials processing technology 58(1) (1996) 79-86.

[50] A.P. Del Pino, P. Serra, J. Morenza, Oxidation of titanium through Nd: YAG laser irradiation, Applied Surface Science 197 (2002) 887-890.

[51] R. Kumari, T. Scharnweber, W. Pfleging, H. Besser, J.D. Majumdar, Laser surface textured titanium alloy (Ti–6Al–4V)–Part II–Studies on bio-compatibility, Applied Surface Science 357 (2015) 750-758.

[52] C. Wang, H. Hu, Z. Li, Y. Shen, Y. Xu, G. Zhang, X. Zeng, J. Deng, S. Zhao, T. Ren, Enhanced osseointegration of titanium alloy implants with laser microgrooved surfaces and graphene oxide coating, ACS applied materials & interfaces 11(43) (2019) 39470-39483.

[53] R. Honda, M. Mizutani, H. Ohmori, J. Komotori, Biocompatibility evaluation of nanosecond laser treated titanium surfaces, International Journal of Modern Physics: Conference Series, World Scientific, 2012, pp. 682-687.

[54] T. Zhang, Q. Fan, X. Ma, W. Wang, K. Wang, P. Shen, J. Yang, Microstructure and mechanical properties of Ti-35Nb-2Ta-3Zr alloy by laser quenching, Frontiers in Materials 6 (2019) 318.

[55] Y. Geng, É. McCarthy, D. Brabazon, N. Harrison, Ti6Al4V functionally graded material via high power and high speed laser surface modification, Surface and Coatings Technology 398 (2020) 126085.

[56] N. Khun, A. Tan, W. Sun, E. Liu, Effects of Nd: YAG Laser Surface Treatment on Tribological Properties of Cold-Sprayed Ti-6Al-4V Coatings Tested against 100Cr6 Steel under Dry Condition, Tribology Transactions 62(3) (2019) 391-402.

[57] D. Dias, O.S. Santos, W. Alves, M.S.F. Lima, M.M.d. Silva, Fiber Laser Surface Melting of a NiTi Superelastic Alloy: Influence on Structural and Mechanical Properties, Metals 9(12) (2019) 1268.

[58] Y. Tian, C. Chen, D. Wang, Q. Huo, T. Lei, Wear and oxidation resistance coatings fabricated on Ti-6Al-4v by laser surface alloying technique, Surface Review and Letters 12(02) (2005) 209-213.

[59] R. Olsson, J. Powell, A. Palmquist, R. Brånemark, J. Frostevarg, A.F. Kaplan, Formation of osseointegrating (bone integrating) surfaces on titanium by laser irradiation, Journal of Laser Applications 31(2) (2019) 022508.

[60] G. Tang, A. Abdolvand, Structuring of titanium using a nanosecond-pulsed Nd: YVO 4 laser at 1064 nm, The International Journal of Advanced Manufacturing Technology 66(9-12) (2013) 1769-1775.

[61] X. Chang, G.C. Smith, J. Quinn, L. Carson, C.-W. Chan, S. Lee, Optimization of anti-wear and anti-bacterial properties of beta TiNb alloy via controlling duty cycle in open-air laser nitriding, Journal of the Mechanical Behavior of Biomedical Materials 110 (2020) 103913.

[62] X. Zong, H. Wang, Z. Li, J. Li, X. Cheng, Y. Zhu, X. Tian, H. Tang, Laser nitridation on Ti-6.5 Al-3.5 Mo-1.5 Zr-0.3 Si titanium alloy, Surface and Coatings Technology 386 (2020) 125425.

[63] L.A. Narciso da Silva Briguente, J. Oñoro, F. Perpétuo Briguente, F. Assis Resende, J. Lidovino dos Reis, D.A. Pereira Reis, A.C. de Oliveira, The influence of laser nitriding on creep behavior of Ti-4Al-4V alloy with widmanstätten microstructure, Metals 9(2) (2019) 236.

[64] J. Guo, Y. Shi, P. Geng, G. Zhang, M. Zhu, The Surface Morphology of a Ti–6Al–4V Fiber-Lasered Nitride Layer, Coatings 10(5) (2020) 451.

[65] C.L. Donaghy, R. McFadden, S. Kelaini, L. Carson, A. Margariti, C.-W. Chan, Creating an antibacterial surface on beta TNZT alloys for hip implant applications by laser nitriding, Optics & Laser Technology 121 (2020) 105793.

[66] K.Z.T.A.V.M. LASERSKO-PLINSKIM, Mechanisms of hardness increase for composite surface layers during laser gas nitriding of the Ti6Al4V alloy, Materiali in tehnologije 51(4) (2017) 577-583.

[67] A. Lisiecki, A. Klimpel, Diode laser gas nitriding of Ti6Al4V alloy, Archives of materials science and engineering 31(1) (2008) 53-56.

[68] M. Marticorena, G. Corti, D. Olmedo, M. Guglielmotti, S. Duhalde, Laser surface modification of Ti implants to improve osseointegration, Journal of Physics: Conference Series, 2007, pp. 662-665.

[69] F.J. Braga, R.F. Marques, E. de A Filho, A.C. Guastaldi, Surface modification of Ti dental implants by Nd: YVO4 laser irradiation, Applied Surface Science 253(23) (2007) 9203-9208.

[70] P. Jiang, X. He, X.a. Li, L. Yu, H. Wang, Wear resistance of a laser surface alloyed Ti–6Al–4V alloy, Surface and Coatings Technology 130(1) (2000) 24-28.

[71] A. Lisiecki, Titanium matrix composite Ti/TiN produced by diode laser gas nitriding, metals 5(1) (2015) 54-69.

[72] N. Ohtsu, W. Saito, M. Yamane, Thickness of titanium nitride layers formed by focused low-power pulsed Nd: YAG laser irradiation in nitrogen atmospheres, Surface and Coatings Technology 244 (2014) 57-62.

[73] C. Hu, T. Baker, The importance of preheat before laser nitriding a Ti–6Al–4V alloy, Materials Science and Engineering: A 265(1-2) (1999) 268-275.

[74] S. Yerramareddy, S. Bahadur, The effect of laser surface treatments on the tribological behavior of Ti-6Al-4V, Wear 157(2) (1992) 245-262.

[75] J.H. Abboud, A. Fidel, K. Benyounis, Surface nitriding of Ti–6Al–4V alloy with a high power CO2 laser, Optics & Laser Technology 40(2) (2008) 405-414.

[76] D. Wang, Y. Zhou, J. Shen, Y. Liu, D. Li, Q. Zhou, G. Sha, P. Xu, T. Ebel, M. Yan, Selective laser melting under the reactive atmosphere: A convenient and efficient approach to fabricate ultrahigh strength commercially pure titanium without sacrificing ductility, Materials Science and Engineering: A 762 (2019) 138078.

[77] M. Raaif, F. El-Hossary, N. Negm, S. Khalil, A. Kolitsch, D. Höche, J. Kaspar, S. Maendl, P. Schaaf, CO2 laser nitriding of titanium, Journal of Physics D: Applied Physics 41(8) (2008) 085208.

[78] X. Zhang, Z. Liu, J. Xu, F. Xuan, Z. Wang, S. Tu, Synthesis of TiN/Ti3Al composite coatings on Ti6Al4V alloy by plasma spraying and laser nitriding, Surface and Coatings Technology 228 (2013) S107-S110.

[79] Y. Tian, L. Chen, C. Chen, Microstructures of composite coatings fabricated on Ti-6Al-4V by laser alloying technique, Crystal growth & design 6(6) (2006) 1509-1513.

[80] C.-W. Chan, X. Chang, M.A. Bozorgzadeh, G.C. Smith, S. Lee, A single parameter approach to enhance the microstructural and mechanical properties of beta Ti-Nb alloy via open-air fiber laser nitriding, Surface and Coatings Technology 383 (2020) 125269.

[81] J. Sobiecki, T. Wierzchoń, J. Rudnicki, The influence of glow discharge nitriding, oxynitriding and carbonitriding on surface modification of Ti–1Al–1Mn titanium alloy, Vacuu 64(1) (2001) 41-46.

[82] Z. Song, Z. Chunhua, W. Qiang, M. Hauchung, Z. Shenglong, C. Qingkui, Microstructure and were performance of the laser gas nitrided NiTi shape memory alloy, Rare Metal Materials and Engineering 34(6) (2005) 986.

[83] B. Berman, 3-D printing: The new industrial revolution, Business horizons 55(2) (2012) 155-162.

[84] M.J. Matthews, G. Guss, S.A. Khairallah, A.M. Rubenchik, P.J. Depond, W.E. King, Denudation of metal powder layers in laser powder bed fusion processes, Acta Materialia 114 (2016) 33-42.

[85] G. Kasperovich, J. Haubrich, J. Gussone, G. Requena, Correlation between porosity and processing parameters in TiAl6V4 produced by selective laser melting, Materials & Design 105 (2016) 160-170.

[86] T. Sercombe, X. Li, Selective laser melting of aluminium and aluminium metal matrix composites, Materials Technology 31(2) (2016) 77-85.

[87] S.A. Khairallah, A.T. Anderson, A. Rubenchik, W.E. King, Laser powder-bed fusion additive manufacturing: Physics of complex melt flow and formation mechanisms of pores, spatter, and denudation zones, Acta Materialia 108 (2016) 36-45.

[88] W.E. King, H.D. Barth, V.M. Castillo, G.F. Gallegos, J.W. Gibbs, D.E. Hahn, C. Kamath, A.M. Rubenchik, Observation of keyhole-mode laser melting in laser powder-bed fusion additive manufacturing, Journal of Materials Processing Technology 214(12) (2014) 2915-2925.

[89] S.L. Sing, W.Y. Yeong, F.E. Wiria, Selective laser melting of titanium alloy with 50 wt% tantalum: Microstructure and mechanical properties, Journal of Alloys and Compounds 660 (2016) 461-470.

[90] Y. Liu, S. Li, H. Wang, W. Hou, Y. Hao, R. Yang, T. Sercombe, L.C. Zhang, Microstructure, defects and mechanical behavior of beta-type titanium porous structures manufactured by electron beam melting and selective laser melting, Acta Materialia 113 (2016) 56-67.

[91] S. Ly, A.M. Rubenchik, S.A. Khairallah, G. Guss, M.J. Matthews, Metal vapor micro-jet controls material redistribution in laser powder bed fusion additive manufacturing, Scientific reports 7(1) (2017) 4085.

[92] M. Masoomi, S.M. Thompson, N. Shamsaei, Laser powder bed fusion of Ti-6Al-4V parts: Thermal modeling and mechanical implications, International Journal of Machine Tools and Manufacture 118-119 (2017) 73-90.

[93] H. Zhang, H. Zhu, T. Qi, Z. Hu, X. Zeng, Selective laser melting of high strength Al–Cu–Mg alloys: Processing, microstructure and mechanical properties, Materials Science and Engineering: A 656 (2016) 47-54.

[94] N.T. Aboulkhair, N.M. Everitt, I. Maskery, I. Ashcroft, C. Tuck, Selective laser melting of aluminum alloys, MRS Bulleti 42(4) (2017) 311-319.

[95] S.Z. Uddin, L.E. Murr, C.A. Terrazas, P. Morton, D.A. Roberson, R.B. Wicker, Processing and characterization of crack-free aluminum 6061 using high-temperature heating in laser powder bed fusion additive manufacturing, Additive Manufacturing 22 (2018) 405-415.

[96] M. Cloots, K. Kunze, P.J. Uggowitzer, K. Wegener, Microstructural characteristics of the nickel-based alloy IN738LC and the cobalt-based alloy Mar-M509 produced by selective laser melting, Materials Science and Engineering: A 658 (2016) 68-76.

[97] L.E. Criales, Y.M. Arısoy, B. Lane, S. Moylan, A. Donmez, T. Özel, Laser powder bed fusion of nickel alloy 625: Experimental investigations of effects of process parameters on melt pool size and shape with spatter analysis, International Journal of Machine Tools and Manufacture 121 (2017) 22-36.

[98] Y.M. Arısoy, L.E. Criales, T. Özel, B. Lane, S. Moylan, A. Donmez, Influence of scan strategy and process parameters on microstructure and its optimization in additively manufactured nickel alloy 625 via laser powder bed fusion, The International Journal of Advanced Manufacturing Technology 90(5) (2017) 1393-1417.

[99] S.D. Jadhav, S. Dadbakhsh, J. Vleugels, J. Hofkens, P. Van Puyvelde, S. Yang, J.-P. Kruth, J. Van Humbeeck, K. Vanmeensel, Influence of Carbon Nanoparticle Addition (and Impurities) on Selective Laser Melting of Pure Copper, Materials 12(15) (2019) 2469.

[100] C. Silbernagel, L. Gargalis, I. Ashcroft, R. Hague, M. Galea, P. Dickens, Electrical resistivity of pure copper processed by medium-powered laser powder bed fusion additive manufacturing for use in electromagnetic applications, Additive Manufacturing 29 (2019) 100831.

[101] C. Wallis, B. Buchmayr, Effect of heat treatments on microstructure and properties of CuCrZr produced by laser-powder bed fusion, Materials Science and Engineering: A 744 (2019) 215-223.

[102] J. Suryawanshi, K. Prashanth, U. Ramamurty, Mechanical behavior of selective laser melted 316L stainless steel, Materials Science and Engineering: A 696 (2017) 113-121.

[103] H. Choo, K.-L. Sham, J. Bohling, A. Ngo, X. Xiao, Y. Ren, P.J. Depond, M.J. Matthews, E. Garlea, Effect of laser power on defect, texture, and microstructure of a laser powder bed fusion processed 316L stainless steel, Materials & Design 164 (2019) 107534.

[104] M.J. Heiden, L.A. Deibler, J.M. Rodelas, J.R. Koepke, D.J. Tung, D.J. Saiz, B.H. Jared, Evolution of 316L stainless steel feedstock due to laser powder bed fusion process, Additive Manufacturing 25 (2019) 84-103.

[105] S.D. Jadhav, D. Fu, M. Deprez, K. Ramharter, D. Willems, B. Van Hooreweder, K. Vanmeensel, Highly conductive and strong CuSn0. 3 alloy processed via laser powder bed fusion starting from a tin-coated copper powder, Additive Manufacturing 36 (2020) 101607.

[106] B. Buchmayr, G. Panzl, A. Walzl, C. Wallis, Laser Powder Bed Fusion–Materials Issues and Optimized Processing Parameters for Tool steels, AlSiMg-and CuCrZr-Alloys, Advanced Engineering Materials 19(4) (2017) 1600667.

[107] C. Wallis, B. Buchmayr, M. Kitzmantel, Hybrid material systems with complex 3D structures for manufacturing of high performance heat sinks, Rapid.Tech ? International Trade Show & Conference for Additive Manufacturing, Carl Hanser Verlag GmbH & Co. KG2017, pp. 359-376.

[108] P. Becker, Selektives Laserschmelzen von Kupfer und Kupferlegierungen, Apprimus Verlag 2014.

[109] B. Buchmayr, G. Panzl, A. Walzl, C. Wallis, Laser Powder Bed Fusion – Materials Issues and Optimized Processing Parameters for Tool steels, AlSiMg- and CuCrZr-Alloys Advanced Engineering Materials 19(4) (2017) 1600667.

[110] C. Su, D. Li, A.A. Luo, T. Ying, X. Zeng, Effect of solute atoms and second phases on the thermal conductivity of Mg-RE alloys: A quantitative study, Journal of Alloys and Compounds 747 (2018) 431-437.

[111] A. Eivani, H. Ahmed, J. Zhou, J. Duszczyk, Correlation between electrical resistivity, particle dissolution, precipitation of dispersoids, and recrystallization behavior of AA7020 aluminum alloy, Metallurgical and Materials Transactions A 40(10) (2009) 2435-2446.

[112] A. Rudajevova, M. Staněk, P. Lukáč, Determination of thermal diffusivity and thermal conductivity of Mg–Al alloys, Materials Science and Engineering: A 341(1-2) (2003) 152-157.

[113] M. Hatakeyama, T. Toyama, J. Yang, Y. Nagai, M. Hasegawa, T. Ohkubo, M. Eldrup, B.N. Singh, 3D-AP and positron annihilation study of precipitation behavior in Cu–Cr–Zr alloy, Journal of Nuclear Materials 386-388 (2009) 852-855.

[114] S. Zhang, R. Li, H. Kang, Z. Chen, W. Wang, C. Zou, T. Li, T. Wang, A high strength and high electrical conductivity Cu-Cr-Zr alloy fabricated by cryorolling and intermediate aging treatment, Materials Science and Engineering: A 680 (2017) 108-114.

[115] Q. Liu, X. Zhang, Y. Ge, J. Wang, J.-Z. Cui, Effect of processing and heat treatment on behavior of Cu-Cr-Zr alloys to railway contact wire, Metallurgical and Materials Transactions A 37(11) (2006) 3233-3238.

[116] I. Sağlam, D. Özyürek, K. Çetinkaya, Effect of ageing treatment on wear properties and electrical conductivity of Cu-Cr-Zr alloy, Bulletin of Materials Science 34(7) (2011) 1465-1470.

[117] J. Tu, W. Qi, Y. Yang, F. Liu, J. Zhang, G. Gan, N. Wang, X. Zhang, M. Liu, Effect of aging treatment on the electrical sliding wear behavior of Cu–Cr–Zr alloy, Wear 249(10-11) (2001) 1021-1027.

[118] G. Lin, Z. Wang, M. Zhang, H. Zhang, M. Zhao, Heat treatment method for making high strength and conductivity Cu–Cr–Zr alloy, Materials Science and Technology 27(5) (2011) 966-969.

[119] Z. Mao, D.Z. Zhang, J. Jiang, G. Fu, P. Zhang, Processing optimisation, mechanical properties and microstructural evolution during selective laser melting of Cu-15Sn high-tin bronze, Materials Science and Engineering: A 721 (2018) 125-134.

[120] P. Cherian, R. Sellamuthu, An investigation on the effect of process parameters on microstructure, hardness and wear properties of surface modified Cu-Sn bronze alloy, Applied Mechanics and Materials, Applied Mechanics and Materials 2014, pp. 58-62.

[121] C. Paul, R. Sellamuthu, The effect of Sn content on the properties of surface refined Cu-Sn bronze alloys, Procedia Engineering 97 (2014) 1341-1347.

[122] A. Korneva, B. Straumal, A. Kilmametov, L. Lityńska-Dobrzyńska, G. Cios, P. Bała, P. Zięba, Effect of high pressure torsion on microstructure of Cu-Sn alloys with different content of Hume Rothery phase, Materials Characterization 118 (2016) 411-416.

[123] D. Šatović, L.V. Žulj, V. Desnica, S. Fazinić, S. Martinez, Corrosion evaluation and surface characterization of the corrosion product layer formed on Cu–6Sn bronze in aqueous Na2SO4 solution, Corrosion Science 51(8) (2009) 1596-1603.

[124] Z. Mao, D.Z. Zhang, P. Wei, K. Zhang, Manufacturing feasibility and forming properties of Cu-4Sn in selective laser melting, Materials 10(4) (2017) 333.

[125] A.P. Ventura, C.A. Wade, G. Pawlikowski, M. Bayes, M. Watanabe, W.Z. Misiolek, Mechanical properties and microstructural characterization of Cu-4.3 Pct Sn fabricated by selective laser melting, Metallurgical and Materials Transactions A 48(1) (2017) 178-187.

[126] S. Scudino, C. Unterdörfer, K. Prashanth, H. Attar, N. Ellendt, V. Uhlenwinkel, J. Eckert, Additive manufacturing of Cu–10Sn bronze, Materials Letters 156 (2015) 202-204.

[127] C. Deng, J. Kang, T. Feng, Y. Feng, X. Wang, P. Wu, Study on the selective laser melting of CuSn10 powder, Materials 11(4) (2018) 614.

[128] A. Bhat, V.K. Balla, S. Bysakh, D. Basu, S. Bose, A. Bandyopadhyay, Carbon nanotube reinforced Cu–10Sn alloy composites: mechanical and thermal properties, Materials Science and Engineering: A 528(22-23) (2011) 6727-6732.

[129] P.R. Gradl, C. Protz, S.E. Greene, D. Ellis, B. Lerch, I. Locci, Development and hot-fire testing of additively manufactured copper combustion chambers for liquid rocket engine applications, 53rd AIAA/SAE/ASEE Joint Propulsion Conference, 2017, p. 4670.

[130] P.R. Gradl, C.S. Protz, D.L. Ellis, S.E. Greene, Progress in Additively Manufactured Copper-Alloy GRCop-84, GRCop-42, and Bimetallic Combustion Chambers for Liquid Rocket Engines, (2019).

[131] H. Attar, S. Ehtemam-Haghighi, D. Kent, X. Wu, M.S. Dargusch, Comparative study of commercially pure titanium produced by laser engineered net shaping, selective laser melting and casting processes, Materials Science and Engineering: A 705 (2017) 385-393.

[132] I. Kunce, M. Polanski, K. Karczewski, T. Plocinski, K. Kurzydlowski, Microstructural characterisation of high-entropy alloy AlCoCrFeNi fabricated by laser engineered net shaping, Journal of Alloys and Compounds 648 (2015) 751-758.

[133] Z. Fan, Y. Zhao, Q. Tan, N. Mo, M.-X. Zhang, M. Lu, H. Huang, Nanostructured Al2O3-YAG-ZrO2 ternary eutectic components prepared by laser engineered net shaping, Acta Materialia 170 (2019) 24-37.

[134] V.K. Balla, A. Bandyopadhyay, Laser processing of Fe-based bulk amorphous alloy, Surface and Coatings Technology 205(7) (2010) 2661-2667.

[135] N. Read, W. Wang, K. Essa, M.M. Attallah, Selective laser melting of AlSi10Mg alloy: Process optimisation and mechanical properties development, Materials & Design (1980-2015) 65 (2015) 417-424.

[136] K. Prashanth, S. Scudino, J. Eckert, Defining the tensile properties of Al-12Si parts produced by selective laser melting, Acta Materialia 126 (2017) 25-35.

[137] G. Kasperovich, J. Hausmann, Improvement of fatigue resistance and ductility of TiAl6V4 processed by selective laser melting, Journal of Materials Processing Technology 220 (2015) 202-214.

[138] D. Gu, Y.-C. Hagedorn, W. Meiners, K. Wissenbach, R. Poprawe, Selective laser melting of in-situ TiC/Ti5Si3 composites with novel reinforcement architecture and elevated performance, Surface and Coatings Technology 205(10) (2011) 3285-3292.

[139] W.E. Frazier, Metal additive manufacturing: a review, Journal of Materials Engineering and performance 23(6) (2014) 1917-1928.

[140] H. Chouirfa, H. Bouloussa, V. Migonney, C. Falentin-Daudré, Review of titanium surface modification techniques and coatings for antibacterial applications, Acta biomaterialia 83 (2019) 37-54.

[141] I.A. Roberts, C. Wang, R. Esterlein, M. Stanford, D. Mynors, A three-dimensional finite element analysis of the temperature field during laser melting of metal powders in additive layer manufacturing, International Journal of Machine Tools and Manufacture 49(12-13) (2009) 916-923.

[142] C.-W. Chan, S. Lee, G.C. Smith, C. Donaghy, Fibre laser nitriding of titanium and its alloy in open atmosphere for orthopaedic implant applications: Investigations on surface quality, microstructure and tribological properties, Surface and Coatings Technology 309 (2017) 628-640.

[143] A.M. Kamat, S.M. Copley, J.A. Todd, A two-step laser-sustained plasma nitriding process for deep-case hardening of commercially pure titanium, Surface and Coatings Technology 313 (2017) 82-95.

[144] S. Mridha, T. Baker, Effects of nitrogen gas flow rates on the microstructure and properties of laser-nitrided IMI318 titanium alloy (Ti–4V–6Al), Journal of Materials Processing Technology 77(1-3) (1998) 115-121.

[145] R.S. Razavi, M. Salehi, M. Ramazani, H. Man, Corrosion behaviour of laser gas nitrided Ti–6Al–4V in HCl solution, Corrosion Science 51(10) (2009) 2324-2329.

[146] H. Man, M. Bai, F. Cheng, Laser diffusion nitriding of Ti–6Al–4V for improving hardness and wear resistance, Applied Surface Science 258(1) (2011) 436-441.

[147] S. Sathish, M. Geetha, N. Pandey, C. Richard, R. Asokamani, Studies on the corrosion and wear behavior of the laser nitrided biomedical titanium and its alloys, Materials Science and Engineering: C 30(3) (2010) 376-382.

[148] N. Kazantseva, P. Krakhmalev, I. Yadroitsev, A. Fefelov, A. Merkushev, M. Ilyinikh, N. Vinogradova, I. Ezhov, T. Kurennykh, Oxygen and nitrogen concentrations in the Ti-6Al-4V alloy manufactured by direct metal laser sintering (DMLS) process, Materials Letters 209 (2017) 311-314.

[149] S.N. Dahotre, H.D. Vora, R.S. Rajamure, L. Huang, R. Banerjee, W. He, N.B. Dahotre, Laser induced nitrogen enhanced titanium surfaces for improved osseo-integration, Annals of biomedical engineering 42(1) (2014) 50-61.

[150] B. Wysocki, P. Maj, A. Krawczyńska, K. Rożniatowski, J. Zdunek, K.J. Kurzydłowski, W. Święszkowski, Microstructure and mechanical properties investigation of CP titanium processed by selective laser melting (SLM), Journal of Materials Processing Technology 241 (2017) 13-23.

[151] H. Attar, K. Prashanth, A. Chaubey, M. Calin, L.C. Zhang, S. Scudino, J. Eckert, Comparison of wear properties of commercially pure titanium prepared by selective laser melting and casting processes, Materials Letters 142 (2015) 38-41.

[152] H. Attar, S. Ehtemam-Haghighi, D. Kent, I. Okulov, H. Wendrock, M. Bönisch, A. Volegov, M. Calin, J. Eckert, M. Dargusch, Nanoindentation and wear properties of Ti and Ti-

TiB composite materials produced by selective laser melting, Materials Science and Engineering: A 688 (2017) 20-26.

[153] L. Mullen, R.C. Stamp, W.K. Brooks, E. Jones, C.J. Sutcliffe, Selective Laser Melting: A regular unit cell approach for the manufacture of porous, titanium, bone in-growth constructs, suitable for orthopedic applications, Journal of Biomedical Materials Research Part B: Applied Biomaterials: An Official Journal of The Society for Biomaterials, The Japanese Society for Biomaterials, and The Australian Society for Biomaterials and the Korean Society for Biomaterials 89(2) (2009) 325-334.

[154] G. Seward, S. Celotto, D. Prior, J. Wheeler, R. Pond, In situ SEM-EBSD observations of the hcp to bcc phase transformation in commercially pure titanium, Acta Materialia 52(4) (2004) 821-832.

[155] X. Wang, S. Zhang, X. Cheng, E. Zhu, W. Hang, B. Huang, Ion kinetic energy distributions in laser-induced plasma, Spectrochimica Acta Part B: Atomic Spectroscopy 99 (2014) 101-114.

[156] V. Valvoda, J. Musil, X-ray analysis of strain in titanium nitride layers, TSF 149(1) (1987) 49-60.

[157] J.B. Fogagnolo, A.V. Rodrigues, E. Sallica-Leva, M.S. Lima, R. Caram, Surface stiffness gradient in Ti parts obtained by laser surface alloying with Cu and Nb, Surface and Coatings Technology 297 (2016) 34-42.

[158] M.C. Biesinger, L.W. Lau, A.R. Gerson, R.S.C. Smart, Resolving surface chemical states in XPS analysis of first row transition metals, oxides and hydroxides: Sc, Ti, V, Cu and Zn, Applied Surface Science 257(3) (2010) 887-898.

[159] A. Poulon-Quintin, I. Watanabe, E. Watanabe, C. Bertrand, Microstructure and mechanical properties of surface treated cast titanium with Nd: YAG laser, Dental Materials 28(9) (2012) 945-951.

[160] E. Uhlmann, R. Kersting, T.B. Klein, M.F. Cruz, A.V. Borille, Additive manufacturing of titanium alloy for aircraft components, Procedia Cirp 35 (2015) 55-60.

[161] N. Taniguchi, S. Fujibayashi, M. Takemoto, K. Sasaki, B. Otsuki, T. Nakamura, T. Matsushita, T. Kokubo, S. Matsuda, Effect of pore size on bone ingrowth into porous titanium implants fabricated by additive manufacturing: an in vivo experiment, Materials Science and Engineering: C 59 (2016) 690-701.

[162] Y.-L. Hao, S.-J. Li, R. Yang, Biomedical titanium alloys and their additive manufacturing, Rare Metals 35(9) (2016) 661-671.

[163] K. Katahira, Y. Tanida, S. Takesue, J. Komotori, Rapid surface nitriding of titanium alloy by a nanosecond fiber laser under atmospheric conditions, CIRP Annals 67(1) (2018) 563-566.

[164] N. Ohtsu, K. Kodama, K. Kitagawa, K. Wagatsuma, Comparison of surface films formed on titanium by pulsed Nd: YAG laser irradiation at different powers and wavelengths in nitrogen atmosphere, Applied Surface Science 256(14) (2010) 4522-4526.

[165] V.K. Balla, J. Soderlind, S. Bose, A. Bandyopadhyay, Microstructure, mechanical and wear properties of laser surface melted Ti6Al4V alloy, Journal of the mechanical behavior of biomedical materials 32 (2014) 335-344.

[166] J. Ciganovic, J. Stasic, B. Gakovic, M. Momcilovic, D. Milovanovic, M. Bokorov, M. Trtica, Surface modification of the titanium implant using TEA CO2 laser pulses in controllable gas atmospheres–Comparative study, Applied Surface Science 258(7) (2012) 2741-2748.

[167] A. Hindy, F. Farahmand, F. sadat Tabatabaei, In vitro biological outcome of laser application for modification or processing of titanium dental implants, Lasers in Medical Science 32(5) (2017) 1197-1206.

[168] M.D. Paz, J.I. Álava, L. Goikoetxea, S. Chiussi, I. Díaz-Güemes, J. Usón, F. Sánchez, B. León, Biological response of laser macrostructured and oxidized titanium alloy: an in vitro and in vivo study, Journal of Applied Biomaterials & Biomechanics 9(3) (2011).

[169] A.J. Antończak, Ł. Skowroński, M. Trzcinski, V.V. Kinzhybalo, Ł.K. Łazarek, K.M. Abramski, Laser-induced oxidation of titanium substrate: Analysis of the physicochemical structure of the surface and sub-surface layers, Applied Surface Science 325 (2015) 217-226.

[170] E. Akman, E. Cerkezoglu, Compositional and micro-scratch analyses of laser induced colored surface of titanium, Optics and Lasers in Engineering 84 (2016) 37-43.

[171] T. Jwad, S. Deng, H. Butt, S. Dimov, Laser induced single spot oxidation of titanium, Applied Surface Science 387 (2016) 617-624.

[172] A. Antończak, M. Trzcinski, T. Hiller, A. Bukaluk, A. Wronkowska, Optical properties of laser induced oxynitride films on titanium, Applied Surface Science 304 (2014) 107-114.

[173] F. Torrent, L. Lavisse, P. Berger, J.-M. Jouvard, H. Andrzejewski, G. Pillon, S. Bourgeois, M.M. De Lucas, Wavelength influence on nitrogen insertion into titanium by nanosecond pulsed laser irradiation in air, Applied Surface Science 278 (2013) 245-249.

[174] R. Ocaña, A. Calatayud, Laser-induced Coloring on Small Titanium Surfaces, Physics Procedia 83 (2016) 225-232.

[175] C.-C. Yang, Y.-C. Lin, C.-C. Yang, Y.-H. Lin, K.-C. Huang, K.-m. Lin, W.-T. Hsiao, Laser-induced coloring of titanium alloy using ultraviolet nanosecond pulses scanning technology, Journal of Alloys and Compounds 715 (2017) 349-361.

[176] M. Marticorena, G. Corti, D. Olmedo, M. Guglielmotti, S. Duhalde, Laser surface modification of Ti implants to improve osseointegration, Journal of Physics: Conference Series, IOP Publishing, 2007, p. 662.

[177] Á.P. Del Pino, P. Serra, J. Morenza, Laser surface processing of titanium in air: influence of scan traces overlapping, Journal of Laser Applications 15(2) (2003) 120-123.

[178] E. Ageev, Y.M. Andreeva, Y.Y. Karlagina, Y.R. Kolobov, S. Manokhin, G. Odintsova, A. Slobodov, V. Veiko, Composition analysis of oxide films formed on titanium surface under pulsed laser action by method of chemical thermodynamics, Laser Physics 27(4) (2017) 046001.

[179] L. Lavisse, M. Sahour, J. Jouvard, G. Pillon, M.M. de Lucas, S. Bourgeois, D. Grevey, Growth of titanium oxynitride layers by short pulsed Nd: YAG laser treatment of Ti plates: influence of the cumulated laser fluence, Applied Surface Science 255(10) (2009) 5515-5518.

[180] X. Zhao, S. Li, M. Zhang, Y. Liu, T.B. Sercombe, S. Wang, Y. Hao, R. Yang, L.E. Murr, Comparison of the microstructures and mechanical properties of Ti–6Al–4V fabricated by selective laser melting and electron beam melting, Materials & Design 95 (2016) 21-31.

[181] X. Li, M. Roberts, Y. Liu, C. Kang, H. Huang, T. Sercombe, Effect of substrate temperature on the interface bond between support and substrate during selective laser melting of Al–Ni–Y–Co–La metallic glass, Materials & Design (1980-2015) 65 (2015) 1-6.

[182] L. Nánai, R. Vajtai, T.F. George, Laser-induced oxidation of metals: state of the art, Thin Solid Films 298(1-2) (1997) 160-164.

[183] A. Nwobu, R. Rawlings, D. West, Nitride formation in titanium based substrates during laser surface melting in nitrogen–argon atmospheres, Acta materialia 47(2) (1999) 631-643.

[184] D. Höche, S. Müller, G. Rapin, M. Shinn, E. Remdt, M. Gubisch, P. Schaaf, Marangoni convection during free electron laser nitriding of titanium, Metallurgical and Materials Transactions B 40(4) (2009) 497-507.

[185] A.P. Del Pino, P. Serra, J. Morenza, Coloring of titanium by pulsed laser processing in air, Thin Solid Films 415(1-2) (2002) 201-205.

[186] P. Kofstad, High-temperature oxidation of titanium, Journal of the Less Common Metals 12(6) (1967) 449-464.

[187] D. David, G. Beranger, E. Garcia, A Study of the Diffusion of Oxygen in α-Titanium Oxidized in the Temperature Range 460°–700° C, Journal of The Electrochemical Society 130(6) (1983) 1423.

[188] D. David, E. Garcia, X. Lucas, G. Beranger, Etude de la diffusion de l'oxygene dans le titane α oxyde entre 700° c et 950° c, Journal of the Less Common Metals 65(1) (1979) 51-69.

[189] W.P. Roe, H.R. Palmer, W.R. Opie, Diffusion of oxygen in alpha and beta titanium, Trans. ASM 52 (1960) 191.

[190] F. Claisse, H.P. Koenig] Thermal and forced diffusion of oxygen in β-titanium, Acta Metallurgica 4(6) (1956) 650-654.

[191] O. Carlson, F. Schmidt, R. Lichtenberg, Investigation of reported anomalies in the electrotransport of interstitial solutes in titanium and iron, Metallurgical Transactions A 6(4) (1975) 725.

[192] R. Shenoy, J. Unnam, R. Clark, Oxidation and embrittlement of Ti-6Al-2Sn-4Zr-2Mo alloy, Oxidation of metals 26(1-2) (1986) 105-124.

[193] R. Cardoso, G. Arnoult, T. Belmonte, G. Henrion, S. Weber, Titanium nitriding by microwave atmospheric pressure plasma: towards single crystal synthesis, Plasma Processes and Polymers 6(S1) (2009) S302-S305.

[194] B. Yilbas, S. Shuja, M. Hashmi, A numerical solution for laser heating of titanium and nitrogen diffusion in solid, Journal of Materials Processing Technology 136(1-3) (2003) 12-23.

[195] F. Wood, O. Paasche, Dubious details of nitrogen diffusion in nitrided titanium, Thin Solid Films 40 (1977) 131-137.

[196] G. Maksimovich, V. Fedirko, I. Pogrelyuk, Nitriding of titanium alloys at the atmospheric pressure of nitrogen, Soviet materials science: a transl. of Fiziko-khimicheskaya mekhanika materialov/Academy of Sciences of the Ukrainian SSR 23(6) (1987) 566-568.

[197] H.D. Vora, R.S. Rajamure, S.N. Dahotre, Y.-H. Ho, R. Banerjee, N.B. Dahotre, Integrated experimental and theoretical approach for corrosion and wear evaluation of laser surface nitrided, Ti–6Al–4V biomaterial in physiological solution, journal of the mechanical behavior of biomedical materials 37 (2014) 153-164.

[198] A. Temmler, E. Willenborg, K. Wissenbach, Design surfaces by laser remelting, Physics Procedia 12 (2011) 419-430.

[199] K.J. Brookes, Introduction to surface engineering Peter A. Dearnley, Metal Powder Report 73(3) (2018) 126-127.

[200] T. Thorpe, A. Morrish, S. Qadri, Effect of grain size on the oxidation kinetics of sputtered titanium nitride films, Journal of Vacuum Science & Technology A: Vacuum, Surfaces, and Films 6(3) (1988) 1727-1729.

[201] A. Thomann, A. Basillais, M. Wegscheider, C. Boulmer-Leborgne, A. Pereira, P. Delaporte, M. Sentis, T. Sauvage, Chemical and structural modifications of laser treated iron surfaces: investigation of laser processing parameters, Applied Surface Science 230(1-4) (2004) 350-363.

[202] E. Carpene, P. Schaaf, M. Han, K. Lieb, M. Shinn, Reactive surface processing by irradiation with excimer laser, Nd: YAG laser, free electron laser and Ti: sapphire laser in nitrogen atmosphere, Applied Surface Science 186(1-4) (2002) 195-199.

[203] F. Esaka, K. Furuya, H. Shimada, M. Imamura, N. Matsubayashi, H. Sato, A. Nishijima, A. Kawana, H. Ichimura, T. Kikuchi, Comparison of surface oxidation of titanium nitride and chromium nitride films studied by X-ray absorption and photoelectron spectroscopy, Journal of Vacuum Science & Technology A: Vacuum, Surfaces, and Films 15(5) (1997) 2521-2528.

[204] M. Wittmer, J. Noser, H. Melchior, Oxidation kinetics of TiN thin films, Journal of Applied Physics 52(11) (1981) 6659-6664.

[205] N.C. Saha, H.G. Tompkins, Titanium nitride oxidation chemistry: An x-ray photoelectron spectroscopy study, Journal of Applied Physics 72(7) (1992) 3072-3079.

[206] H.-Y. Chen, F.-H. Lu, Oxidation behavior of titanium nitride films, Journal of Vacuum Science & Technology A: Vacuum, Surfaces, and Films 23(4) (2005) 1006-1009.

[207] H.G. Tompkins, Oxidation of titanium nitride in room air and in dry O2, Journal of Applied Physics 70(7) (1991) 3876-3880.

[208] H. Wang, R. Zhang, Z. Yuan, X. Shu, E. Liu, Z. Han, A comparative study of the corrosion performance of titanium (Ti), titanium nitride (TiN), titanium dioxide (TiO2) and nitrogen-doped titanium oxides (N–TiO2), as coatings for biomedical applications, Ceramics International 41(9) (2015) 11844-11851.

[209] F. Weng, C. Chen, H. Yu, Research status of laser cladding on titanium and its alloys: a review, Materials & Design 58 (2014) 412-425.

[210] Z. Wang, H. Hu, Y. Zheng, W. Ke, Y. Qiao, Comparison of the corrosion behavior of pure titanium and its alloys in fluoride-containing sulfuric acid, Corrosion Science 103 (2016) 50-65.

[211] L.T. Duarte, C. Bolfarini, S.R. Biaggio, R.C. Rocha-Filho, P.A. Nascente, Growth of aluminum-free porous oxide layers on titanium and its alloys Ti-6Al-4V and Ti-6Al-7Nb by micro-arc oxidation, Materials Science and Engineering: C 41 (2014) 343-348.

[212] A.H. Ettefagh, C. Zeng, S. Guo, J. Raush, Corrosion behavior of additively manufactured Ti-6Al-4V parts and the effect of post annealing, Additive Manufacturing 28 (2019) 252-258.

[213] B. Attard, A. Leyland, A. Matthews, E. Gutmanas, I. Gotman, G. Cassar, Improving the surface characteristics of Ti-6Al-4V and Timetal 834 using PIRAC nitriding treatments, Surface and Coatings Technology 339 (2018) 208-223.

[214] D. She, W. Yue, Z. Fu, C. Wang, X. Yang, J. Liu, Effects of nitriding temperature on microstructures and vacuum tribological properties of plasma-nitrided titanium, Surface and Coatings Technology 264 (2015) 32-40.

[215] Y. Bédouin, D.M. Gordin, P. Pellen-Mussi, F. Pérez, S. Tricot-Doleux, C. Vasilescu, S.I. Drob, D. Chauvel-Lebret, T. Gloriant, Enhancement of the biocompatibility by surface nitriding of a low-modulus titanium alloy for dental implant applications, Journal of Biomedical Materials Research Part B: Applied Biomaterials 107(5) (2019) 1483-1490.

[216] W.-Y. Wu, M.-Y. Chan, Y.-H. Hsu, G.-Z. Chen, S.-C. Liao, C.-H. Lee, P.-W. Lui, Bioapplication of TiN thin films deposited using high power impulse magnetron sputtering, Surface and Coatings Technology 362 (2019) 167-175.

[217] J. Sun, Q. Yao, Y. Zhang, X. Du, Y. Wu, W. Tong, Simultaneously improving surface mechanical properties and in vitro biocompatibility of pure titanium via surface mechanical attrition treatment combined with low-temperature plasma nitriding, Surface and Coatings Technology 309 (2017) 382-389.

[218] L. Duta, G.E. Stan, A.C. Popa, M.A. Husanu, S. Moga, M. Socol, I. Zgura, F. Miculescu, I. Urzica, A.C. Popescu, Thickness influence on in vitro biocompatibility of titanium nitride thin films synthesized by pulsed laser deposition, Materials 9(1) (2016) 38.

[219] S. Katayama, A. Matsunawa, A. Morimoto, S. Ishimoto, Y. Arata, Surface hardening of titanium by laser nitriding, International Congress on Applications of Lasers & Electro-Optics, Laser Institute of America, 1983, pp. 127-134.

[220] Y. Tian, C. Chen, S. Li, Q. Huo, Research progress on laser surface modification of titanium alloys, Applied Surface Science 242(1-2) (2005) 177-184.

[221] A. Thomann, E. Sicard, C. Boulmer-Leborgne, C. Vivien, J. Hermann, C. Andreazza-Vignolle, P. Andreazza, C. Meneau, Surface nitriding of titanium and aluminium by laser-induced plasma, Surface and Coatings Technology 97(1-3) (1997) 448-452.

[222] J. Abboud, Effect of processing parameters on titanium nitrided surface layers produced by laser gas nitriding, Surface and Coatings Technology 214 (2013) 19-29.

[223] A. Hamad, J. Abboud, F. Shuaeib, K. Benyounis, Surface hardening of commercially pure titanium by laser nitriding: response surface analysis, Advances in Engineering Software 41(4) (2010) 674-679.

[224] H. Xin, S. Mridha, T. Baker, The effect of laser surface nitriding with a spinning laser beam on the wear resistance of commercial purity titanium, Journal of materials science 31(1) (1996) 22-30.

[225] H. Wen, C. Zeng, A. Hemmasian Ettefagh, J. Gao, S. Guo, Laser surface treatment of Ti-10Mo alloy under Ar and N2 environment for biomedical application, Journal of Laser Applications 31(2) (2019) 022012.

[226] S. Sathish, V. Anbarasan, M. Geetha, R. Asokamani, Corrosion resistance of laser nitrided commercially pure titanium and Ti-13Nb-13Zr biomedical alloys, Transactions of the Indian Institute of Metals 61(2-3) (2008) 235-238.

[227] C.-W. Chan, L. Carson, G.C. Smith, A. Morelli, S. Lee, Enhancing the antibacterial performance of orthopaedic implant materials by fibre laser surface engineering, Applied Surface Science 404 (2017) 67-81.

[228] V.K. Balla, A. Bhat, S. Bose, A. Bandyopadhyay, Laser processed TiN reinforced Ti6Al4V composite coatings, Journal of the mechanical behavior of biomedical materials 6 (2012) 9-20.

[229] S. Zhou, Y. Zhao, X. Wang, W. Li, D. Chen, T. Sercombe, Enhanced corrosion resistance of Ti-5 wt.% TiN composite compared to commercial pure Ti produced by selective laser melting in HCl solution, Journal of Alloys and Compounds 820 (2020) 153422.

[230] C. Zeng, H. Wen, H. Bellamy, P. Sprunger, P.J. Schilling, S. Guo, Titanium and nitrogen interactions under laser additive manufacturing conditions, Surface and Coatings Technology 378 (2019) 124955.

[231] L. Wang, J. Jue, M. Xia, L. Guo, B. Yan, D. Gu, Effect of the Thermodynamic behavior of selective laser melting on the formation of in situ oxide dispersion-strengthened aluminum-based composites, Metals 6(11) (2016) 286.

[232] J. Dai, S. Hou, Laser gas nitriding of titanium and titanium alloys, Surface review and letters 16(06) (2009) 789-796.

[233] C. Zeng, H. Wen, B. Zhang, P. Sprunger, S. Guo, Diffusion of oxygen and nitrogen into titanium under laser irradiation in air, Applied Surface Science 505 (2020) 144578.

[234] H. Li, Z. Cui, Z. Li, S. Zhu, X. Yang, Surface modification by gas nitriding for improving cavitation erosion resistance of CP-Ti, Applied Surface Science 298 (2014) 164-170.

[235] A. Mukhtar, M. Fry, B. Jackson, L. Bolzoni, Effects of Gas Nitriding on Fatigue and Crack Initiation of Ti6Al4V produced by Selective Laser Melting, Materials Research 22 (2019).

[236] Z. Chen, G. Zhou, Z. Chen, Microstructure and hardness investigation of 17-4PH stainless steel by laser quenching, Materials Science and Engineering: A 534 (2012) 536-541.

[237] W. Lengauer, Properties of bulk δ-TiN1-x prepared by nitrogen diffusion into titanium metal, Journal of alloys and compounds 186(2) (1992) 293-307.

[238] L. Fleischmann, A. Crismani, F. Falkensammer, H.-P. Bantleon, X. Rausch-Fan, O. Andrukhov, Behavior of osteoblasts on TI surface with two different coating designed for orthodontic devices, Journal of Materials Science: Materials in Medicine 26(1) (2015) 10.

[239] M. Annunziata, L. Guida, L. Perillo, R. Aversa, I. Passaro, A. Oliva, Biological response of human bone marrow stromal cells to sandblasted titanium nitride-coated implant surfaces, Journal of Materials Science: Materials in Medicine 19(12) (2008) 3585-3591.

[240] L. Le Guéhennec, A. Soueidan, P. Layrolle, Y. Amouriq, Surface treatments of titanium dental implants for rapid osseointegration, Dental Materials 23(7) (2007) 844-854.

[241] R. Asri, W. Harun, M. Samykano, N. Lah, S. Ghani, F. Tarlochan, M. Raza, Corrosion and surface modification on biocompatible metals: A review, Materials Science and Engineering: C 77 (2017) 1261-1274.

[242] M.A. Hussein, B. Yilbas, A.M. Kumar, R. Drew, N. Al-Aqeeli, Influence of laser nitriding on the surface and corrosion properties of Ti-20Nb-13Zr alloy in artificial saliva for dental applications, Journal of Materials Engineering and Performance 27(9) (2018) 4655-4664.

[243] C. Alves Jr, C.G. Neto, G. Morais, C. Da Silva, V. Hajek, Nitriding of titanium disks and industrial dental implants using hollow cathode discharge, Surface and Coatings Technology 200(11) (2006) 3657-3663.

[244] S. Bodhak, S. Bose, A. Bandyopadhyay, Role of surface charge and wettability on early stage mineralization and bone cell–materials interactions of polarized hydroxyapatite, Acta Biomaterialia 5(6) (2009) 2178-2188.

[245] N.J. Hallab, K.J. Bundy, K. O'Connor, R.L. Moses, J.J. Jacobs, Evaluation of metallic and polymeric biomaterial surface energy and surface roughness characteristics for directed cell adhesion, Tissue Engineering 7(1) (2001) 55-71.

[246] H.R.A. Bidhendi, M. Pouranvari, Corrosion study of metallic biomaterials in simulated body fluid, Metallurgical and Materials Engineering (2012).

[247] T. Yetim, Corrosion Behavior of Ag-doped TiO 2 Coatings on Commercially Pure Titanium in Simulated Body Fluid Solution, Journal of Bionic Engineering 13(3) (2016) 397-405.

[248] X. Yan, D. Yang, X. Liu, Corrosion behavior of a laser-welded NiTi shape memory alloy, Materials Characterization 58(7) (2007) 623-628.

[249] S. Gollapudi, Grain size distribution effects on the corrosion behaviour of materials, Corrosion Science 62 (2012) 90-94.

[250] I. Pohrelyuk, V. Fedirko, O. Tkachuk, R. Proskurnyak, Corrosion resistance of Ti–6Al–4V alloy with nitride coatings in Ringer's solution, Corrosion Science 66 (2013) 392-398.

[251] K. Lee, C. Hu, K.-N. Tu, In situ scanning electron microscope comparison studies on electromigration of Cu and Cu (Sn) alloys for advanced chip interconnects, Journal of applied physics 78(7) (1995) 4428-4437.

[252] B.S. Ünlü, E. Atik, Evaluation of effect of alloy elements in copper based CuSn10 and CuZn30 bearings on tribological and mechanical properties, Journal of Alloys and Compounds 489(1) (2010) 262-268.

[253] A. Canakci, T. Varol, H. Cuvalci, F. Erdemir, S. Ozkaya, E. Yalcın, Synthesis of novel CuSn10-graphite nanocomposite powders by mechanical alloying, Micro & Nano Letters 9(2) (2014) 109-112.

[254] X. Chen, Z. Wang, D. Ding, H. Tang, L. Qiu, X. Luo, G. Shi, Strengthening and toughening strategies for tin bronze alloy through fabricating in-situ nanostructured grains, Materials & Design (1980-2015) 66 (2015) 60-66.

[255] D.D. Gu, W. Meiners, K. Wissenbach, R. Poprawe, Laser additive manufacturing of metallic components: materials, processes and mechanisms, International Materials Reviews 57(3) (2012) 133-164.

[256] C.Y. Yap, C.K. Chua, Z.L. Dong, Z.H. Liu, D.Q. Zhang, L.E. Loh, S.L. Sing, Review of selective laser melting: Materials and applications, Applied physics reviews 2(4) (2015) 041101.

[257] Y.S. Touloukian, R. Powell, C. Ho, P. Klemens, Thermophysical properties of matter-the tprc data series. volume 1. thermal conductivity-metallic elements and alloys, THERMOPHYSICAL AND ELECTRONIC PROPERTIES INFORMATION ANALYSIS CENTER …, 1970.

[258] E. Sidot, N. Souissi, L. Bousselmi, E. Triki, L. Robbiola, Study of the corrosion behaviour of Cu–10Sn bronze in aerated Na2SO4 aqueous solution, Corrosion Science 48(8) (2006) 2241-2257.

[259] G. Ingo, T. De Caro, C. Riccucci, E. Angelini, S. Grassini, S. Balbi, P. Bernardini, D. Salvi, L. Bousselmi, M. Gener, Large scale investigation of chemical composition, structure and corrosion mechanism of bronze archeological artefacts from Mediterranean basin, Applied Physics A 83(4) (2006) 513-520.

[260] C. Chiavari, A. Colledan, A. Frignani, G. Brunoro, Corrosion evaluation of traditional and new bronzes for artistic castings, Materials Chemistry and Physics 95(2-3) (2006) 252-259.

[261] N. Souissi, E. Sidot, L. Bousselmi, E. Triki, L. Robbiola, Corrosion behaviour of Cu–10Sn bronze in aerated NaCl aqueous media–electrochemical investigation, Corrosion Science 49(8) (2007) 3333-3347.

[262] L. Robbiola, T. Tran, P. Dubot, O. Majerus, K. Rahmouni, Characterisation of anodic layers on Cu–10Sn bronze (RDE) in aerated NaCl solution, Corrosion Science 50(8) (2008) 2205-2215.

[263] K. Zohdy, M. Sadawy, M. Ghanem, Corrosion behavior of leaded-bronze alloys in sea water, Materials Chemistry and Physics 147(3) (2014) 878-883.

[264] A. Drach, I. Tsukrov, J. DeCew, J. Aufrecht, A. Grohbauer, U. Hofmann, Field studies of corrosion behaviour of copper alloys in natural seawater, Corrosion Science 76 (2013) 453-464.

[265] B. Zhang, Y. Song, G.Z. Voyiadjis, W.J. Meng, Assessing texture development and mechanical response in microscale reverse extrusion of copper, Journal of Materials Research 33(8) (2018) 978-988.

[266] J.R. Croteau, S. Griffiths, M.D. Rossell, C. Leinenbach, C. Kenel, V. Jansen, D.N. Seidman, D.C. Dunand, N.Q. Vo, Microstructure and mechanical properties of Al-Mg-Zr alloys processed by selective laser melting, Acta Materialia 153 (2018) 35-44.

[267] D. Wang, C. Song, Y. Yang, Y. Bai, Investigation of crystal growth mechanism during selective laser melting and mechanical property characterization of 316L stainless steel parts, Materials & Design 100 (2016) 291-299.

[268] M.M. Kirka, Y. Lee, D.A. Greeley, A. Okello, M.J. Goin, M.T. Pearce, R.R. Dehoff, Strategy for texture management in metals additive manufacturing, JOM 69(3) (2017) 523-531.

[269] Y. Lu, S. Wu, Y. Gan, T. Huang, C. Yang, L. Junjie, J. Lin, Study on the microstructure, mechanical property and residual stress of SLM Inconel-718 alloy manufactured by differing island scanning strategy, Optics & Laser Technology 75 (2015) 197-206.

[270] L. Thijs, K. Kempen, J.-P. Kruth, J. Van Humbeeck, Fine-structured aluminium products with controllable texture by selective laser melting of pre-alloyed AlSi10Mg powder, Acta Materialia 61(5) (2013) 1809-1819.

[271] E. Hall, The deformation and ageing of mild steel: III discussion of results, Proceedings of the Physical Society. Section B 64(9) (1951) 747.

[272] Z. He, C. Jian, J.-C. Feng, Microstructure and mechanical properties of Ti6Al4V/Cu-10Sn bronze diffusion-bonded joint, Transactions of Nonferrous Metals Society of China 19 (2009) s414-s417.

[273] E.A. Gadallah, M.A. Ghanem, M. Abd El-Hamid, A.E. El-Nikhaily, Effect of tin content and ECAP passes on the mechanical properties of Cu/Sn alloys, American Journal of Science and Technology 2(1) (2014) 60.

[274] A.E. Nassef, A. Alateyah, M.A. El-Hadek, W. El-Garaihy, Mechanical behavior and fracture surface characterization of liquid-phase sintered Cu-Sn powder alloys, Advanced Materials Letters 8 (2017) 717-722.

[275] A. Nassef, M. El-Hadek, Microstructure and mechanical behavior of hot pressed Cu-Sn powder alloys, Advances in Materials Science and Engineering 2016 (2016).

[276] R. Abedinzadeh, S.M. Safavi, F. Karimzadeh, A study of pressureless microwave sintering, microwave-assisted hot press sintering and conventional hot pressing on properties of aluminium/alumina nanocomposite, Journal of mechanical science and technology 30(5) (2016) 1967-1972.

[277] S. Pauly, P. Wang, U. Kühn, K. Kosiba, Experimental determination of cooling rates in selectively laser-melted eutectic Al-33Cu, Additive Manufacturing 22 (2018) 753-757.

[278] X. Wang, L.N. Carter, B. Pang, M.M. Attallah, M.H. Loretto, Microstructure and yield strength of SLM-fabricated CM247LC Ni-Superalloy, Acta Materialia 128 (2017) 87-95.

[279] Y.S. Touloukian, Thermophysical Properties of Matter: Metallic Elements and Alloys. Thermal Conductivity, IFI/Plenum1970.

[280] C. Smith, THERMAL CONDUCTIVITY OF COPPER ALLOYS II.-COPPER-TIN ALLOYS III.-COPPER-PHOSPHORUS ALLOYS, AIME TECH PUBL 1930 (1930) 11.

[281] M. Cook, W. Tallis, The Physical Properties and Annealing Characteristics of Standard Phosphor-Bronze Alloys, J INST MET 67 (1941) 49-65.

[282] C.-L. Huang, Z.-Z. Lin, Y.-H. Feng, X.-X. Zhang, G. Wang, Thermal conductivity prediction of 2-dimensional square-pore metallic nanoporous materials with kinetic method approach, International Journal of Thermal Sciences 112 (2017) 263-269.

[283] A. Mallikarjunan, S. Sharma, S. Murarka, Resistivity of copper films at thicknesses near the mean free path of electrons in copper minimization of the diffuse scattering in copper, Electrochemical and Solid State Letters 3(9) (2000) 437.

[284] J. Plombon, E. Andideh, V.M. Dubin, J. Maiz, Influence of phonon, geometry, impurity, and grain size on copper line resistivity, Applied physics letters 89(11) (2006) 113124.

[285] I. Sumirat, Y. Ando, S. Shimamura, Theoretical consideration of the effect of porosity on thermal conductivity of porous materials, Journal of Porous Materials 13(3-4) (2006) 439-443.

[286] K. Pietrak, T.S. Wiśniewski, A review of models for effective thermal conductivity of composite materials, Journal of Power Technologies 95(1) (2014) 14-24.

[287] M. Booth, J. Brandon, R. Brizard, C.t. Chieh, W. Pearson, γ-Brasses with F cells, Acta Crystallographica Section B: Structural Crystallography and Crystal Chemistry 33(1) (1977) 30-36.

[288] S.I. Kim, K.H. Lee, H.A. Mun, H.S. Kim, S.W. Hwang, J.W. Roh, D.J. Yang, W.H. Shin, X.S. Li, Y.H. Lee, Dense dislocation arrays embedded in grain boundaries for high-performance bulk thermoelectrics, Science 348(6230) (2015) 109-114.

[289] K. Ralston, N. Birbilis, C. Davies, Revealing the relationship between grain size and corrosion rate of metals, Scripta Materialia 63(12) (2010) 1201-1204.

[290] W. Luo, C. Qian, X. Wu, M. Yan, Electrochemical corrosion behavior of nanocrystalline copper bulk, Materials Science and Engineering: A 452 (2007) 524-528.

[291] A. Barbucci, G. Farne, P. Matteazzi, R. Riccieri, G. Cerisola, Corrosion behaviour of nanocrystalline Cu90Ni10 alloy in neutral solution containing chlorides, Corrosion Science 41(3) (1998) 463-475.

[292] N. Fu, X. Tang, D. Li, L. Parent, H. Tian, In situ investigation of local corrosion at interphase boundary under an electrochemical-atomic force microscope, Journal of Solid State Electrochemistry 19(2) (2015) 337-344.

[293] I.J.C. Team, The impact of materials selection on the design of the International Thermonuclear Experimental Reactor (ITER), Journal of Nuclear Materials 212 (1994) 3-10.

[294] U. Holzwarth, H. Stamm, M. Pisoni, A. Volcan, R. Scholz, The recovery of tensile properties of CuCrZr alloy after hot isostatic pressing, Fusion Engineering and Design 51 (2000) 111-116.

[295] V. Barabash, G. Kalinin, S.A. Fabritsiev, S.J. Zinkle, Specification of CuCrZr alloy properties after various thermo-mechanical treatments and design allowables including neutron irradiation effects, Journal of Nuclear Materials 417(1-3) (2011) 904-907.

[296] J.-Y. Park, Y.-I. Jung, B.-K. Choi, J.-S. Lee, Y.H. Jeong, B.G. Hong, Investigation on the microstructure and mechanical properties of CuCrZr after manufacturing thermal cycle for plasma facing component, Journal of Nuclear Materials 417(1-3) (2011) 916-919.

[297] M. Merola, A. Orsini, E. Visca, S. Libera, L. Moreschi, S. Storai, B. Panella, E. Campagnoli, G. Ruscica, C. Bosco, Influence of the manufacturing heat cycles on the CuCrZr properties, Journal of Nuclear Materials 307 (2002) 677-680.

[298] A. Ivanov, A. Nikolaev, G. Kalinin, M. Rodin, Effect of heat treatments on the properties of CuCrZr alloys, Journal of Nuclear Materials 307 (2002) 673-676.

[299] D. Edwards, B.N. Singh, S. Tähtinen, Effect of heat treatments on precipitate microstructure and mechanical properties of a CuCrZr alloy, Journal of Nuclear Materials 367 (2007) 904-909.

[300] J.-Y. Park, J.-S. Lee, B.-K. Choi, B.G. Hong, Y.H. Jeong, Effect of cooling rate on mechanical properties of aged ITER-grade CuCrZr, Fusion Engineering and Design 83(10-12) (2008) 1503-1507.

[301] O. Gillia, L. Briottet, I. Chu, P. Lemoine, E. Rigal, A. Peacock, Characterization of CuCrZr and CuCrZr/SS joint strength for different blanket components manufacturing conditions, Journal of Nuclear Materials 386 (2009) 830-833.

[302] G. Kalinin, A. Ivanov, A. Obushev, B. Rodchenkov, M. Rodin, Y. Strebkov, Ageing effect on the properties of CuCrZr alloy used for the ITER HHF components, Journal of Nuclear Materials 367 (2007) 920-924.

[303] N. Sitnikov, A. Shelyakov, R. Rizakhanov, N. Mitina, I. Khabibullina, The effect of copper on structure of TiNiCu melt-spun ribbons, Materials Today: Proceedings 4(3) (2017) 4680-4684.

[304] J.-O. Andersson, T. Helander, L. Höglund, P. Shi, B. Sundman, Thermo-Calc & DICTRA, computational tools for materials science, Calphad 26(2) (2002) 273-312.

[305] M.S.I.T.M.i.m.c.h.w.m. com, Cr-Cu-Zr (Chromium-Copper-Zirconium) Non-Ferrous Metal Ternary Systems. Selected Copper Systems: Phase Diagrams, Crystallographic and Thermodynamic Data, Non-Ferrous Metal Systems. Part 2: Selected Copper Systems (2007) 228-242.

[306] P. Guan, X. Chen, P. Liu, F. Sun, C. Zhu, H. Zhou, S. Fu, Z. Wu, Y. Zhu, Effect of selective laser melting process parameters and aging heat treatment on properties of CuCrZr alloy, Materials Research Express 6(11) (2019) 1165c1.

[307] S. Preston, I. Bretherton, C. Forty, The thermophysical and mechanical properties of the copper heat sink material intended for use in ITER, Fusion Engineering and Design 66 (2003) 441-446.

[308] S. Choi, H. Cho, S. Kumai, Effect of the precipitation of secondary phases on the thermal diffusivity and thermal conductivity of Al-4.5 Cu alloy, Journal of Alloys and Compounds 688 (2016) 897-902.

[309] P. Olaffsson, R. Sandstrom, A. Karlsson, Comparison of experimental, calculated and observed values for electrical and thermal conductivity of aluminium alloys, (2013).

[310] R. Endo, M. Shima, M. Susa, Thermal-conductivity measurements and predictions for Ni–Cr solid solution alloys, International Journal of Thermophysics 31(10) (2010) 1991-2003.

[311] Y. Zhang, G.M. Stocks, K. Jin, C. Lu, H. Bei, B.C. Sales, L. Wang, L.K. Béland, R.E. Stoller, G.D. Samolyuk, Influence of chemical disorder on energy dissipation and defect evolution in concentrated solid solution alloys, Nature communications 6(1) (2015) 1-9.

[312] Z. Shijie, Z. Bingjun, Z. Zhen, J. Xin, Application of lanthanum in high strength and high conductivity copper alloys, Journal of Rare Earths 24(1) (2006) 385-388.

[313] S. Han, J. Gu, J. Lee, Z. Que, J. Shin, S. Lim, S. Kim, Effect of V addition on hardness and electrical conductivity in Cu-Ni-Si alloys, Metals and Materials International 19(4) (2013) 637-641.

[314] V. Gray, D. Galvin, L. Sun, E. Gilbert, T. Martin, P. Hill, M. Rawson, K. Perkins, Precipitation in a novel maraging steel F1E: A study of austenitization and aging using small angle neutron scattering, Materials Characterization 129 (2017) 270-281.

[315] Z. Ding, S. Jia, P. Zhao, M. Deng, K. Song, Hot deformation behavior of Cu–0.6 Cr–0.03 Zr alloy during compression at elevated temperatures, Materials Science and Engineering: A 570 (2013) 87-91.

[316] J.-h. Su, Q.-m. Dong, P. Liu, H.-j. Li, B.-x. Kang, Research on aging precipitation in a Cu–Cr–Zr–Mg alloy, Materials Science and Engineering: A 392(1-2) (2005) 422-426.

[317] T. Hamaoka, M. Takeguchi, Displacement fields around Guinier–Preston 1 zones in Al–Cu alloys: investigations using MD and ADF-STEM image simulations, Philosophical Magazine 98(31) (2018) 2845-2860.

[318] Y. Pang, C. Xia, M. Wang, Z. Li, Z. Xiao, H. Wei, X. Sheng, Y. Jia, C. Chen, Effects of Zr and (Ni, Si) additions on properties and microstructure of Cu–Cr alloy, Journal of alloys and compounds 582 (2014) 786-792.

[319] M. Hatakeyama, T. Toyama, J. Yang, Y. Nagai, M. Hasegawa, T. Ohkubo, M. Eldrup, B.N. Singh, 3D-AP and positron annihilation study of precipitation behavior in Cu–Cr–Zr alloy, Journal of Nuclear Materials 386 (2009) 852-855.

[320] M. Hatakeyama, T. Toyama, Y. Nagai, M. Hasegawa, M. Eldrup, B.N. Singh, Nanostructural evolution of Cr-rich precipitates in a Cu-Cr-Zr alloy during heat treatment studied by 3 dimensional atom probe, Materials transactions (2008) 0802180333-0802180333.

Vita

Congyuan Zeng was born in Jiangsu, China, in 1990. He graduated from Southeast Univeristy, Nanjing, China, and received his Bachelor Degree in Materials Science and Engineering in June 2013. In June 2016, he grauated from Southeast University and received his Master's Degree also in Materials Science and Enginnering. In Augest 2016, he enrolled in the Department of Mechanical Enginnering, Louisiana State University, as a Ph.D student under the supervision of Dr. Shengmin Guo.